NOVEL REGIMES OF QUANTUM OPTOMECHANICS

LUKAS NEUMEIER

PhD Thesis

Thesis supervisor: Prof. Darrick E. Chang

ICFO-The Institute of Photonic Sciences
Universtitat Politècnica de Catalunya

April 2018 – Barcelona

Für Valentin

ABSTRACT

In everyday life the impact of light on the motion of mechanical objects is negligible. However, modern experiments making use of high quality optical resonators are able to observe significant effects originating from the forces associated with photons on small mechanical systems. The common feature of these systems is the dependence of the optical resonance frequency on the position of the mechanical object, laying the framework of optomechanics. Many interesting regimes have been explored which allow for photon-light entanglement, laser cooling of motion, generation of squeezed states of light, and even the detection of gravitational waves. Interestingly, the optomechanical interaction is so generic that its underlying concepts and derived insights can be generally applied to a large variety of systems, as we will see in this thesis.

In Chapter 1, we provide a brief overview of key concepts and results from the field of optomechanics, before going on to discuss the novel regimes and applications that we have identified and proposed.

In Chapter 2, we theoretically investigate results from a couple of experiments, that were previously not well-understood. These experiments trap dielectric nano-particles through an optical resonator mode and observe that the intensities experienced by the particles are strongly reduced compared to a conventional optical tweezer trap. We find that these systems can be fully described by a simple optomechanical toy model and derive that the optical potential inside resonators can approach a nearly perfect square well. This potential can be dynamically reshaped by changing the driving laser frequency and we find a dramatic reduction of intensities seen by the trapped particle, which could significantly increase the range of systems to which optical trapping can be applied. These results are quite remarkable and should have important implications for future trapping technologies.

In Chapter 3, we recognize that a major trend within the field of cavity QED is to attain the strong coupling regime. Additional rich dynamics can occur by considering the atomic motional degree of freedom. In particular, we show that such a system is a natural candidate to explore the single-photon optomechanical strong coupling regime of quantum optomechanics, but where the motional frequency cannot be resolved by the cavity. We show that this regime can result in a number of remarkable phenomena, such as strong entanglement between the atomic wave-function and the scattering properties of single incident photons, or an anomalous heating mechanism of atomic motion.

In Chapter 4 we show that an atom trapped in and coupled to a cavity constitutes an attractive platform for realizing the optomechanical single-photon strong coupling regime with resolved mechanical sidebands. Realizing this regime is a major goal within the field of optomechanics, as it would enable the deterministic generation of non-classical states of light. However, this regime is difficult to achieve with conventional mechanical systems due to their small zero-point motions. As an example, we show that optomechanically-induced photon blockade can be realized in realistic setups, wherein non-classical light is generated due to the interaction of photons with the atomic motion alone.

RESUMEN

En la vida cotidiana, el impacto de la luz sobre el movimiento de los objetos mecánicos es insignificante. Sin embargo, los experimentos modernos que usan resonadores ópticos de alta calidad son capaces de observar efectos significativos que se originan de las fuerzas asociadas con los fotones en pequeños sistemas mecánicos. La característica común de estos sistemas es la dependencia de la frecuencia de resonancia óptica en la posición del objeto mecánico, que establece el campo de la optomecánica. Se han explorado muchos regímenes interesantes que permiten el entrelazamiento de fotones, el enfriamiento del movimiento por láser, la generación de estados de luz comprimidos e incluso la detección de ondas gravitacionales. Curiosamente, la interacción optomecánica es tan genérica que sus conceptos subyacentes y sus profundas consecuencias pueden aplicarse generalmente a una gran variedad de sistemas, como veremos en esta tesis.

En el Capítulo 1, proporcionamos una breve descripción de los principales conceptos y resultados del campo de la optomecánica, antes de pasar a analizar los nuevos regímenes y aplicaciones que hemos identificado y propuesto.

En el Capítulo 2, investigamos teóricamente los resultados de un par de experimentos que antes no se entendían bien. Estos experimentos atrapan nanopartículas dieléctricas a través de un modo de un resonador óptico y observan que las intensidades

experimentadas por las partículas se reducen considerablemente en comparación con una trampa de pinzas ópticas convencional. Encontramos que estos sistemas se pueden describir completamente mediante un modelo optomecánico de juguete simple y demostramos que el potencial óptico dentro de los resonadores puede aproximarse a un pozo cuadrado casi perfecto. Este potencial se puede modificar dinámicamente cambiando la frecuencia de entrada del láser y encontramos una reducción drástica de las intensidades vistas por la partícula atrapada, lo que podría aumentar significativamente el rango de sistemas a los que se puede aplicar el atrapamiento óptico. Estos resultados son bastante notables y deberían tener implicaciones importantes para las futuras tecnologías de atrapamiento.

En el Capítulo 3, reconocemos que una tendencia importante en el campo de la electrodinámica cuántica de cavidades (del inglés, çavity QED") es lograr un régimen de acoplamiento fuerte. Se pueden producir dinámicas adicionales al considerar el grado de libertad de movimiento atómico. En particular, mostramos que dicho sistema es un candidato natural para explorar el régimen de acoplamiento fuerte optomecánico de un único fotón en optomecánica cuántica, pero donde la frecuencia de movimiento no puede ser resuelta por la cavidad. Mostramos que este régimen puede dar lugar a una serie de fenómenos notables, como un fuerte entrelazamiento entre la función de onda atómica y las propiedades de dispersión de los fotones incidentes individuales, o un mecanismo de calentamiento anómalo del movimiento atómico.

En el Capítulo 4 mostramos que un átomo atrapado y acoplado a una cavidad constituye una plataforma atractiva para obtener el régimen de acoplamiento fuerte optomecánico con un único fotón y con bandas laterales mecánicas resueltas. La obtención de este régimen es un objetivo principal en el campo de la optomecánica, ya que permitiría la generación determinista de estados de luz no clásicos. Sin embargo, este régimen es difícil de lograr con los sistemas mecánicos convencionales debido a sus pequeños movimientos de punto cero. Como ejemplo, mostramos que el bloqueo de fotones inducido de forma mecánica puede realizarse en configuraciones realistas, donde la luz no clásica se genera solamente debido a la interacción de fotones con el movimiento atómico.

PUBLICATIONS

1. Neumeier, L. Quidant, R & Chang, D. E. Self-induced back-action optical trapping in nanophotonic systems, *New J. Phys.* **17**, 123008 (2015).
2. Neumeier & Chang, D. E. Exploring unresolved sideband, optomechanical strong coupling using a single atom coupled to a cavity: soon
3. Neumeier, L, Northup T. E & Chang, D. E. Reaching the optomechanical strong coupling regime with a single atom in a cavity, arXiv:1711.09619 (2017)

The results of the first publication are included in Chapter 2 and those of the second and third publication are included in Chapter 3 and 4, respectively.

ACKNOWLEDGMENTS

Firstly I would like to express my sincere gratitude to my thesis advisor and mentor Prof. Darrick Chang. Thank you for letting me experience your level of rational thinking, your way of communicating scientific ideas and your merciless realism. I profited a lot from your perspective. Also thank you for your empathy and understanding during a pretty tough time. I see you not only as an outstanding scientist but also as a wonderful human being.

I had the pleasure of collaborating with Prof. Romain Quidant doing amazing research at ICFO and with Prof. Tracy Northup doing ambitious experiments in her lab in Innsbruck. Thank you for sharing your experimental perspective with me and your great talk at the mechanical systems in the quantum regime conference. I would also like to thank Prof. Jeff Kimble for stimulating discussions and for inviting our group to Caltech.

Thanks to my former group colleagues who share with me their interest in physics and who were fun to have around at conferences, lunches and group meetings. Thanks James, Tommaso, Ana, Marco, Marinko, Christine, Hessam, Marcos, David, Loïc and Stefano.

I would like to thank the "Severo Ochoa" program for funding my PhD.

Thank you for being awesome friends in Barcelona and for sharing wonderful times or even a flat: Raquel, Joao, Rainer, Nina, Sam, Brittany, Nello, Angelo, Susan, Sabine, Ksenjia, Thomas, Thomas, Amalia, Martin, Diego. My life here would have been very different without you.

Thank you for being my closest friends from all around the world and for sharing wonderful moments: Sebastian, Franky, Sonia, Anton, Mark, Baumi, Henrii, Harry, Heino, Kathi, Engo, Andrea, Michaela, Phillip, Ferhan, Lea, Mark, Alex, Jo, Casey, Kathi, Stefan, Annika, Jessica, Bene, Flo, Julian, Lisa, Dominik, Nici, Thomas, Martin, Mona, Peter....

Danke fuer die Unterstützung meine Familie, Mama, Papa, Jonas, Lena, Harry, meine Großeltern, Tanten und Onkels, Cousins, Anton und Evi und für die Existenz meines Sohnes Valentin und danke an seine Mutter Martina, die sich gut um ihn kümmert wärend ich diese Arbeit hier schreibe.

CONTENTS

Part I

INTRODUCTION

1

INTRODUCTION

1.1 FORCES OF LIGHT

A photon walks into a hotel and the receptionist asks "Hi! Can we help you with your luggage?" And the photon responds: "No thanks, I am traveling light!"

So what can we learn from this joke? Particles of light are called photons, which we can count. Other than being countable they also change the velocity of things they hit. The force arising from continuous hitting is known as the radiation pressure force [1]. Due to the large mass of macroscopic mechanical objects, the effect of this force applied by single photons is incredibly weak. As an example, when a single photon reflects off a smartphone at rest, the velocity of that smartphone after the interaction is about one atom-size per age of the universe. However, if we reflect a photon on a single atom at rest, the atom has a velocity of roughly one smartphone length per second, which is a decent effect at the single photon level and something to keep in mind. Optical forces have many applications ranging from physics to life sciences. For example they are exploited for solar sails [2], for cooling atoms [3] and for optical tweezers that can trap and move small particles around [4].

The effects of optical forces are most easily seen with large laser intensities, due to the small effect that a single photon typically has. One way to increase the effect of optical forces, without increasing the incident intensity, is to utilize an optical resonator (cavity). An example of an optical cavity with length L is shown in Figure 1.1a). We assume that the cavity is driven by a coherent laser drive with frequency ω_L and number flux E_0^2 through the left mirror. The cavity supports optical modes with frequencies $\omega_c = 2\pi c/\lambda$ with possible wavevelength obeying $m \cdot \lambda/2 = L$, m being any positive integer number. For most setups it is sufficient to only consider a single optical mode, that for which the frequency ω_c is closest to the laser frequency. Here, for simplicity we assume equal mirrors with a decay rate of $\kappa/2$ each, and ignore intrinsic losses. Resonant photons ($\omega_L = \omega_c$) bounce back and forth between the mirrors many times before they decay with rate κ. Thus, the number of resonant photons inside the cavity is proportional to $n_c \propto E_0^2/\kappa$, as shown in Fig. 1.1b), where we plot the number of intra-cavity photons n_c as a function of laser frequency. It becomes obvious

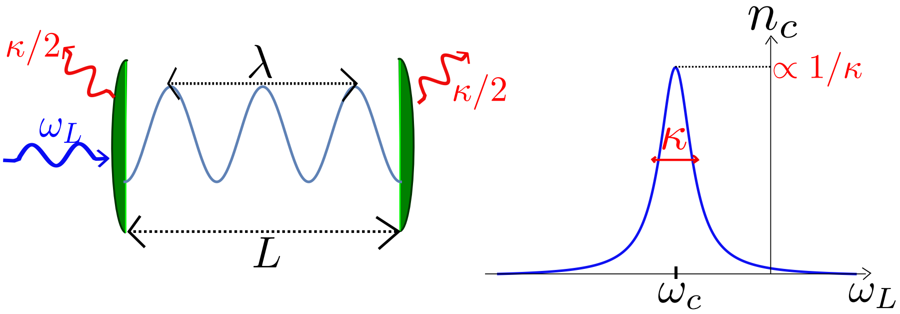

Figure 1.1: **a) Illustration of an optical cavity** with length L creating a standing wave optical mode with wavelength λ corresponding to a resonance frequency $\omega_c = 2\pi c/\lambda$. The cavity consists of two equal mirrors each having a decay rate of $\kappa/2$ and is coherently driven with a laser of frequency ω_L through the left mirror.
b) The number of photons n_c inside the cavity (qualitatively) as a function of laser frequency ω_L forms a Lorentzian centered around the cavity frequency ($\omega_L = \omega_c$) with width κ and a maximum value of $n_c \propto 1/\kappa$.

that good mirrors (small κ) can lead to a huge build up of light intensity inside the cavity. This allows enhanced optical forces $F_{opt} \propto n_c$ on objects trapped inside the cavity (and on the cavity mirrors themselves).

The idea of using cavities to enhance optical forces (or many other effects involving light) is quite old. However, in the past ten years, the field of "optomechanics" has seen explosive growth. At a broad level, this field aims to observe and exploit interesting dynamical effects that can occur, when optical cavity forces and the motion they induce modify the properties of the cavity itself. A simple model where such effects can be understood is illustrated in Fig. 1.2a), where now one of the cavity mirrors is mounted on a spring and allowed to move.

For an empty cavity, the mirror has an equilibrium position x_0 and the cavity a length L determining its resonance frequency $\omega_c(x_0)$. In Fig. 1.2b) we turn on an external laser drive populating the cavity with photons. For large n_c, the balance of optical forces and the restoring force of the spring results in a new equilibrium position $\bar{x}_0$, which increases the length of the cavity and results in a lower resonance frequency $\omega_c(\bar{x}_0)$. This enables an interesting dynamic: The resonance frequency of the cavity depends on the position of the mirror, the position of the mirror depends on the number of photons inside the cavity and the number of photons depends again on the resonance frequency of the cavity. The dynamics arising from this interplay can give rise to remarkable effects. Perhaps most notably, it enables an incoming laser to extract energy from a motional degree of freedom, thereby reducing its effective temperature [5, 6].

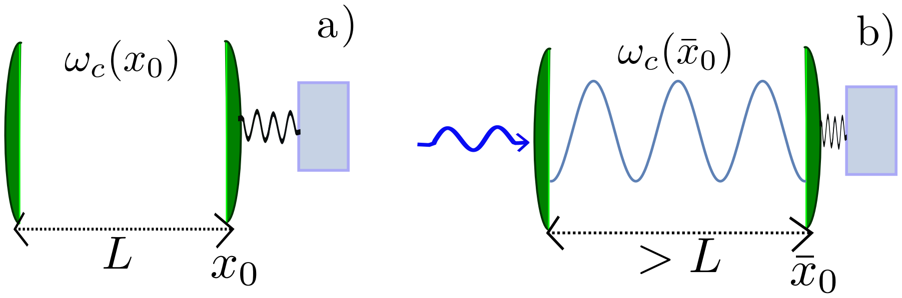

Figure 1.2: **Illustration of the standard optomechanical setup.**
a) An empty cavity with length L, where the right mirror is attached to a spring representing a vibrational mode. The cavity frequency $\omega_c(x_0)$ depends on its equilibrium position x_0.
b) A coherently driven cavity. The radiation pressure force on the mirrors is proportional to the number of photons n_c inside the cavity. Thus, many photons inside the cavity push the right mirror to a new equilibrium position $\bar{x}_0$, which increases the cavity length $> L$ and as a consequence reduces its resonance frequency to $\omega_c(\bar{x}_0)$.

It turns out that a simple and "standard" physical model underlying the system illustrated in Fig. 1.2 can equally apply to a broad class of systems that contain coupled optical and mechanical resonances. This provides a large number of ways in which optomechanical effects can be observed and exploited (see Sec. 1.2). At the same time, in all systems explored thus far, a single photon still has a very weak optomechanical effect, which necessitates that a large number of photons are sent in. Within this context, the broad questions this thesis aims to answer can be summarized in two bullet points:

- Can one, inspired by the concepts of optomechanics, find new applications or identify new phenomena in systems, which go beyond the "standard" optomechanical model?
- Can we find new systems, where the interaction between individual photons and motion becomes very strong, creating a new playground to explore optomechanical phenomena in the quantum regime?

Before we answer these questions in Chapters 2-4, we will provide a basic introduction into the theory of cavity optomechanics.

1.2 STANDARD REGIMES OF OPTOMECHANICS

Here, we will introduce the standard regimes of optomechanics, which have been both theoretically analyzed and experimentally observed. As hinted by Fig. 1.2, a minimal model of optomechanical interactions involves a single optical and mechanical degree of freedom, and where the optical resonance depends on the position of the mechanical system. A corresponding Hamiltonian thus reads [7]:

$$H_{om} = \omega_m b^\dagger b + \omega_c(x) a^\dagger a. \tag{1.1}$$

We use a and b as the annihilation operators for photons and phonons in the optical and mechanical modes, respectively, and ω_m is the frequency of the mechanical mode. For simplicity we neglect mechanical damping. $\omega_c(x)$ describes the position-dependent cavity resonance frequency. Formally, we can expand the resonance frequency in powers of the displacement around some equilibrium position x_0,

$$\omega_c(x) = \omega_c(x_0) + \omega_c'(x_0)(x - x_0) + ... \tag{1.2}$$

Given the naturally weak force associated with light, the coupled mechanical degree of freedom is displaced by these forces by typically infinitesimal distances. This motivates expanding the resonance frequency of the cavity only up to linear displacements in Eq. (1.2) which defines the optomechanical interaction as given by

$$H_I = \omega_c'(x_0)(x - x_0) a^\dagger a = g_m(b + b^\dagger) a^\dagger a. \tag{1.3}$$

Here, we have re-written the displacement in terms of the fundamental creation and annihilation operators, $x - x_0 = x_{zp}(b^\dagger + b)$, where $x_{zp} = \sqrt{\hbar/(2m\omega_m)}$ is the quantum mechanical uncertainty associated with motion, which decreases with the effective mass m of the mirror. The single-photon, single-phonon optomechanical coupling strength is defined by

$$g_m \equiv \omega_c'(x_0) x_{zp}. \tag{1.4}$$

Even though we have linearized the displacement of the mechanical motion, the optomechanical interaction Eq. (1.3) still gives rise to non-linear equations of motion due to the product of three operators in the Hamiltonian. Without losses and thermal effects, starting from a classical (e.g., coherent) state, the interaction could eventually cause the state to become non-classical. This is interesting for a number of reasons; for example, it might be that optomechanical systems could be used to generate and manipulate non-classical states of light for quantum information processing. However, as the best demonstrated ratio of coupling strength to cavity linewidth thus far is $g_m/\kappa \sim 10^{-2}$ [8, 9], such quantum effects are too small to be observed.

To intuitively motivate the optomechanical Hamiltonian (1.1) we considered the simple picture of a moving mirror attached to a spring. Real optomechanical setups seldom look that way as the optomechanical description of a position-dependent optical resonance frequency is quite generic and successfully models a wide range of different systems. Examples of recently developed optomechanical geometries are shown in Fig. 1.3, with mechanical frequencies ranging from Hz to GHz, and masses ranging from kilograms to sub-picograms. The largest optomechanical structure and also the most sensitive to mechanical displacement to date is the gravitational wave detector (LIGO), which can resolve a change in length of less than 1/10000 the size of a proton. The length of its interferometer arms (4km) is affected by distortions of space itself. Other (a bit smaller) approaches to include a mechanical degree of freedom are gram-scale mirrors, which are optically trapped at mechanical frequencies of $\omega_m \sim 2\pi \times 200\,\text{Hz}$ [10] and coating of cantilevers [11–13] which constitute movable cavity mirrors. Optomechanical dynamics can also be achieved by placing membranes [14] inside a cavity mode. The resonances of whispering gallery mode micro-cavities [15, 16] can be affected by the elastic deformations of the dielectric structure itself, whereas in superconducting microwave resonators the capacitive coupling of a nanomechanical beam gives rise to the optomechanical interaction [17]. The smallest optomechanical systems are photonic crystal cavities where suspended membranes function as a mechanical oscillator [18] and photonic crystal nanobeam cavities, where the deformations of the beam itself supports vibrational frequencies in the GHz range [5] by having an effective mass of a fraction of a picogram.

While most systems rely on the deformation or displacement of resonator boundaries in order to achieve a position dependent resonance frequency, the trapping of nano-spheres inside a cavity mode constitutes an optomechanical platform as well [19–24].

As mentioned, all those experiments remain in the so-called optomechanical weak coupling regime, $g_m \ll \kappa$, where many photons inside the optical mode are required to see an appreciable effect on the vibrational mode. In the following we will demonstrate how to model this regime and give some intuition about its consequences.

1.2.1 *Weak optomechanical coupling*

Since $g_m \ll \kappa$, a large incident field must be sent in to drive the system. This enables one to develop a linearized theory of quantum fluctuations around the classical steady-state solution. The optomechanical Hamiltonian including a coherent laser drive

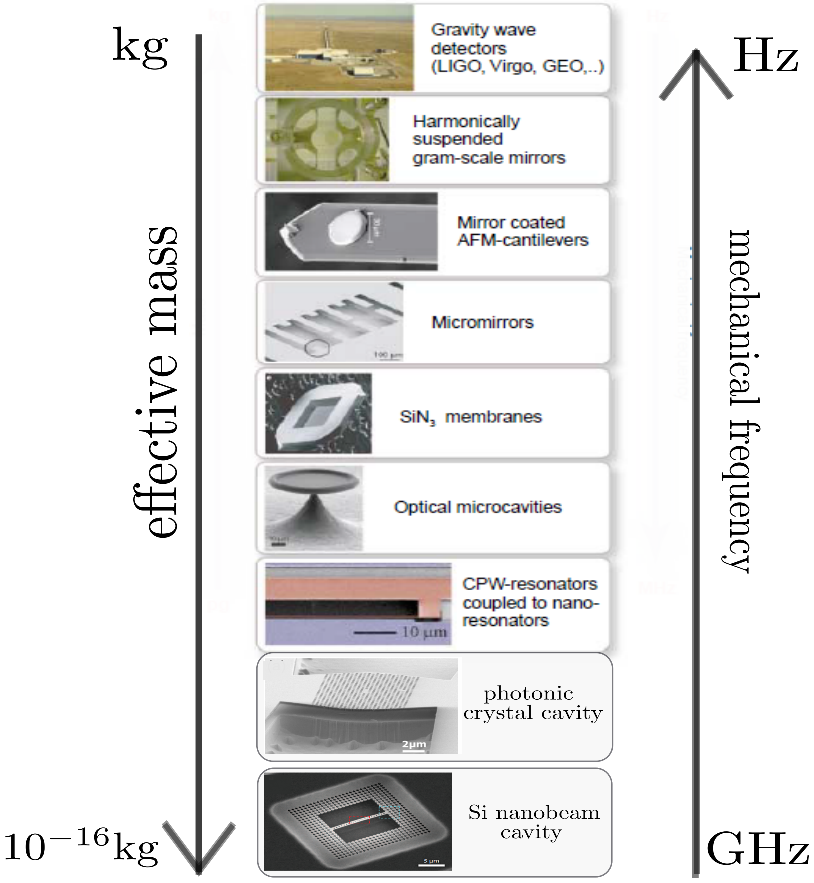

Figure 1.3: **Examples of recent optomechanical systems**
(Top to Bottom) Gravitational wave detectors [photo credit LIGO Laboratory], harmonically suspended gramscale mirrors [10], coated atomic force microscopy cantilevers [11], coated micromirrors [12, 13], SiN3 membranes dispersively coupled to an optical cavity [14], optical microcavities [15, 16], superconducting microwave resonators coupled to a nanomechanical beam [17], suspended membranes in photonic crystal cavities [18] and SI nanobeam cavities [5]. Parts of the figure and caption are taken from a review on optomechanics [25].

and written in a frame rotating with laser frequency ω_L is given by

$$H_o = -\delta_c a^\dagger a + \omega_m b^\dagger b + g_m(b^\dagger + b)a^\dagger a + \sqrt{\kappa_{ex}} E_0(a^\dagger + a). \quad (1.5)$$

Here, $\delta_c = \omega_L - \omega_c(x_0)$ is the detuning of the laser from the cavity frequency and κ_{ex} denotes the decay rate of the cavity into some particular external channel, which also serves as the source of injection of photons. With the standard Heisenberg-Langevin equations [26], one can find the steady-state equilibrium position $\bar{x}_0$ and the steady-state expectation value of the amplitude $\langle a \rangle = \bar{\alpha}$ for this Hamiltonian. The optomechanical interaction can be linearized by splitting the optical mode into this steady-state solution and quantum fluctuations δa around it:

$$a = \bar{\alpha} + \delta a. \quad (1.6)$$

The effect of the laser drive is then absorbed into the steady state solution $\bar{\alpha} \propto E_0$ and the last term of Eq. 1.5 can be omitted. The interaction Hamiltonian turns into

$$H_I = g_m(\bar{\alpha}^* + \delta a^\dagger)(\bar{\alpha} + \delta a)(b^\dagger + b). \quad (1.7)$$

The first term $g_m|\bar{\alpha}|^2(b + b^\dagger)$ just describes an average radiation pressure force. Intuitively, such a constant force pushing on the mirror just results in a new equilibrium position $\bar{x}_0$, and a corresponding static shift in the cavity resonance frequency $\omega_c(\bar{x}_0)$. We also omit the term proportional to $\delta a^\dagger \delta a$ as it is smaller by a factor of $\bar{\alpha}$ than the term we are interested in. Then, we end up with the "standard model" of (linearized) optomechanical interactions, which describes essentially every optomechanical experiment to date:

$$H_L \approx g_m \sqrt{\bar{n}_c}(\delta a^\dagger + \delta a)(b^\dagger + b). \quad (1.8)$$

Here, $\bar{n}_c = |\bar{\alpha}|^2$ is the mean intra-cavity photon number.

To get some intuition, we note that H_L enables a process where a photon is created ($\delta a^\dagger$), along with the creation or annihilation of a phonon. If the photon exits the cavity (due to the finite cavity losses κ), then this cycle has resulted in the heating or cooling of the mechanical energy, with the energy difference carried away by the outgoing photon (so-called Stokes or anti-Stokes sidebands). In particular, when $\omega_m > \kappa$ (sideband resolved) , one can use the narrow optical resonance to significantly enhance the cooling process over heating, by choosing the laser frequency $\omega_L \approx \omega_c(x_0) - \omega_m$ to be red detuned. This in principle provides a route to cool the mechanical motion to its quantum ground state.

For $\omega_m < \kappa$ (unresolved sidebands) the adiabatic response of the cavity field to the motion gives rise to the optical spring effect, where the vibrational frequency can be optically enhanced (spring) or reduced (anti-spring). All these effects can be completely understood from a classical perspective. Therefore we will now derive the classical (and linear) response of the optomechnical system, which is also called the susceptibility.

1.2.2 *Linear response: susceptibility*

Many interesting effects arising from cavity optomechanics can be explained classically. When the equations of motions can be linearized, the expectation values of the quantum Heisenberg-Langevin equations coincide with the classical observables. The linear response of a mechanical system to an external drive with frequency ω gives information about its resonance frequencies and damping or amplification rates. The total linearized Hamiltonian of the optomechanical system, written in a frame rotating with an external laser frequency ω_L is given by

$$H_{LO} = \frac{p^2}{2m} + \frac{1}{2} m\omega_m^2 (x - \bar{x}_0)^2 - \bar{\delta}_c a^\dagger a + (g/x_{zp})(a^\dagger + a)x - xF_{ext}(t). \tag{1.9}$$

The first term describes the kinetic energy of the mechanical motion with momentum p. Here, $\bar{\delta}_c = \omega_L - \omega_c(\bar{x}_0)$ is the detuning of the laser from the steady state cavity frequency. For simplicity we choose $\bar{x}_0 = 0$ and changed the notation from δa to a. We define the intra-cavity field enhanced optomechanical coupling strength $g = g_m \sqrt{\bar{n}_c}$. We added an external driving force $F_{ext}(t)$ shaking the mechanical system with frequency ω. The system dynamics under this Hamiltonian is described by standard Heisenberg-Langevin equations [26]. After taking the classical expectations values for the position $x = \langle x(t) \rangle$ and the cavity amplitude fluctuations $\alpha = \langle a \rangle$, the equations of motion are given by:

$$m\ddot{x} = -m\omega_m^2 x - m\Gamma_m \dot{x} + (g/x_{zp})(\alpha^* + \alpha) + F_{ext}(t) \tag{1.10}$$

$$\dot{\alpha} = (i\bar{\delta}_c - \frac{\kappa}{2})\alpha + i(g/x_{zp})x. \tag{1.11}$$

In addition to the unitary dynamics under H_{LO}, we have added the cavity decay rate κ and a mechanical damping rate Γ_m. These are linear coupled equations, which can be straightforwardly solved for $x(\omega)$ in frequency space, where we replace all variables $v(t)$ with their Fourier transforms $v(t) = \int d\omega e^{-i\omega t} v(\omega)$. The susceptibility $\chi(\omega)$ is then defined as the ratio between the motional amplitude and the external force, $x(\omega) \equiv \chi(\omega) F_{\mathrm{ext}}(\omega)$. It is given by

$$\chi(\omega) = \frac{1}{m(\omega_m^2 - \omega^2 - i\Gamma_m \omega) + \Sigma(\omega)}. \tag{1.12}$$

All effects originating from the optomechanical interaction are contained in

$$\Sigma(\omega) = \frac{g^2}{x_{zp}^2}\left(\frac{1}{(\bar{\delta}_c + \omega) + i\kappa/2} + \frac{1}{(\bar{\delta}_c - \omega) - i\kappa/2}\right) \tag{1.13}$$

which could be called the "optomechanical self-energy" [27] summarizing the effects of the optomechanical interaction.

1.2.3 *The optical spring effect and cooling/heating*

For $\Gamma_m \ll g \ll \kappa$, all dynamics take place in the vicinity of $\omega \approx \omega_m$ and we can approximate $\omega_m^2 - \omega^2 \approx 2\omega_m(\omega_m - \omega)$ and evaluate $\Sigma(\omega_m)$ at the bare mechanical frequency. Then the susceptibility (Eq. 1.12) takes a Lorentzian shape:

$$\chi(\omega) = \frac{1}{2m\omega_m}\frac{1}{(\omega_m + \delta\omega_{\mathrm{opt}}) - \omega - i(\Gamma_m + \Gamma_{\mathrm{opt}})/2}. \tag{1.14}$$

Thus, we are able to identify the optomechanically induced damping rate $\Gamma_{\mathrm{opt}} = -\mathrm{Im}[\Sigma(\omega_m)]/(m\omega_m)$ and mechanical frequency shift $\delta\omega_{\mathrm{opt}} = \mathrm{Re}[\Sigma(\omega_m)]/(2m\omega_m)$:

$$\Gamma_{\mathrm{opt}} = g^2\left(\frac{\kappa}{(\bar{\delta}_c + \omega_m)^2 + \kappa^2/4} - \frac{\kappa}{(\bar{\delta}_c - \omega_m)^2 + \kappa^2/4}\right) \tag{1.15}$$

$$\delta\omega_{\mathrm{opt}} = g^2\left(\frac{\bar{\delta}_c + \omega_m}{(\bar{\delta}_c + \omega_m)^2 + \kappa^2/4} + \frac{\bar{\delta}_c - \omega_m}{(\bar{\delta}_c - \omega_m)^2 + \kappa^2/4}\right). \tag{1.16}$$

Note that the effect of the optomechanical interaction is, as $g^2 \propto \bar{n}_c$, increasing linearly with laser power. The first and second terms in Γ_{opt} can be identified with anti-Stokes and Stokes scattering. In particular, the anti-Stokes process leads to cooling ($\Gamma_{\mathrm{opt}} > 0$) and its rate is maximized when $\bar{\delta}_c \approx -\omega_m$, such that the frequency of the scattered photon (which takes away a phonon of energy) aligns with the cavity resonance. Likewise, the Stokes process leads to heating ($\Gamma_{\mathrm{opt}} < 0$) and is maximized when $\bar{\delta}_c \approx \omega_m$. Note that for substantial heating/cooling to take place, the mechanical sidebands have to be resolved $\omega_m > \kappa$; otherwise both processes take place with an almost equal rate. The maximal cooling rate is $\Gamma_{\mathrm{opt}}^m = 4g^2/\kappa$.

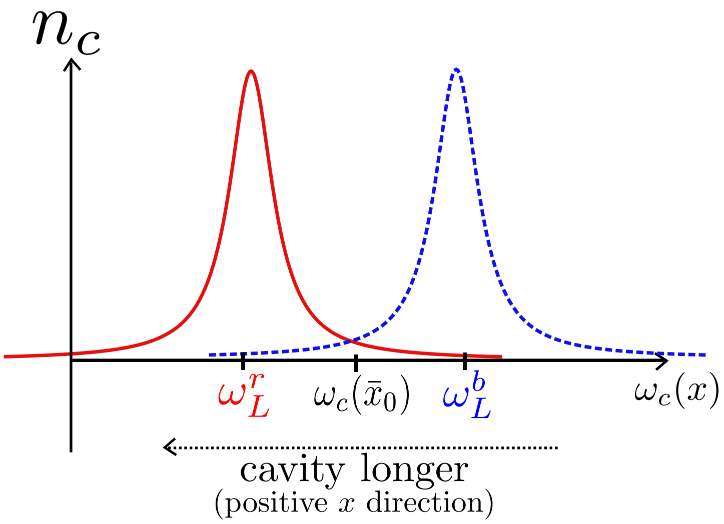

Figure 1.4: **Intra-cavity photon number** n_c as a function of cavity frequency $\omega_c(x)$ for a red detuned drive with frequency ω_L^r (red) and a blue detuned drive with frequency ω_L^b (blue). For $\omega_m \ll \kappa$, the intra-cavity intensity adiabatically follows the motion. For a blue detuned drive the intra-cavity intensity decreases as the cavity gets longer leading to spring hardening since $k_{opt} = -F'_{opt}(\bar{x}_0) \propto -n'_c(\bar{x}_0) > 0$. With the same argument, a red detuned drive causes the intra-cavity intensity to increase as the cavity gets longer leading to $k_{opt} < 0$ (anti-spring).

In the unresolved sideband regime $\kappa \gg \omega_m$, the shift in the mechanical frequency dominates over the damping rate, and takes the form

$$\delta\omega_{opt} \approx g^2 \frac{2\bar{\delta}_c}{\bar{\delta}_c^2 + \kappa^2/4}. \tag{1.17}$$

It follows that the mechanical frequency shift is positive for a blue-detuned laser (spring) and negative for a red detuned laser (anti-spring).

The intuition for the optical spring effect in the example of a moving mirror is given in Fig. 1.4, which shows the intra-cavity photon number n_c as a function of cavity resonance frequency ω_c for a blue detuned ω_L^b (blue, dashed) and a red detuned ω_L^r (red) drive. We first consider the blue-detuned case and small fluctuations of the mirror motion around its equilibrium position x_0. If the mirror displaces in such a way that the cavity becomes longer, then the cavity resonance detunes even further from the laser frequency. This results in a reduced intra-cavity photon number n_c, and a reduced radiation pressure force pushing the mirror outward (or equivalently, this appears as an extra force pushing the mirror back toward its equilibrium). The final result is an optical spring effect, where the optical contribution to the spring constant

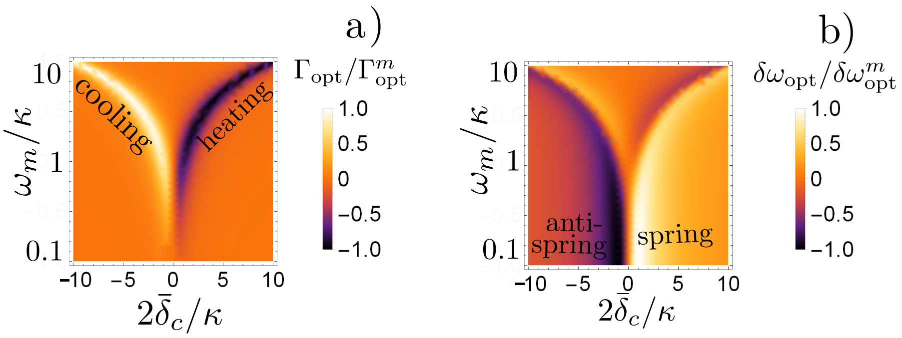

Figure 1.5: **Summary of standard regimes of optomechanics**
a) Optical damping rate $\Gamma_{\rm opt}$ normalized by its maximum value $\Gamma^{\rm m}_{\rm opt}$, as a function of detuning $\bar{\delta}_c$ and mechanical frequency ω_m (each of these normalized by the cavity linewidth κ). Cooling occurs for a red detuned ($\bar{\delta}_c < 0$) and heating for blue detuned ($\bar{\delta}_c > 0$) drive. Both processes dominate in the resolved sideband regime $\omega_m \gg \kappa$.
b) Optically induced shift of mechanical frequency $\delta\omega_{\rm opt}$ normalized by its maximum value $\delta\omega^{\rm m}_{\rm opt}$, as a function of detuning $\bar{\delta}_c$ and mechanical frequency ω_m (each of these normalized by the cavity linewidth κ). The optical spring effect dominates in the unresolved sideband regime $\omega_m \ll \kappa$. An optical anti-spring is created for a red detuned drive $\bar{\delta}_c < 0$ and spring hardening occurs for a blue detuned drive $\bar{\delta}_c > 0$.

$k_{\rm opt} = -F'_{\rm opt}(\bar{x}_0) \propto -n'_c(\bar{x}_0) > 0$, is proportional to the derivative of the photon number at the equilibrium position. A similar argument reveals that red-detuning gives rise to an anti-spring effect. We note that there would be no optical spring effect without the existence of a external restoring force as the mirror would just be pushed to infinity.

For $\bar{\delta}_c = \pm\kappa/2$ a maximum shift of $\delta\omega^{\rm m}_{\rm opt} = \pm 2g^2/\kappa$ can be achieved. A summary of the standard regimes of optomechanics is given in Fig. 1.5. In Fig. 1.5a), we plot the optical damping rate $\Gamma_{\rm opt}$, normalized by its maximum value $\Gamma^{\rm m}_{\rm opt}$ (Eq. (1.15)), as a function of $\bar{\delta}_c$ and ω_m/κ. One can see clearly that damping is most significant in the resolved sideband regime $\omega_m \gg \kappa$ and that cooling occurs for a red detuned ($\bar{\delta}_c < 0$) and heating for blue detuned ($\bar{\delta}_c > 0$) drive. In Fig. 1.5b), we plot the mechanical frequency shift $\delta\omega_{\rm opt}$, normalized by its maximum value $\delta\omega^{\rm m}_{\rm opt}$ (Eq. (1.16)) One can see that the optical spring effect dominates in the unresolved sideband regime $\omega_m \ll \kappa$ and that an optical anti-spring occurs for a red detuned drive $\bar{\delta}_c < 0$ and spring hardening occurs for a blue detuned drive $\bar{\delta}_c > 0$.

These effects have been ubiquitously seen in optomechanical systems. For example, sideband cooling is a standard procedure used to bring a mechanical system to close to its ground state, where the number of phonons $\langle b^\dagger b \rangle \approx 0$ [5, 28]. Mirror spring hardening of a Fabry-Pérot resonator [10, 29] and spring hardening of microlevers as a mirror in microcavities [30] have been demonstrated.

While a classical picture is indeed sufficient to understand the reduced dynamics of the mechanical oscillator, the linearized "standard model" of optomechanics nonetheless does allow for some interesting quantum functionalities. Formally, the Hamiltonian of Eq. (1.8), which is quadratic in creation and annihilation operators, implies that the system dynamics will only evolve within the space of so-called "Gaussian states", provided that the external driving and noise are classical (e.g., coherent state driving and thermal states) [31]. As a more formal description is beyond the scope of this introduction we will just provide some intuition here. First, the linearized model enables "quantum state transfer", in which an optical quantum state and a mechanical quantum state can be coherently converted into one another [32, 33]. This is in fact closely related to optomechanical cooling – specifically, a phonon is not removed into some inaccessible bath, but is in fact coherently converted into an anti-Stokes photon. The linearized model also enables entanglement between the mechanical and optical systems [34–36]. This arises from viewing optomechanical heating not as an incoherent process, but one where each added phonon is accompanied by the generation of a (correlated) Stokes photon. These processes can in turn be exploited for diverse processes such as a quantum memory based upon optomechanics [37], quantum coherent microwave-to-optical conversion [38], or heralded single-photon generation [39]. Despite this, Gaussian states only form a small portion of the total Hilbert space, and thus it would be highly desirable to go beyond the linearized Hamiltonian of (1.8).

1.3 NON-STANDARD REGIMES OF OPTOMECHANICS

In the previous section we have reviewed the standard regimes of optemechanics, where both the motion and the optical field have been linearized around the classical, steady-state values. In this section, we will introduce some additional regimes, with the goal of identifying and accessing richer phenomena than allowed by the linearized system. We will first give up on the linearization of the motional degree of freedom and afterwards explore strong optomechanical coupling, $g_m \gtrsim \kappa$, where the linearization of the cavity field breaks down.

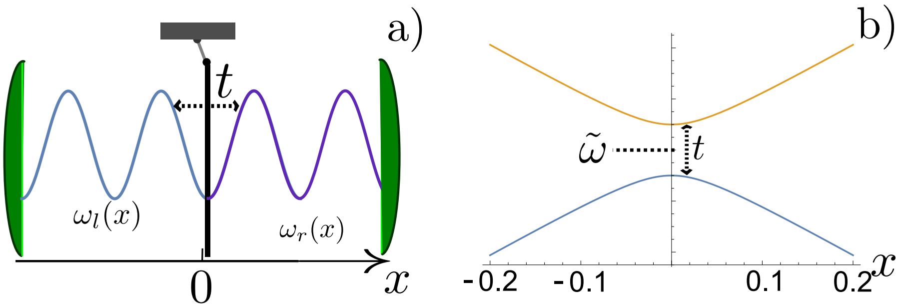

Figure 1.6: **Quadratic optomechanical coupling?**
a) Highly reflecting membrane in the middle of a cavity. The sytem can be viewed as two optical modes with frequency $\omega_l(x) = \tilde{\omega} - sx$ and $\omega_r(x) = \tilde{\omega} + sx$ coupled by a tunneling rate t.
b) Eigenenergies of system a) as a function of membrane displacement x with $t = 0.1$ and $s = 1$. Although the original Hamiltonian only contains linear optomechanical coupling plus linear cross-coupling, the eigenenergies behave like x^2 around $x = 0$ due to anti-crossing. This behavior has been incorrectly interpreted as quadratic optomechanical coupling [42].

1.3.1 *Non-linear motion*

In order to arrive at the optomechanical interaction Hamiltonian (Eq. 1.3) we expandend the frequency shift (Eq. 1.2) up to linear order. The next order term is proportional to x^2, whose quantum mechanical consequences we will briefly discuss now. The optomechanical interaction Hamiltonian with quadratic coupling is given by

$$H_I^{(2)} = g_m^{(2)} a^\dagger a (b^\dagger + b)^2. \tag{1.18}$$

The quadratic optomechanical coupling strength $g_m^{(2)} \propto x_{zp}^2$ is proportional to the zero-point motion squared, and thus extremely small for conventional optomechanical systems. Nonetheless, at least in theory, it has been shown that in the weak coupling regime $g_m^{(2)} < \kappa, \omega_m$, the cavity mode can again be strongly driven and its dynamics linearized. Now, however, the interaction with light in principle allows for motional squeezing and non-linear cooling due to the coupling terms proportional to $(b^\dagger)^2$ and b^2, which generate or annihilate pairs of phonons at a time [40]. On the other hand, the term $a^\dagger a b^\dagger b$ in principle allows for quantum non-demolition measurements of the phonon number, by measuring the phonon number-dependent optical cavity frequency [41]. The fact that this interaction term commutes with phonon number ensures that it is not perturbed by back-action.

Even though theoretically studied, quantum effects from quadratic optomechanical coupling have not been experimentally observed up to date. In previous experiments, static transmission spectra have been recorded for a membrane in the middle of a cavity [42, 43]. By moving the membrane by hand, one can map out an x^2 dependence of the cavity resonance frequencies, such as around a symmetric anti-node of the cavity. However, such a static measurement is not sufficient to conclude a Hamiltonian of the form (1.18). A counter-example where this approach breaks down is the following: Imagine a highly reflecting membrane in the center of a Fabry-Pérot cavity as illustrated in Fig. 1.6 (and incorrectly proposed for strong quadratic optomechanical coupling in [42]). The system can be modeled as two optical modes, occupying the left and right sides of the cavity, and interacting via the small but finite transmission allowed by the membrane. The Hamiltonian describing this situation is $H_T = \omega_l(x) a_l^\dagger a_l + \omega_r(x) a_r^\dagger a_r + t(a_l^\dagger a_r + a_l a_r^\dagger)$, where a_l and a_r are the photon annihilation operators for the left and right mode, respectively. The corresponding resonance frequencies $\omega_l(x) \approx \tilde{\omega} - sx$ and $\omega_r(x) \approx \tilde{\omega} + sx$ of these modes depend in first approximation on the linear position x of the membrane, where $\tilde{\omega}$ is the frequency of both modes if the membrane is at the center $x = 0$. The modes interact by tunneling through the membrane with rate t.

Fig. 1.6 shows a plot of the eigenfrequencies of this Hamiltonian as a function of membrane displacement x. Here, for the sake of demonstration, we assume $s = 1$ and $t = 0.1$ and work in dimensionless units. Measuring the eigenfrequencies of this system as a function of displacement would yield a scaling of x^2 around $x = 0$. However, it would be wrong to infer a quadratic optomechanical coupling from just this behavior, since the original Hamiltonian clearly just contains linear optomechanical coupling plus linear cross-coupling. It can be shown that the conditions for achieving QND measurement of phonon number with the Hamiltonian H_T are much more stringent, corresponding to attaining the single-photon, single-phonon strong coupling regime of optomechanics, $g_m > \kappa$ [44].

In order to resolve this issue, one would need to quantize the electromagnetic field with dielectric boundary conditions [45], which would provide a rigorous derivation of the starting Hamiltonian (at least for a model system). Another approach, which we describe in Chapter 3, is to use a single atom coupled to a cavity, whose Hamiltonian is already and unambiguously known.

While quadratic optomechanical coupling has been discussed in literature, one might also wonder if even richer effects could arise, if the mechanical motion is unconstrained and thus the functional form of $\omega_c(x)$ could be even more complex. We will discuss some of the consequences in Chapter 2 (in the classical regime) and Chapter 3 (quantum).

1.3.2 *Strong optomechanical coupling*

As mentioned in Sec. 1.2 the interaction Hamiltonian described by Eq. (1.3) is intrinsically non-linear. Although working in a linearized regime of dynamics (Eq. (1.8)) captures many interesting phenomena, it fails for single-photon strong optomechanical coupling $g_m \gtrsim \kappa$.

For resolved vibrational sidebands $\omega_m > \kappa$, strong optomechanical coupling leads to a photon blockade effect, which has been theoretically analyzed [46]. Here, the interaction is strong enough that one photon in the cavity essentially displaces the mechanical element enough that the cavity frequency shifts by more than a linewidth. Under certain conditions, this can result in the capability of the system to only resonantly transmit single photons at a time, resulting in a non-classical "anti-bunching" signal in transmission. Such anti-bunching is usually associated with two-level atoms. Thus, its observation would be highly exciting, and might invite a discussion of whether optomechanical systems could in principle replace atoms for quantum optical information processing.

We will now give more detailed intuition for the optomechanical photon blockade phenomenon, which exists in the resolved sideband regime. The system Hamiltonian is given by

$$H_{op} = \omega_m b^\dagger b + \omega_c(x_0) a^\dagger a + g_m(b^\dagger + b) a^\dagger a. \qquad (1.19)$$

From the interaction (last term) one can interpret that a given photon number Fock state $|n_c\rangle$ imparts a constant mechanical force of $\propto g_m \cdot n_c$. This force displaces the mechanical equilibrium position by $\delta x \sim -n_c \cdot x_{zp} g_m/\omega_m$. Putting that displacement back into the interaction, one can see that this displacement lowers the energy by $g_m^2 n_c^2/\omega_m$. The resulting energy spectrum of Hamiltonian (1.19) is illustrated in Fig. 1.7. Here, $|n_c, m\rangle$ denotes the state with n_c photons and m phonons. If the laser frequency is resonant with the transition $|0_c, 0\rangle \to |1_c, 0\rangle$ then a second photon entering the system is off resonant from the transition $|1_c, 0\rangle \to |2_c, 0\rangle$ by an amount $-2g_m^2/\omega_m$. If this nonlinearity is larger than the cavity linewidth, $g_m^2/\omega_m > \kappa$, then the first photon would be resonantly transmitted while the second photon would not, resulting in a non-classical "anti-bunched" transmitted field [46]. For this so-called "photon blockade" effect to occur, it is also necessary to maintain sideband res-

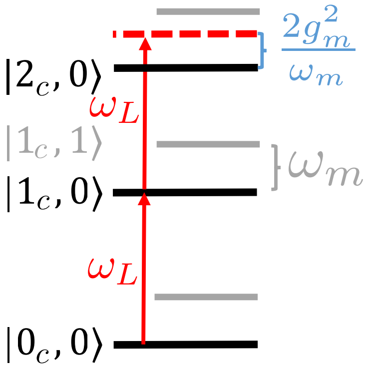

Figure 1.7: **Optomechanical photon blockade.** Spectrum of the optomechanical Hamiltonian (1.19). $|n_c, m\rangle$ denotes the state with n_c photons and m phonons. In this diagram, we focus on transitions involving states with $m = 0$ phonons (black lines), while other states ($m = 1$ shown here) are denoted by gray lines. A laser with frequency ω_L, which is resonant with the transition $|0_c, 0\rangle \rightarrow |1_c, 0\rangle$ (the zero-phonon line), cannot resonantly excite a second photon $|2_c, 0\rangle$ as optomechanical interactions shift the relative energy of this state by an amount $2g_m^2/\omega_m$.

olution, $\omega_m > \kappa$, to prevent the near-resonant transmission of the second photon via the excitation of phonon states $|2_c, m \neq 0\rangle$.

In Chapter 4 we demonstrate that an atom trapped in and dispersively coupled to a high finesse cavity constitutes an attractive platform for realizing this regime. In particular, we show that current experiments should be already able to obtain strong optomechanical coupling and resolving mechanical sidebands. This can then be experimentally verified by the anti-bunched statistics of the transmitted light.

Consequences of the strong optomechanical coupling regime with unresolved sidebands $\kappa \gg \omega_m$ are thus far unexplored in literature. This is perhaps because with conventional optomechanical systems one cannot cool to the ground state in the first place in this regime, and thus any quantum effects that arise would need to be observed on top of a thermal background of phonons. In Chapter 3, we will provide for the first time a theoretical analysis of this regime, which is naturally reached by dispersively coupling atoms to cavities with small mode volumes. The use of atoms to explore this regime is novel, as the atomic motion can be separately cooled to the ground state by standard techniques, and is highly decoupled from any thermal or decoherent environment. This allows novel quantum effects to emerge.

1.4 OVERVIEW OF THE THESIS RESULTS

In the previous sections we have reviewed the standard regimes of optomechanics where the motion and the field have been linearized leading to the "optical spring" effect and cooling and heating of mechanical motion. These effects have been both theoretically analyzed and also experimentally observed. Then we focused on non-standard regimes of optomechanics, where either the motion or the field cannot be linearized. Those effects have not been observed yet. Now we will give an overview of the thesis results, which on one hand analyze additional novel regimes within optomechanics for the first time, and on the other hand propose specific systems in which non-standard regimes of optomechanics could be realized experimentally.

1.4.1 *Self-induced back-action (SIBA) optical trapping in nanophotonic systems*

The beginning of our scientific journey was motivated by a couple of experiments [47, 48], which observed a qualitatively new trapping behavior in nanophotonic cavities leading to strongly reduced local intensities experienced by the trapped particles. For example, by trapping nano-particles inside a coherently driven photonic crystal cavity, long trapping times (up to 20min) without apparent photo-thermal damage or photo-bleaching of the particles have been observed [48]. In particular, as presented in Fig. 1.8a), they measured the particle induced resonance shift in time, which shows the optical response of the cavity in the presence or absence of a particle using a scanning rate of 1 Hz. Additionally, in Fig. 1.8b), they provide a snapshot, which shows the cavity transmission with and without a trapped particle as a function of laser wavelength. One can see an average resonance shift of 1.8 nm, which is larger than the cavity linewidth. This clearly shows the capability of the particle to shift the cavity in and out of resonance and as a consequence turning its own trapping field on and off. Thus, one can conclude that the particle plays an active role in the trapping mechanism by acting back on its own trapping field, thus coining the term "self-induced back-action trapping" (SIBA).

Furthermore, the group of Romain Quidant at ICFO was running an experiment of trapping gold nano-particles in plasmonic cavities during that time and was seeing similar effects. In Fig. 1.8c) we see their measured transmission as a function of time changing around 50% for an empty cavity compared to a cavity containing a particle. However, both experiments were lacking a simple theoretical model describing SIBA, which

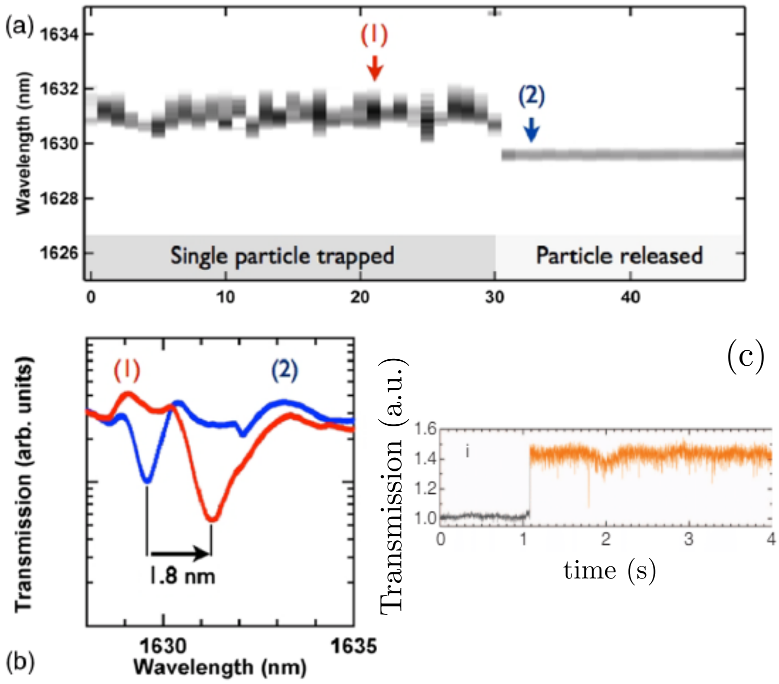

Figure 1.8: **Experimental demonstration of a particle-induced resonance frequency shift.**
(a) Record of the time evolution of the cavity spectrum while a particle is trapped in a photonic crystal cavity and after it is released.
(b) Snapshots from (a), displaying an average resonance shift of 1.8 nm from the unloaded cavity resonance, which is larger than the bare cavity linewidth (width of the blue peak). **c)** Transmission of an empty (grey) or with a trapped particle (orange) plasmonic cavity as a function of time, normalized to the transmission of an empty cavity.
Plots a) and b) are taken from [48] and plot c) is taken from [49].

could possibly be used to boost its performance and understand the advantages of SIBA trapping over conventional optical tweezers. To find such a theory became then our task. I want to mention that stimulating discussions with Romain Quidant and learning experimental details from Pau Mestres and Johann Berthelot made this process very enjoyable. In Chapter 2 we will present such a simple theoretical model which fully captures the physics of SIBA and provides a clear prescription of how to optimize back-action effects. Some of the insights from this theory helped Pau Mestres et al. to nicely demonstrate the back-action of the particle on its own trapping potential with their original experimental setup [49]. We will now give a short overview of our approach to model SIBA and the remarkable results.

As has been experimentally observed, the key physics is that the position of the trapped particle alters the resonance frequency of the cavity, which results in a strong interplay between the intra-cavity field intensity and the forces exerted. As this sounds a lot like standard optomechanics, we will apply its formalism to this problem. However, the frequency shift $\omega_c(x)$ needs to be treated globally as the particle is allowed to freely diffuse through the cavity, and in contrast to standard optomechanics (where there usually exists a natural restoring force for the mechanics), the particle only experiences forces from the externally driven cavity mode itself. As the SIBA effect has been observed by trapping particles in water at room temperature, we conclude that this effect is purely classical.

In Chapter 2 we will show that SIBA trapping exhibits several surprising features, when compared to conventional optical tweezer traps. First, the particle is effectively trapped in an intensity minimum, even if it is nominally high-intensity seeking, which explains the strong reduction of photo-thermal damage seen by experiments. Furthermore, we show that back-action can be exploited to create traps with strongly sub-wavelength spatial features, even if the cavity mode itself obeys the diffraction limit, even allowing a square well potential for a large enough "back-action parameter". The spatial features of this trap can also be dynamically shaped using only changes in laser frequency. We believe that these properties of SIBA will have important implications for future trapping technologies.

1.4.2 *Quantum SIBA with a single atom in a nano/micro-cavity (unresolved sidebands)*

In the previous section, we solved for the classical expectation values as our system of interest was far from any quantum behavior. However, motivated by the observation that the SIBA effect provides us with a square well potential, we were very curious about whether such an analysis holds up in the quantum domain. In particular, a square well is interesting due to its highly anharmonic spectrum, and might be useful to create, e.g., a two-level phonon. For this reason, the next step of our journey is to derive a full quantum master equation capable of describing the SIBA effect in the quantum regime, which we will do in Chapter 3.

Even assuming that the square-well potential holds in the quantum domain, a quick analysis shows that the energy scales associated with realistic dielectric particles are much too low to make preparation of the ground state realistic. We thus turn to a single atom in a cavity, with the goal of taking advantage of its light mass and decoupling of its motion from a thermal bath.

There are already many experiments coupling single neutral atoms [50–53] or ions [54–60] to high-finesse cavities. In particular, experiments [50, 51, 61, 62] now routinely reach the strong coupling regime of cavity QED, wherein an atom maximally coupled to the cavity (in an anti-node) shifts the bare cavity frequency by more than a linewidth. Moving the atom by a quarter-wavelength to a node eliminates this shift. Thus, a zero-point motion on the order of a fractional wavelength is sufficient to attain optomechanical strong coupling, which is easily achievable given the light single-atom mass.

Thus, we derive a full master equation for a single atom in a coherently driven nano-cavity. Although the quantum calculation yields an expectation value for the force, whose integral corresponds to the classical square well potential, the square well potential does not appear as the Hermitian Hamiltonian of the particle itself. In other words, a significant part of the classical force comes from cavity *dissipation*, and the entanglement that builds up between scattered photons and the position of the atom.

We decided to shift our attention further onto the entanglement between light and motion. To intuitively understand how strong position-photon entanglement arises, we note that when $g_m > \kappa$, the uncertainty of the zero-point motion itself translates into an uncertainty of the cavity resonance frequency that is much larger than the linewidth. Thus, observing the reflection or transmission of a single incident photon (revealing an off- or on-resonance cavity) is consistent only with the atom being located or not in a spatial region much smaller than the zero-point uncertainty. This regime naturally emerges in the strong optomechanical coupling regime with unresolved mechanical sidebands $\kappa > \omega_m$. We realize that there are already many experiments focusing on achieving strong coupling between a photon and the atomic internal degree of freedom within the field of cavity QED and we discovered that this same resource also naturally enables one to reach this optomechanical strong coupling regime. We thought that one experimental candidate system for our theory could be a new fiber-cavity setup of Tracy Northup in Innsbruck.

Funny side story: Before we realized that strong optomechanical coupling could be achieved within cavity QED I met Tracy on a conference in Benasque where she explained me her fiber cavity experiment in which she strongly couples single $^{40}\mathrm{Ca}^+$ ions to a cavity mode. We also discussed how she could model optomechanics with her system and what she could measure and things looked really interesting. However, in the end she accidentally gave me the parameters from an older experiment of a high finesse Fabry-Pérot cavity (well, most likely I confused it). Looking at those parameters at home I was first disappointed, as in that particular experiment mechanical sidebands were resolved $\omega_m > \kappa$ and thus our theory was not valid. However, a quick calculation with those parameters showed that she would be able to reach the strong optomechanical coupling regime with resolved sidebands (the holy grail of optomechanics!) with her older setup. Furthermore, she would be able to show that she reached it by demonstrating optomechanically induced photon blockade for the first time. So, out of this misunderstanding, a collaboration and a new resarch project was born which we will discuss now.

1.4.3 *Reaching the optomechanical strong coupling regime with a single atom in a cavity (resolved sidebands)*

As mentioned in Sec. 1.3.2, in order to reach the optomechanical strong coupling regime, a zero-point mechanical displacement should shift the frequency of the optical resonator by an amount comparable to its linewidth, which is difficult due to the large mass of conventional mechanical elements and the implied small zero-point motion. Finding a platform where this single-photon strong coupling regime of optomechanics can be explored constitutes a very important goal of the field.

As a specific example, we show theoretically that one can observe optomechanically induced photon blockade in realistic cavity QED setups, where a non-classical anti-bunched field is produced as the system is unable to transmit more than a single photon at a time. We also describe how this optomechanical behavior can be clearly distinguished from, and dominate over, the usual anti-bunching associated with the two-level nature of the atom. Experimentally showing photon blockade induced by motion proves that one really has reached the strong coupling regime of optomechanics and we anticipate that the proposed platform of single atoms coupled to a cavity will also enable many other exotic new regimes of optomechanics to be identified and explored.

Part II

RESULTS

2

SELF-INDUCED BACK-ACTION OPTICAL TRAPPING IN NANOPHOTONIC SYSTEMS

2.1 INTRODUCTION

Optical trapping is one of the most important experimental tools in physics and life sciences because it enables precise control over small dielectric particles [4]. Famous examples of its use are optical levitation and cooling of nanoscale particles [23, 63–66], trapping of bacteria [67] and cells [68], optical sorting in microfluidic channels [69], the manipulation and stretching of DNA [70], and recently, even trapping of individual HIV-1 viruses [71]. However, the difficulty of trapping a particle generally increases with decreasing size, due to the decreased optical response of the particle. This requires a commensurate increase in field intensity to maintain trap stability, and leads to associated problems such as thermal or material damage. Another limiting factor is the diffraction limit, which constrains the length scale over which fields can vary, and thus the stiffness or possible spatial features that a trap can possess.

A number of experiments in recent years have migrated from trapping in free-space beams to the fields generated in nano-optical resonators [47, 48, 72–75] as illustrated in Fig. 2.1. Such a paradigm can enable some technical advantages. For example, the resonator allows one to build up a higher intensity seen by the particle within the structure compared to the input, thus relaxing input power requirements. Engineering the nanophotonic structure also provides some flexibility over the field profile, and thus the trapping potential. However, it is clear that simply replacing the input field with the enhanced one does not relax any requirements from the standpoint of intensity seen by the particle. Therefore it remains an open question whether one can circumvent these seemingly fundamental trade offs between particle size and the intensities required to achieve given trap depths, frequencies, and spatial confinement. At the same time, doing so would have significant implications for optical manipulation as a tool in physics, chemistry and biology.

In this context, a number of experiments have observed qualitatively new trapping behavior in nanophotonic cavities [47, 48]. The key physics is that the position of the trapped particle alters the resonance frequency. This results in a “self-induced back-action" (SIBA) effect in which the motion dynamically af-

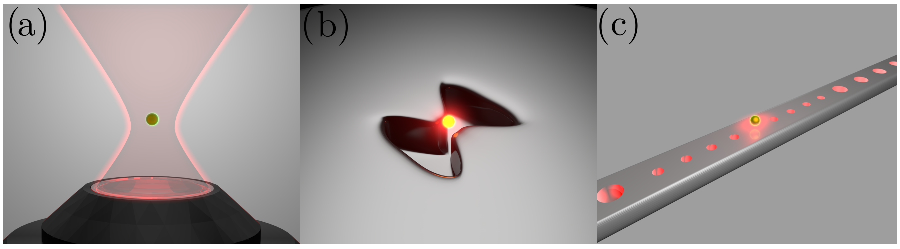

Figure 2.1: **Schematic illustration of trap configurations.** a) A dielectric particle trapped with an optical tweezer in free space, b) a plasmonic cavity (*e.g.*, a metallic bowtie antenna), c) a photonic crystal cavity.

fects the build up of intra-cavity intensity, and thus the optical force exerted.

Here, we develop a general theoretical model for SIBA. Using such a model, we show how parameters can be chosen to maximize the effects of back-action, and that a single "back-action parameter" $\eta \propto Q \cdot V/V_m$, proportional to the resonator quality factor and the ratio of particle to cavity mode volumes, characterizes the performance of any optimized system. In particular, the back-action parameter indicates how many line widths the particle can shift the cavity resonance frequency due to its movement. For large η, large shifts in the cavity detuning relative to the laser frequency as the particle moves can induce strong changes in the intra-cavity intensity. Under these circumstances, and when properly optimized, such a trap yields very different trade-offs between intensities, trap depth, and confinement, which should have significant consequences for optical trapping technology. Specifically, we show that back-action can be exploited to create traps with strongly sub-wavelength spatial features, even if the cavity mode itself obeys the diffraction limit. The spatial features of the trap can also be dynamically shaped using only changes in laser frequency. Furthermore, the particle can effectively be trapped in a dynamical intensity minimum, even if it is nominally high-intensity seeking, which can strongly reduce the effects of photo-thermal damage. Finally, we discuss the possibilities for implementation in nanoplasmonic (Fig. 2.1b)) and photonic crystal (Fig. 2.1c)) systems.

2.2 OPTICAL TWEEZERS

We first briefly review the properties and limits of trapping with free-space optical tweezers. Considering a small dielectric particle whose dimensions are much smaller than the optical wavelength $d \ll \lambda$, its response to a monochromatic beam with frequency ω is that of a point dipole with induced dipole moment $p_{\text{ind}} = \alpha(\omega)E(x)$. The interaction between the induced dipole and the field itself results in a stored (potential) energy. This leads to the well-known potential for optical trapping in free space, such as by using an optical tweezer [4]:

$$U_T(x) = -\frac{1}{4}\mathrm{Re}(\alpha(\omega))|E(x)|^2 \tag{2.1}$$

where $\alpha(\omega)$ is the frequency dependent polarizability of the particle and $|E(x)|^2 \propto I(x)$ is the peak electric field amplitude squared at the particle position x, which is proportional to the intensity $I(x)$. In the following, we will focus on the case where the polarizability is positive and largely frequency independent, which models well a typical dielectric particle. In this case, the dielectric particle is trapped around points of local maximum intensity. For sub-wavelength particles, the polarizability is proportional to particle volume, $\alpha(\omega) \propto V$. It can thus be seen that the trapping of smaller particles requires a commensurate increase in intensity to maintain a fixed trap depth. Furthermore, the spring constant around the trap minimum x_{min}, $k_{\mathrm{spring}} = U_T''(x_{\mathrm{min}}) \lesssim \frac{V \cdot I}{\lambda^2}$, in addition to being proportional to the beam intensity I and particle volume V, is at best proportional to the inverse of the optical wavelength squared, as the diffraction limit sets this as the minimum scale over which free-space optical fields can vary.

2.3 TRAPPING IN NANOSCALE RESONATORS

We now examine the case where the particle is trapped in a nanoscale cavity. Our formalism is quite general, covering equally systems such as plasmonic and photonic crystal cavities, and trapping in vacuum or fluid environments. Qualitatively, the new feature of such a system is that the resonance frequency of the cavity depends on the particle position, enabling the particle motion to feed back on its trapping potential. We then distinguish the regimes in which this system gives rise to standard optical trapping as in Eq. (2.1), versus a novel “back-action" trapping mechanism.

A general model of this system is given by following Hamiltonian:

$$H = \hbar\omega_c(x_p)a^\dagger a + \hbar\sqrt{\kappa_{ex}}E_0\left(a^\dagger e^{i\omega_L t} + a e^{-i\omega_L t}\right) + \frac{p^2}{2m} \tag{2.2}$$

where $\omega_c(x_p)$ is the resonance frequency of the optical cavity as a function of particle position x_p and a is the annihilation operator of the cavity mode. κ_{ex} denotes the decay rate of the cavity into some particular external channel (such as free-space radiation, coupling fiber, etc.), which also serves as the source of injection of photons into the cavity with number flux E_0^2 and frequency ω_L. The last term, $E_{kin} = \frac{p^2}{2m}$, describes the kinetic energy of a particle with momentum p and mass m. In addition to the external coupling, we assume that the cavity has an intrinsic loss rate κ_{in}, such as through material absorption or scattering losses. The total cavity linewidth is thus $\kappa = \kappa_{in} + \kappa_{ex}$. In principle, the particle also contributes a position-dependent loss term $\kappa(x_p)$ due to its scattering of light out of the cavity mode. While this term could be explicitly included in the analysis, this position-dependent effect is negligible under reasonable conditions as the scattering rate $\propto \frac{V^2}{\lambda^6}$ rapidly falls off for sub-wavelength sizes, as shown in Appendix A.2. Thus, the quality factor of the resonator is defined as $Q = \omega_c/\kappa$, where ω_c is the empty cavity resonance frequency.

The system dynamics under the Hamiltonian of Eq. (2.2) and system losses are described by standard Heisenberg-Langevin equations [26]. As the regime of interest for trapping is far from any quantum behavior, we proceed to solve their classical expectation values. We neglect damping of the mechanical motion and the effect of a thermal environment, which do not influence the optical force and can be added independently later on. The equations of motion then read

$$\frac{dx_p}{dt} = \frac{p}{m} \tag{2.3}$$

$$\frac{dp}{dt} = -n(x_p)\hbar\omega_c'(x_p) \tag{2.4}$$

$$\frac{d}{dt}\beta = i\left(\omega_L - \omega_c(x_p)\right)\beta - \frac{\kappa}{2}\beta + i\sqrt{\kappa_{ex}}E_0 \tag{2.5}$$

where $\beta = \langle a \rangle$ is the expectation value of the photon amplitude while $n = |\beta|^2$ is the expectation value of the photon number in the resonator. We note that even in state-of-the-art photonic crystal cavities, the achievable quality factor $Q = \omega_c/\kappa \approx 10^6$ results in decay times of $\kappa^{-1} \sim 1$ ns that are significantly shorter than the timescales of motion [76]. Thus, this motivates an approximation $\frac{d\beta}{dt} \approx 0$ where the cavity is able to instantaneously respond to the particle motion.

Before solving equations (2.3-2.5), we want to examine how strongly the particle affects the resonance frequency. To quantify this, we compare the frequency shift $\delta\omega_c(x_p) = \omega_c(x_p) - \omega_c$ with half of the line width $\kappa/2$ of the resonator, where ω_c is the resonance frequency of the empty cavity. Within lowest order perturbation theory, where the particle induces a frequency shift much smaller than the bare cavity frequency, it can be shown that (see Appendix A.1):

$$\frac{2\delta\omega_c(x_p)}{\kappa} = -\eta \cdot f(x_p). \tag{2.6}$$

Here, we have defined the dimensionless back-action parameter $\eta = \frac{\alpha(\omega)}{\epsilon_0 V_m} Q$, where V_m is the cavity mode volume. $f(x)$ is the dimensionless spatial intensity profile of the empty cavity, normalized to be 1 at the intensity maximum. Thus, as $0 \leqslant f(x) \leqslant 1$, the back-action parameter η characterizes how many linewidths (half-width half-maxima) the particle can shift the resonance frequency of the cavity moving from the minimum $f(x) = 0$ to the maximum of the mode profile. For sub-wavelength dielectric particles the polarizability $\alpha(\omega) \propto \epsilon_0 V$ is proportional to the particle volume, with the pre-factor depending on the particle refractive index and shape [77]. Thus, achieving a large back-action parameter requires a sufficient combination of large cavity quality factor and ratio of particle to cavity mode volume, $\eta \propto Q \cdot V/V_m$. When the particle size is larger than $kr \gtrsim Q^{-1/6}$ (with $k = 2\pi/\lambda$), the effect on the quality factor due to light scattering by the particle cannot be neglected anymore as shown in Appendix A.2. We note that within the approximations described above, our equations are rigorous, although numerical simulations would generally be needed to accurately obtain the mode volume, the intensity profile $f(x)$, and polarizability α for complicated experimental configurations.

The expectation value of the intra-cavity photon number $n(x_p) = |\beta|^2$ reads:

$$n(x_p) = \frac{4E_0^2 \kappa_{ex}}{\kappa^2} \frac{1}{1 + \left(\eta f(x_p) + \tilde{\Delta}\right)^2} \tag{2.7}$$

where we have defined the dimensionless detuning between the laser and empty cavity frequencies, $\tilde{\Delta} = 2(\omega_L - \omega_c)/\kappa$. From Eq. (2.7), one sees that there are certain positions of the particle x_r that cause the driving laser to become resonant with the (frequency-shifted) cavity, $\tilde{\Delta} + \eta f(x_r) = 0$, and where the intra-cavity photon number is maximized. We call these positions the resonant positions x_r, which can be chosen by adjusting the laser frequency ω_L. Note that in arbitrary dimensions the resonant positions $\vec{x}_r$ are contour points/lines/surfaces in 1D/2D/3D and follow the symmetry of the mode profile, see Fig. 2.2. Inserting Eq. (2.7) into Eq. (2.4) and integrating the negative force with respect to x_p yields the general potential for trapping in resonators:

$$U(x) = -2\hbar E_0^2 \frac{\kappa_{ex}}{\kappa} \arctan\left[\eta f(x) + \tilde{\Delta}\right]. \tag{2.8}$$

We will proceed by looking at different regimes of this potential: First we consider the regime where the particle induces a shift on the cavity resonance frequency that is negligible compared to its linewidth, which corresponds to $\eta \ll 1$ from our

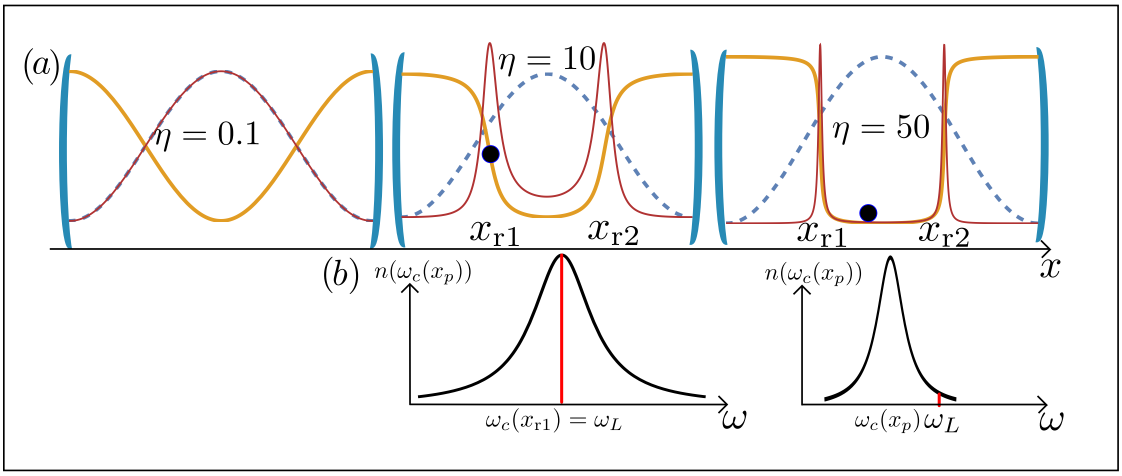

Figure 2.2: **Back-action trapping in the fundamental mode of a Fabry-Perot cavity**, with dimensionless intensity profile $f(x) = \cos^2(kx)$ (dashed blue curve). a) In the regime of small back-action parameter ($\eta = 0.1$), the intra-cavity intensity is not significantly affected by the particle motion. Thus, the local intensity $I(x_p)$ seen by the particle (red) is directly proportional to $f(x)$, while the trapping potential $U(x) \propto -f(x)$ (yellow). For an increasing back-action parameter $\eta \gg 1$ the seen local intensity $I(x_p)$ forms sharp peaks centered around the resonant points x_r and the trapping potential $U(x)$ converges to a square well potential. b) Spectra of intra-cavity photon number $n(\omega_c(x_p))$ taken at the instantaneous particle positions shown in the $\eta = 10$ and $\eta = 50$ cases, respectively. For $\eta = 10$, we consider the case where the particle is instantaneously located at one of the resonant positions x_{r1}, such that the laser frequency is resonant with the cavity at this moment to generate a large intra-cavity intensity. For $\eta = 50$, the particle is far from the resonant positions, and the large detuning of the laser from resonance strongly suppresses intra-cavity intensity. The vertical scales of these plots are in arbitrary units.

definition in Eq. (2.6). Then, the movement of the particle does not significantly change the intra-cavity intensity, which recovers the optical tweezer regime. In particular, expanding Eq. (2.8) for small η, one finds that $U_T(x) = -2\hbar\frac{\kappa_{ex}}{\kappa}E_0^2\frac{\eta}{1+\tilde{\Delta}^2}f(x)$. Using the definition of $\eta = \frac{\alpha(\omega)}{\epsilon_0 V_m}Q$ and identifying $|E(x)|^2 = 8\frac{\hbar}{\epsilon_0 V_m}\frac{\kappa_{ex}}{\kappa}QE_0^2\frac{1}{1+\tilde{\Delta}^2}f(x)$ as the time averaged intra-cavity field amplitude, we see that $U_T(x)$ reduces to the optical dipole potential in Eq. (2.1). In this regime, the potential depth increases linearly with Q (i.e., with η), reflecting the effect of a built-up intra-cavity intensity. The different regimes are illustrated in Fig. 2.2 where we choose the first harmonic of a Fabry-Perot cavity as a mode profile.

2.4 TRAPPING WITH BACK-ACTION

We now investigate the very different trap properties that emerge in the regime $\eta \gg 1$.

An increase in the quality factor initially produces an increased trap depth for values $Q \lesssim \pi V_m/V$ (at which point $\eta \sim 1$). For larger values, however, $\eta \gg 1$ and the arctan in Eq. (2.8) saturates between the values of $\pm\pi/2$, yielding a trap depth of $\delta U = 2\pi\hbar E_0^2\frac{\kappa_{ex}}{\kappa}$. Significantly for $\eta \gg 1$, the depth no longer depends on Q nor the particle properties, and is only dependent upon the input intensity. The origin of this saturation can be understood by first considering Fig. 2.2, which shows that the intra-cavity intensity as a function of particle position forms sharp peaks around the resonant positions x_r for $\eta \gg 1$. From Eq. (2.7) it follows that their width is in good approximation $\approx \frac{2}{\eta f'(x_r)}$ and it is only within this narrow spatial region (scaling like $\eta^{-1} \propto Q^{-1}$) that the cavity exerts significant forces on the particle. At the same time, the peak intra-cavity photon number at $x_p = x_r$ (and thus the peak force) grows linearly with Q. Thus, the maximum work that the cavity can do to keep the particle in the trap, as a product of force and distance, becomes independent of Q in the high back-action limit.

Note that the trapping potential turns into an approximate square well if the distance between the intra-cavity intensity peaks is larger than their width $d = |x_{r2} - x_{r1}| \gg \frac{2}{\eta f'(x_r)}$. The wells are (symmetrically) centered around the mode profile maximum x_0, see Fig. 2.2. Remarkably, the resonant positions x_r can be changed with laser frequency, which provides a convenient mechanism for dynamic trap shaping in contrast with conventional optical tweezers.

Another interesting property of the trap in the high back-action regime is that around the minimum x_0 of the potential, the intra-cavity photon number is strongly suppressed due to the large detuning from resonance. Thus, the particle is effectively trapped in a dynamical intensity minimum, despite the fact that it has positive polarizability and is thus nominally high-intensity seeking. This would have tremendous consequences in the reduction of thermal damage due to optical absorption by the particle. Motivated by this observation, we seek to quantify how much the time-averaged intensity seen by the particle can be reduced.

We define the time-averaged experienced intensity $\langle I_{\text{exp}} \rangle_t$ as the local intensity experienced by the particle at its position, averaged over one motional period T. It is thus given by

$$\langle I_{\text{exp}} \rangle_t = \frac{c\hbar\omega_L}{2V_m T} \int_0^T n(x_p(t)) f(x_p(t)) dt \tag{2.9}$$

where $x_p(t)$ is a solution to the differential Eq. (2.4) together with Eq. (2.7). In order to proceed further, we consider a simple case of the fundamental mode of a 1D Fabry-Perot cavity, $f(x) = \cos^2(kx)$ with $k = \pi/L$, where $L = \lambda/2$ is the cavity length. Although we have switched to a specific model to illustrate the back-action mechanism, we believe the overall conclusions are generally valid. A finite temperature of the environment can be taken into account by averaging the results for different maximal kinetic energies E_{kin} (kinetic energy of the particle in the trap minimum) according to a Boltzmann distribution.

We have evaluated Eq. (2.9) by numerically solving the equations of motion (2.3)-(2.5). In Fig. 2.3, we plot the time-averaged experienced intensity $\langle I_{\text{exp}}(\eta) \rangle_t$ normalized by the value in the optical tweezer regime $\langle I_{\text{exp},T} \rangle_t$, as a function of back-action parameter η. As seen before, the optical tweezer regime is reached by taking $\eta \ll 1$. To make a fair comparison, we enforce that the trap depths in the two cases are equal, $\delta U(\eta) = \delta U_T$. For a fixed x_r, the figure shows a significant reduction in time-averaged intensity for high back-action parameter, which also depends on the ratio of kinetic energy E_{kin} to trap depth δU. In the high back-action regime, it is possible to derive an analytic expression (see Appendix A.3):

$$\lim_{\eta \to \infty} \langle I_{\text{exp}}(\eta) \rangle_t = \frac{2c\epsilon_0}{\alpha(\omega)} \frac{f(x_r)}{|f'(x_r)|} \frac{E_{\text{kin}}}{x_r} \tag{2.10}$$

A new feature of the back-action trap is the gradual decoupling between trap depth and the spatial region $\delta x = |x_{t2} - x_{t1}|$ (x_{t1} and x_{t2} are the classical turning points) to which the particle is confined. For large enough η they decouple completely since the classical turning points converge to the resonant positions (i.e., the edges of the square well) and thus $\delta x \to d$. In this regime, confinement only depends on laser frequency, whereas trap depth only depends on laser power. This independent control again highlights the ability to dynamically reshape the trap. In contrast, in the optical tweezer regime, the trap depth, kinetic energy and confinement are inevitably connected.

Instead of comparing the experienced intensity at fixed trap depth, we can also investigate the trade-off between intensity and confinement $\delta x = d$ in the large back-action limit. The locations of the trapping wells are always centered around the mode profile maximum $x_0 = 0$. For small x_r, an asymptotic expansion yields $\frac{f(x_r)}{|f'(x_r)|} \approx \frac{1}{2k^2 x_r}$. Thus, for high back-action and strong confinement, we obtain $\langle I_{\mathrm{exp}} \rangle_t \approx \frac{4c\epsilon_0}{\alpha(\omega)} \frac{1}{(k\delta x)^2} E_{\mathrm{kin}}$. Interestingly, expanding Eq. (2.1) for the optical tweezer around the bottom of a standing wave potential also produces $\langle I_{\mathrm{exp},T} \rangle_t \approx I(x_0) \approx \frac{4c\epsilon_0}{\alpha(\omega)} \frac{1}{(k\delta x)^2} E_{\mathrm{kin}}$, which seems to indicate that no improvement is gained in intensity vs. confinement with back-action.

Looking at Eq. (2.10), in the strong back-action regime, one of the factors of $\frac{1}{\delta x}$ originates simply from the time $T \propto \delta x$ that the particle takes to travel between the walls of the square well. This part of the scaling seems fundamental and cannot be improved within this model. On the other hand, the second factor of $\frac{1}{k\delta x}$ clearly originates from the vanishing of back-action effects around the maximum of the mode profile, as the frequency shift becomes insensitive to first-order changes in the particle displacement, $f'(x_0) = 0$. We show that this factor is not fundamental, and can be eliminated by properly driving a second optical mode of the system.

2.5 TWO MODE BACK-ACTION

In this Sec. we show how the scaling between experienced intensity and confinement can be improved to $\langle I_{\mathrm{exp}} \rangle_t \propto \frac{1}{k\delta x}$ by using two different cavity modes for trapping. In order to obtain concrete results, we consider the simple geometry where the two modes consist of the first and second harmonics of a Fabry-Perot (see Fig. 2.4), although we believe that the conclusions hold quite generally. We assume that each mode can be driven with its own laser, with amplitude E_{0i} and frequency ω_{Li}. As the equation for the intra-cavity fields β_i (generalized from Eq. (2.5)) of each mode are decoupled from one another, they can be separately integrated as in the single-mode case. Thus, the total potential $U_{\mathrm{tot}}(x) = \sum_{i=1,2} U_i(x)$ is the incoherent sum of the potentials in Eq. (2.8) for each mode. To understand the relevant physics, it is sufficient to assume that the mode

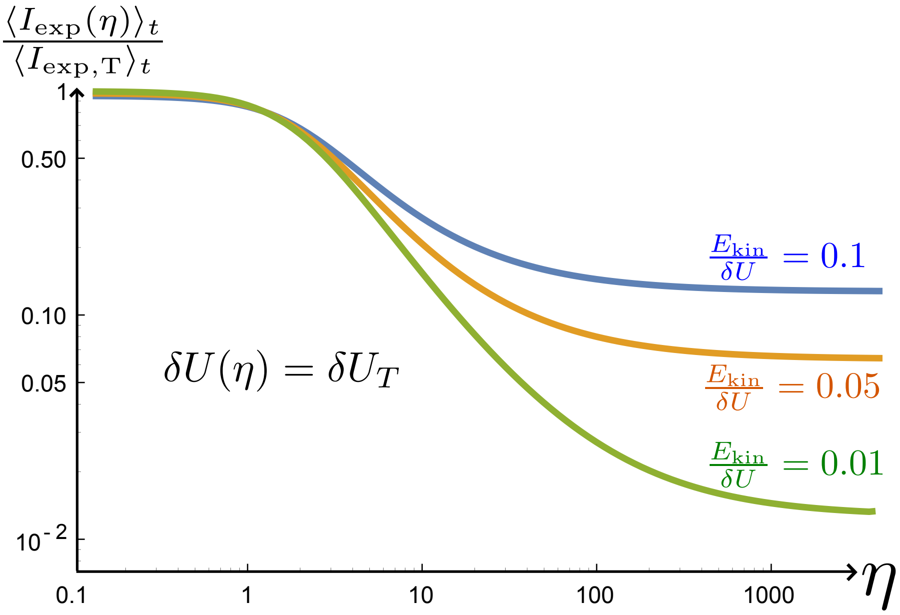

Figure 2.3: **Time-averaged experienced intensity of a trapped particle.** We plot the time-averaged experienced intensity as a function of back-action parameter $\langle I_{\mathrm{exp}}(\eta)\rangle_t$, normalized with the value in the optical tweezer regime $\eta \ll 1$. The two cases are set to have equal trap depth. The plot is numerically calculated for the case of trapping in the fundamental mode of a Fabry-Perot cavity $f(x) = \cos^2(kx)$ with resonant positions $kx_r = \pi/4$. The back-action regime can enable much lower average local intensities than in the optical tweezer regime.

driving amplitudes E_{0i}, decay rates κ_{ex}, κ_{in}, and back-action parameters are identical, although the concepts can be easily generalized.

The interesting regime will be when the resonant positions of each mode are tuned by their respective driving laser frequencies such that each mode is responsible for providing one trapping wall. This is illustrated in Fig. 2.4b), where the left and right walls x_{r1} and x_{r2} originate from the first and second cavity modes, respectively. Significantly, the well can be located far from the nodes/antinodes $f_i'(x) = 0$ where the effects of back-action would vanish for either mode. In the following we will distinguish three different regimes concerning the ratio between the distance $d = |x_{r1} - x_{r2}|$ and the width $\sim \frac{2}{k\eta}$ of these intensity peaks illustrated in Fig. 2.4.

We start by examining the high back-action regime, when the distance of the intensity peaks is much larger than their width, $kd = k|x_{r1} - x_{r2}| \gg \frac{2}{\eta}$, such that we encounter an almost perfect square-well potential as shown in Fig. 2.4b) and Fig. 2.5. It is straightforward to generalize the high back-action limit of Eq. (2.10) in the single mode case. As the particle is trapped far from points where back-action effects vanish ($f_i'(x) = 0$), we recover the improved scaling between experienced intensity and confinement, $\langle I_{exp}\rangle_t \propto \frac{1}{k\delta x}$ as already anticipated.

Qualitatively, the conditions needed to reach this scaling are that $kd \gg \frac{2}{\eta}$, so that the potential resembles a square well, but also that the ratio of kinetic energy to potential depth is sufficiently large that the particle actually approaches the edges of the well. This is schematically illustrated in Fig. 2.5. Assuming that the latter condition is initially satisfied for a large value of d (subplot 1), it continues to be satisfied by decreasing d (subplot 2). On the other hand, it can be seen that dramatically increasing the trap depth prevents the particle from reaching the edge (subplot 3), which results in a less favorable scaling of intensity versus confinement. In Fig. 2.5, we have plotted the results of experienced intensity vs. confinement from full numerical simulations of equations (2.3)-(2.5) (generalized to two modes). The different points for a fixed back-action parameter η are obtained by variation of the input powers and resonant positions x_r (via the laser frequencies). Tuning the resonant positions to reduce $d = |x_{r1} - x_{r2}|$ indeed enables one to saturate the scaling of $\langle I_{exp}\rangle_t \propto \frac{1}{k\delta x}$ as long as $k\delta x \gtrsim \frac{2}{\eta}$, as illustrated in Fig. 2.6a).

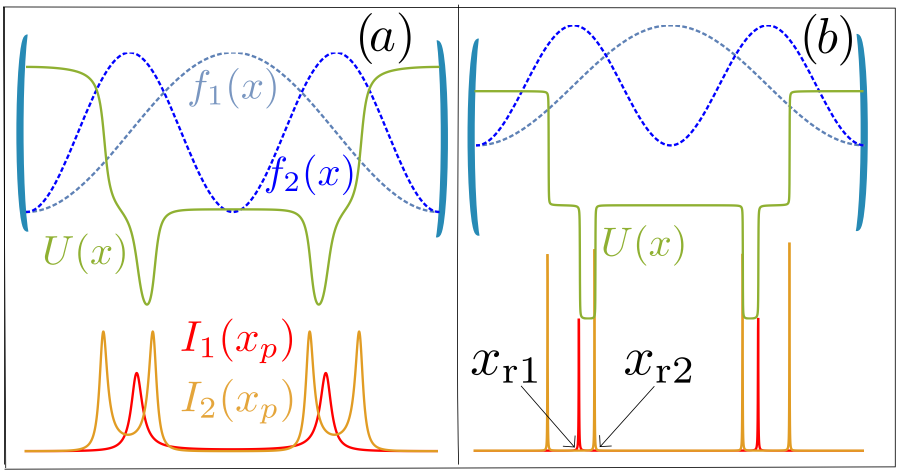

Figure 2.4: **SIBA with two optical modes**, illustrated here for the first two modes of a Fabry-Perot cavity. Top: the mode profiles are given by $f_1(x) = \cos^2(kx)$, $f_2(x) = \sin^2(2kx)$. Green: the resulting optical trapping potential $U(x)$. Bottom: intra-cavity intensities $I(x)$ as a function of particle position. a) In the harmonic back-action regime, the distance between the resonant points is comparable to the width of the intensity peaks, $kd \sim \frac{2}{\eta}$. b) In the high back-action regime, the distance significantly exceeds the width, $kd \gg \frac{2}{\eta}$.

For $k\delta x \lesssim \frac{2}{\eta}$, the optimal scaling seen in the numerics goes like $\langle I_{\mathrm{exp,hb}}\rangle_t \propto \frac{1}{\eta(k\delta x)^2}$. The scaling with δx^{-2} resembles the optical tweezer case, but the intensity is suppressed by a factor of η. We call this the "harmonic back-action regime" (see Fig. 2.4a)). To understand this case, we first note that the particle moves by a small enough amount around the trap minimum that the forces from each mode can be linearized around small displacements to yield a harmonic trap. Furthermore, for small displacements, the total time averaged experienced intensity $\langle I_{\mathrm{exp}}\rangle_t = \sum_i \langle I_{\mathrm{exp},i}\rangle_t \approx \sum_i I_i(x_0)$ is just the sum of the intensities of the respective mode at the trap minimum $x_p = x_0$. The associated spring constant is:

$$k_{\mathrm{opt}} = -F'(x_0) = \sum_i n_i'(x_0)\omega_{c,i}'(x_0) + n_i(x_0)\omega_{c,i}''(x_0) \quad (2.11)$$

where the sum goes over all trapping modes. The first term $n_i'(x_0)$ is a new contribution to the optical spring constant k_{opt} originating from the change in photon number with particle position around the trap minimum. Intuitively, this back-action contribution to the spring constant is maximized by ensuring the photon number of each mode maximally changes around x_0. This is roughly optimized by setting $kd \sim \frac{2}{\eta}$, such that x_0 corresponds to sitting half a cavity linewidth away from the resonant position x_r. Such an optimization yields (see Appendix A.4):

$$k_{\mathrm{opt},i} = \frac{\alpha(\omega)}{c\epsilon_0} \langle I_{\mathrm{exp},i} \rangle_t \frac{1}{f_i(x_0)} \left[\eta_i f_i'(x_{ri})^2 - f_i''(x_0) \right]. \tag{2.12}$$

The first term in the brackets originates from the change in photon number with particle position, whereas the second term reduces to the optical tweezer spring constant given by Eq. (2.1): $k_T = U''(x_0)$. Since $f''(x_0) \sim f'(x_0)^2 \sim k^2$, it can be seen that the back-action contribution is a factor of η larger. We can equivalently interpret this contribution as arising from an effective reduced wavelength $\lambda_{\mathrm{eff}} \sim \frac{\lambda}{\sqrt{\eta}}$, which enables the generation of trap features far below the diffraction limit. We emphasize that this effect originates from the rapid change in intra-cavity photon number with particle displacement rather than a change in the spatial mode itself (see Eq. (2.11)), and thus there is no breakdown of the dipole approximation in which all of these expressions are derived. This is analogous to the “optical spring" effect described in Sec. 1.2.3 and Fig. 1.4, where an optical cavity can exert large restoring forces for small displacements of a mechanical system. In the conventional optical spring effect the stiffness of the mechanical mode itself plays the role of our second optical mode, and serves to keep the equilibrium position at a point of non-vanishing back-action ($f'(x_0) \neq 0$) [78, 79].

Exploiting the notion of a reduced wavelength, in the harmonic back-action regime one can immediately conclude that the scaling for average experienced intensity improves from $\langle I_{\mathrm{exp},T} \rangle_t \propto \frac{1}{(k\delta x)^2}$ for an optical tweezer to $\langle I_{\mathrm{exp,hb}} \rangle_t \propto \frac{1}{\eta (k\delta x)^2}$. A more detailed optimization of the system shown in Fig. 2.4 reveals that (see Appendix A.4):

$$\frac{\langle I_{\mathrm{exp,hb}} \rangle_t}{\langle I_{\mathrm{exp,T}} \rangle_t} = \frac{4}{\eta} \tag{2.13}$$

for equal confinement and kinetic energy. We want to emphasize that to reach this optimal scaling, one should fix $kd = k|x_{r1} - x_{r2}| \sim \frac{2}{\eta}$. In other words, to achieve the best confinement for a given intensity, one should increase the laser intensity (see Fig. 2.5, subplot 4 and 5). This procedure enables one to stay along the dotted line of the intensity versus confinement plot illustrated in Fig. 2.6. In contrast, Fig. 2.6 also shows that by decreasing the distance between the resonant positions, $kd \ll \frac{2}{\eta}$, the scaling deviates back towards the optical tweezer limit and the benefits of back-action vanish.

2.6 CONCLUSION

There have already been two types of systems, plasmonic cavities [80] and photonic crystal cavities [76], where SIBA has been observed, and we now discuss the potential figures of merit associated with each. As the plasmon resonances associated with small metallic systems do not obey a diffraction limit, they are able to achieve strongly sub-wavelength mode volumes. On the other hand, realistic quality factors are limited to $Q \lesssim 10 - 10^2$. At the same time, an upper bound on the validity of our calculation is that the particle size $V \lesssim V_m$ does not exceed the mode volume, and thus we anticipate maximum possible values of $\eta \sim 10 - 10^2$ for such systems. In photonic crystal cavities, the mode volume is limited by the diffraction limit to $V_m \gtrsim (\frac{\lambda}{2})^3$, while extremely high quality factors of $Q \sim 10^6$ are possible [76]. This yields $\eta \sim 10, 100, 400$ for a dielectric sphere with radius $r \sim$ 6.5nm,15nm, 28nm (Appendix A.2). There has been significant activity in recent years to develop design principles in order to tailor the spatial modes of plasmonic [80] and photonic crystal structures [81] for trapping. Combined with the potentially large back-action parameters achievable, we anticipate that our work will open up significant new opportunities for optical trapping. It would also be interesting to explore the use of large back-action parameters in other functionalities, such as particle detection and feedback cooling.

Finally, it is intriguing to ask whether back-action trapping, and the resulting square wells, could be applicable to atoms. Combined with the long coherence times of the atom, a square well could potentially be used to generate a "two-level" phonon. This would build upon the already rich field of mechanical effects of light on atoms in cavities [82–86] and recent successful efforts to interface cold atoms with nanophotonic systems [87, 88]. We thus turn to this question in the next chapter.

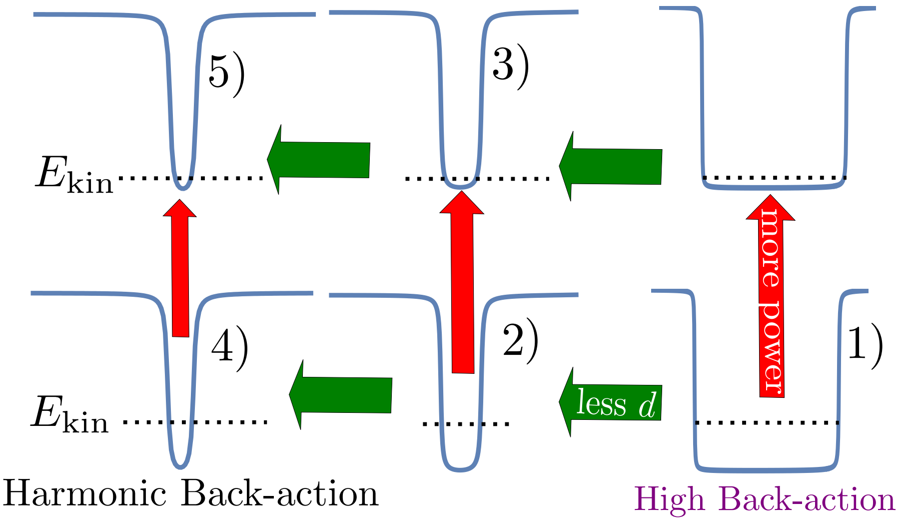

Figure 2.5: **Potential with two optical modes.** Here we show how the trapping potential transforms as one either decreases the distance $d = |x_{r1} - x_{r2}|$ between the resonant positions (via changes in the laser detuning), or increases the laser intensity. Transformations via changes in d and intensity are depicted by the green and red arrows, respectively. For a given kinetic energy E_{kin} increasing the laser power lowers the ratio between kinetic energy and trap depth. This ratio then determines the region of the potential the particle is allowed to explore. In potential 1) we are in the high back-action regime ($kd = k|x_{r2} - x_{r1}| \gg \frac{2}{\eta}$) where d and δU (laser power) decouple and the potential forms a square well that the particle has sufficient energy to explore. Decreasing d until the condition $kd \sim \frac{2}{\eta}$ is reached enables one to stay in the high back-action regime, as shown in 2). On the other hand, a significant increase in power, illustrated in 3), prevents the particle from coming into contact with the edges of the well, and one loses the favorable scaling of intensity versus confinement. At $kd \sim \frac{2}{\eta}$, one reaches the harmonic back-action regime, where the particle experiences an approximate harmonic potential regardless of laser power. Optimum intensity versus confinement is achieved by then increasing laser power, as opposed to further reduction in d, as illustrated in 4) and 5). The subplot numbers 1), 2), 3), 4), 5) correspond to the same numbers as indicated in Fig. 2.6b).

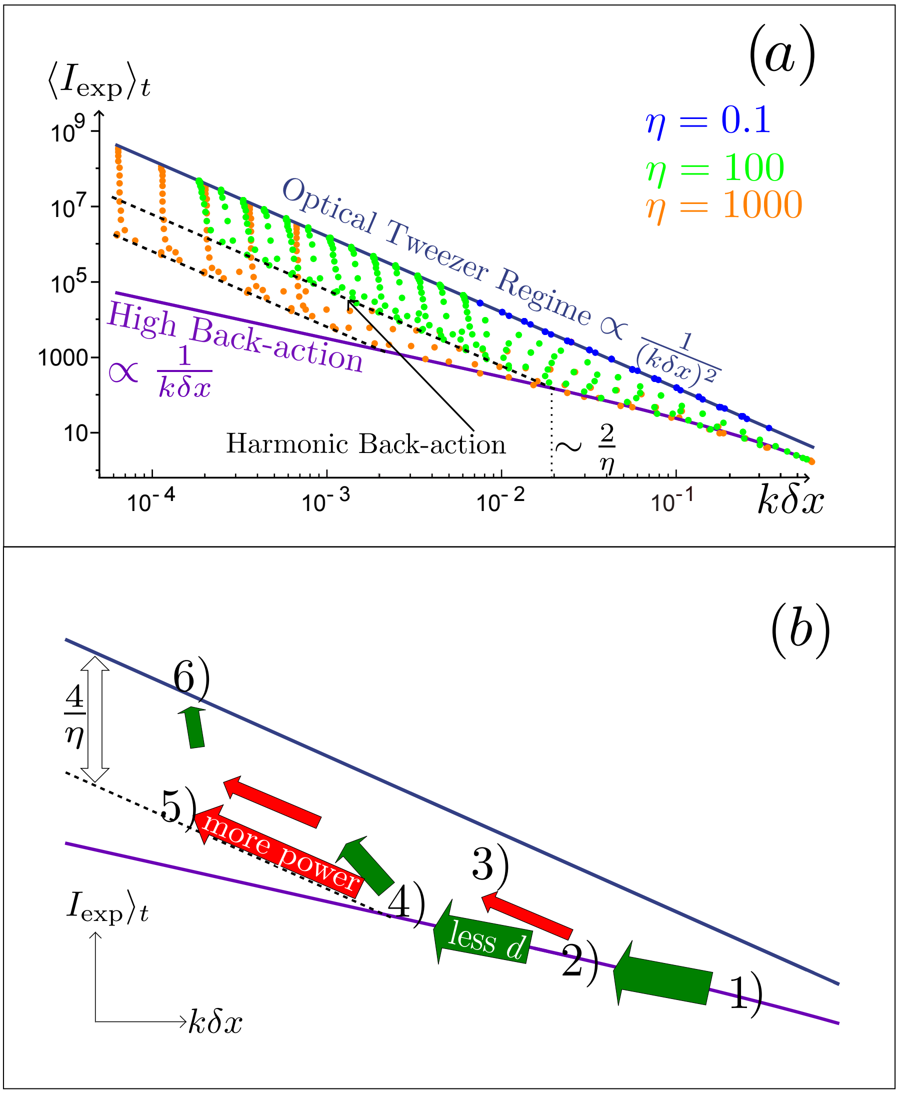

Figure 2.6: **Time-averaged experienced intensity vs. confinement for two optical modes.** a) Time-averaged experienced intensity in units of $\frac{cE_{\text{kin}}}{\alpha(\omega)}$ as a function of confinement $k\delta x = k|x_{t2} - x_{t1}|$. The individual points originate from different combinations of back-action parameter, laser power and detunings. The solid lines indicate the scalings in the optical tweezer regime and high back-action regime ($kd = k|x_{r2} - x_{r1}| \gg \frac{2}{\eta}$). The dashed line shows the optimized harmonic back-action regime, where $kd \sim \frac{2}{\eta}$. b) Illustration of figure 2.6a) for a fixed η and E_{kin}, and a schematic of the protocol to saturate the scaling bounds. The green arrows denote a decrease in distance between the resonant positions $d = |x_{r1} - x_{r2}|$, while the red arrows denote an increase in laser power. The numbers 1), 2), 3), 4), 5) correspond to the same numbers as indicated in Fig. 2.5. 6) decreasing $kd < \frac{2}{\eta}$ suppresses back-action as the particle motion no longer shifts the cavity mode frequencies.

3

EXPLORING UNRESOLVED SIDEBAND, OPTOMECHANICAL STRONG COUPLING USING A SINGLE ATOM COUPLED TO A CAVITY

3.1 INTRODUCTION

In optomechanics much progress has been made improving the control over the interaction between photons and phonons at the quantum level [89]. Lately there have been many important experimental successes, which include the generation of slow light with optomechanics [90], the entanglement of motion with microwave fields [91], and very recently remote entanglement between two micromechanical oscillators [92]. For most of the quantum phenomena observed thus far or envisioned, sideband resolution, where the mechanical frequency ω_m exceeds the cavity linewidth κ, is required. For example, this enables cooling to the quantum ground state [93, 94], which represents a fiducial pure state preparation. In one remarkable theoretical work [46], it has been predicted that the combination of sideband resolution and single-photon optomechanical strong coupling – where the zero-point motional uncertainty induces a shift in the optical resonance frequency larger than the cavity linewidth – would enable the generation of non-classical, antibunched light.

Here, we study the complementary regime of single-photon optomechanical strong coupling, but with unresolved sidebands [95, 96]. We show that interesting quantum effects both in the light and motion can be observed, at least when the mechanical system is well-isolated and can be separately prepared in the ground state. A natural candidate system consists of a single atom [50–53, 97, 98] or ion [54–59] in cavity QED, whose electronic transition is strongly coupled to a near-resonant optical mode. To provide an intuitive picture, strong coupling within cavity QED [99, 100] implies that a point-like atom produces a shift in the cavity resonance frequency that is larger than the cavity linewidth, when the atom is situated at a cavity antinode. If the atom is displaced by a quarter wavelength to a node, this shift vanishes. Given the light mass, it is straightforward for a trapped atom to have a zero-point motion on that scale, thus realizing single-photon optomechanical strong coupling. Furthermore, realistic trap frequencies for atoms are quite low ($\lesssim$ MHz), and are naturally exceeded by the cavity linewidth for small cavities [52, 53, 101, 102]. In this regime of optomechanical strong coupling and unresolved sidebands, the interesting physics arises because the resonance frequency of the cavity correlates strongly with the atomic position, and as the reflection or transmission of a single photon depends on the resonance frequency, a strong entanglement between photon and motion ensues, which is visible in both of these degrees of freedom.

In this work we begin by considering a single atom externally trapped inside a cavity mode that is driven with a coherent state. When the cavity frequency is detuned from the atomic resonance, we derive from the full Jaynes-Cummings model of cavity QED an effective optomechanical Hamiltonian, which only depends on the atomic motion and cavity degrees of freedom. We proceed by tracing out the cavity degree of freedom and analytically derive an effective quantum master equation describing the motional dynamics of the atom only. This master equation would allow for the calculation of motional energy eigenvalues and their lifetimes, and yields interesting insights in the heating processes associated with entanglement between light and motion. This entanglement is also directly revealed by applying scattering theory to exactly solve for the joint atom-photon wave function following the scattering of a single incident photon. Using this formalism, we show that the properties of the scattered photon can become entangled with the atomic motion on length scales much smaller than either the resonant wavelength or the atomic zero-point motion. As one consequence, once the photon is traced out, the atomic motion is seen to heat up significantly, even if the atom is tightly trapped within the Lamb-Dicke limit. We also show that this entanglement can manifest itself in the second-order correlation functions of the outgoing field given a weak coherent state input, or be used to produce a heralded single-phonon Fock state of the atomic motion.

3.2 CAVITY QED: JAYNES CUMMINGS MODEL

Before we study the dynamics of atomic motion inside an optical cavity, we first motivate the field of cavity QED without including motion. The two-level nature of the internal degrees of freedom of single atoms makes them ultimate nonlinear optical elements, fundamentally only able to absorb and emit single photons at a time. As single photons are already non-classical states of light, atoms are a natural platform to potentially realize protocols for quantum information processing. However, in order to efficiently harvest this nonlinearity with light one needs to ensure a strong interaction between the atom and incident photons, which is unfortunately extremely difficult in free space. For example, the interaction probability for a photon, which is resonant with an atomic transition is $P \approx \sigma/A$, where $\sigma \sim \lambda^2$ is the atomic optical cross section and A is the light beam area. To maximize the interaction probability the light has to be focused close to the diffraction limit $A \sim \lambda^2$. This is not easy and maximally achieved values are $P \sim 0.05$ for the interaction between neutral atoms and focused laser beams [103, 104]. One popular solution to this problem is to make the same photon interact with a single atom multiple times by placing the atom inside a cavity, where the interaction probability is enhanced by the number of photon bounces motivating the field of cavity QED. The interaction between the atomic internal degrees of freedom and the cavity mode is described by the Jaynes-Cummings (J-C) interaction Hamiltonian [105]:

$$H_{IJ} = g_0(a^\dagger \sigma_{ge} + a\sigma_{eg}), \tag{3.1}$$

which models the transfer of excitations with rate g_0 (the so-called "vacuum Rabi splitting") between the cavity mode described by photon annihilation operator a and the atomic internal degrees of freedom described by the Pauli matrices $\sigma_{ge} = |g\rangle\langle e|$ and $\sigma_{eg} = |e\rangle\langle g|$. Here, $|g\rangle$ and $|e\rangle$ denote the atomic ground and excited states, respectively. Due to this interaction and the nonlinear properties of the atom, the energy eigenvalues of the composite cavity-atom system are nonlinear as well and constitute the famous Jaynes-Cummings Ladder, as illustrated in Fig. 3.1 for a system where the atomic resonance $\omega_0 = \omega_c$ matches the resonance frequency of the cavity. The eigenstates of the system $|n, \pm\rangle = 1/\sqrt{2}(|n, e\rangle \pm |n+1, g\rangle)$ are symmetric and anti-symmetric superpositions of n photons in the cavity mode while the atom is excited, and $n+1$ photons in the cavity mode while the atom is in its ground state. They have corresponding nonlinear energy eigenvalues of $E_{n,\pm} = n\omega_0 \pm \sqrt{n} g_0$. In this way, the nonlinearity of the atom converts into a nonlinearity of the macroscopic cavity-atom system, which as a whole enables a higher interaction efficiency compared to a single atom in free space. The strong coupling regime of cavity QED consists of the coherent coupling strength g_0 exceeding both the cavity linewidth κ and the atomic spontaneous emission rate γ.

3.3 CAVITY QED WITH MOTION

In this section, we introduce the Jaynes-Cummings (J-C) model [105] to describe the interaction of a (moving) two-level atom

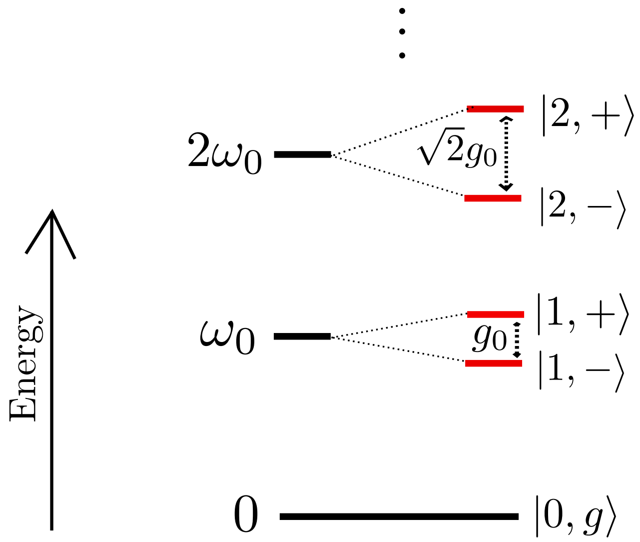

Figure 3.1: **Jaynes Cummings Ladder.** The energy eigenvalue spectrum of an atom which is resonantly coupled to a cavity is nonlinear since $E_{n,\pm} = n\omega_0 \pm \sqrt{n}g_0$. The corresponding eigenstates are $|n,\pm\rangle = 1/\sqrt{2}(|n,e\rangle \pm |n+1,g\rangle)$, where $n/n+1$ denotes the number of photons in the cavity mode, and e/g refers to the atomic excited/ground state, respectively.

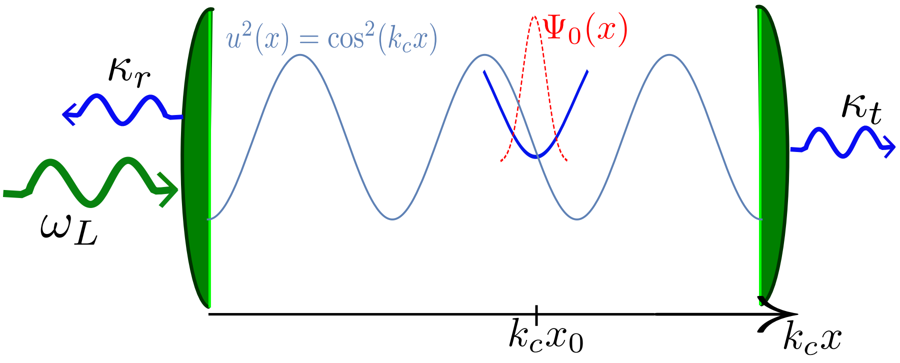

Figure 3.2: An atom is trapped externally by a potential (blue) with equilibrium position x_0 inside a cavity with intensity mode profile $u^2(x)$. $\Psi_0(x)$ is the initial wave function of the atomic motion. Incident photons with frequency ω_L arrive from the left. The left mirror has a decay rate of κ_r and the right mirror has a decay rate of κ_t.

with photons in a cavity mode with amplitude $u(x) = \cos(k_c x)$, where k_c is the wavevector of the cavity mode as shown in Fig. 3.2. In the case where the atomic frequency ω_0 is far detuned from the bare cavity resonance ω_c, we eliminate the atomic internal degrees of freedom, to arrive at an effective optomechanical interaction between the atomic motion and cavity. We further proceed to derive an effective master equation describing the atomic motion when the cavity is externally driven by a coherent state with photon number flux E_0^2 and frequency ω_L. We note that such a procedure would give rise to, e.g., the usual optical cooling and heating rates in a conventional optomechanical system [93, 94, 106]. In our case, however, we neither linearize the cavity field around a steady-state solution nor the motion, owing to the potentially large coupling between motion and the cavity field, which leads to much richer effects.

The full quantum master equation associated with the J-C model, in an interaction picture rotating with the laser frequency ω_L, is given by

$$\dot{\rho} = -i\left[H_{JC}, \rho\right] + (L_\gamma + L_\kappa)\rho \equiv L\rho. \tag{3.2}$$

The J-C Hamiltonian including motion is given by

$$\begin{aligned} H_{JC} = & \omega_m b^\dagger b - \delta_0 \sigma_{ee} - \delta_c a^\dagger a + \sqrt{\kappa_r} E_0 (a + a^\dagger) \\ & + g_0 u(x)(a^\dagger \sigma_{ge} + h.c.). \end{aligned} \tag{3.3}$$

It is written in terms of the detuning between laser and atom-/cavity $\delta_{0/c} = \omega_L - \omega_{0/c}$, respectively, and the mechanical frequency ω_m of the external trap. Furthermore, a and b denote the photon and phonon annihilation operators, respectively, while $\sigma_{\alpha\beta} = |\alpha\rangle\langle\beta|$, where $\alpha, \beta = g, e$ correspond to combinations of the atomic ground and excited states. κ_r denotes the decay rate of the left cavity mirror (reflection), which also serves as the source of injection of photons. The right mirror has a decay rate of κ_t (transmission). In addition to the external coupling, the cavity has an intrinsic loss rate κ_{in}, such as through material absorption and scattering losses. The total cavity linewidth is thus $\kappa = \kappa_r + \kappa_t + \kappa_{in}$. The last term of H_{JC} describes the coupling between cavity and atom with the coupling strength $g_0 u(x)$ depending on the atomic position $x = x_{zp}(b + b^\dagger)$, which can be written in terms of the zero-point motion $x_{zp} = \sqrt{\hbar/(2m\omega_m)}$ (m being the atomic mass), and where g_0 is the magnitude of the vacuum Rabi splitting at the anti-node of the cavity. The Lindblad L_c operator describing cavity dissipation is given by:

$$L_\kappa \rho = -\frac{\kappa}{2}\left(a^\dagger a \rho + \rho a^\dagger a - 2a\rho a^\dagger\right) \tag{3.4}$$

and the general Lindblad operator L_{γ}^{3D} for spontaneous emission into three dimensions of the atom at a rate γ reads [82]:

$$L_{\gamma}^{3D}\rho = -\frac{\gamma}{2}\left(\sigma_{ee}\rho + \rho\sigma_{ee} - 2\int d\Omega_{\vec{u}} N_f(\vec{u})\sigma_{ge} e^{-ik_c\vec{u}\cdot\vec{r}}\rho e^{ik_c\vec{u}\cdot\vec{r}}\sigma_{eg}\right). \tag{3.5}$$

This process, additionally to the emission of a photon, causes a recoil of $k = \frac{\omega_0}{c} \approx k_c$ opposite to the direction $\vec{u}$ of the emitted photon, which is integrated over solid angle $(d\Omega_{\vec{u}})$ and weighted by the distribution function $N_f(\vec{u})$ corresponding to the dipole emission pattern. However, to provide a simpler model that qualitatively captures the correct behavior, we will just consider one single direction of spontaneous emission along the positive cavity axis (x). With a single spontaneous emission direction we can write

$$L_{\gamma}\rho = -\frac{\gamma}{2}\left(\sigma_{ee}\rho + \rho\sigma_{ee} - 2\sigma_{ge}e^{-ik_c x}\rho e^{ik_c x}\sigma_{eg}\right). \tag{3.6}$$

Now we consider the dispersive regime $\Delta = \omega_0 - \omega_c \gg g_0, \kappa, \gamma$, where the atom-cavity detuning is large. Thus the single-excitation eigenstates of the J-C Hamiltonian are either mostly atomic $(|\psi_+\rangle \approx |e, 0\rangle)$ or photonic $(|\psi_-\rangle \approx |g, 1\rangle)$, where 0,1 denote the intra-cavity photon Fock state number. These eigenstates have corresponding eigenenergies $E_1^+ \approx \omega_0 + \frac{g_0^2}{\Delta}u^2(x)$ and $E_1^- \approx \omega_c - \frac{g_0^2}{\Delta}u^2(x)$, respectively. Here, we focus on the case when the system is driven near resonantly with the photonic eigenstate. In that limit, the atom can approximately be viewed as a classical dielectric that provides a position-dependent cavity shift with an effective optomechanical coupling strength $\propto \frac{g_0^2}{\Delta}$. We will derive this effective optomechanical model now in more detail.

3.3.1 *Effective Optomechanical Model*

For large laser-atom detunings $\delta_0 \gg g_0$, the atomic ground state population is approximately one, which allows for an effective elimination of the atomic excited state [82, 107] using the Nakajima-Zwanzig projection operator formalism [106, 108, 109] (details in Appendix A.5.1). The resulting effective master equation is given by

$$\dot{\rho} = -i\left[H_{om}, \rho\right] + L_{om}\rho, \tag{3.7}$$

with an effective optomechanical Hamiltonian

$$H_{om} = \omega_m b^{\dagger}b - \Delta_c(x)a^{\dagger}a + \sqrt{\kappa_r}E_0(a + a^{\dagger}). \tag{3.8}$$

The position dependent cavity-laser detuning is given by

$$\Delta_c(x) = \delta_c - \frac{g_0^2 \delta_0}{\delta_0^2 + \frac{\gamma^2}{4}} u^2(x), \tag{3.9}$$

which now accounts for the cavity shift arising from off-resonant coupling to the atomic transition. The system losses are given by the effective Liouvillian

$$\begin{aligned} L_{\mathrm{om}}\rho = &-\frac{\kappa}{2}\left(a^\dagger a\rho + \rho a^\dagger a - 2a\rho a^\dagger\right) \\ &- \frac{\gamma}{2}\frac{g_0^2}{\delta_0^2 + \frac{\gamma^2}{4}}\left(u^2(x)a^\dagger a\rho + \rho a^\dagger a u^2(x) - 2au(x)e^{-ik_c x}\rho e^{ik_c x}u(x)a^\dagger\right), \end{aligned} \tag{3.10}$$

which describes the broadening of the cavity linewidth due to atomic spontaneous emission,

$$\kappa(x) = \kappa + \gamma \frac{g_0^2}{\delta_0^2 + \frac{\gamma^2}{4}} u^2(x). \tag{3.11}$$

Aside from Appendix A.7, where we discuss in greater detail the corrections to and limitations of the effective model, we will work in regimes where the atomic contribution is negligible compared to the (large) bare cavity linewidth.

In typical treatments of optomechanical systems, the position-dependent shift in Eq. (3.9) would only be treated to linear order in the displacement, with the justification that the maximum possible displacement is very small. However, for atoms, the zero-point motion can be comparable to the optical wavelength (the scale over which $u(x)$ varies), a ratio that can be characterized by the Lamb-Dicke parameter $\eta_{\mathrm{LD}} \equiv k_c x_{zp} = \sqrt{\omega_{\mathrm{rec}}/\omega_m}$. For example, taking a recoil frequency $\omega_{\mathrm{rec}} == \hbar k_c^2/(2m) = 2\pi \times 6.8\,\mathrm{kHz}$, which relates the resonant wavevector k_c and atomic mass m of a $^{40}\mathrm{Ca}^+$-ion, and a trap frequency of $\omega_m = 2\pi \times 0.1\,\mathrm{MHz}$ results in $\eta_{\mathrm{LD}} = \sqrt{\omega_{\mathrm{rec}}/\omega_m} \approx 0.26$. For $\eta_{\mathrm{LD}} \sim 1$, the atomic wavepacket would have significant weight both in a cavity anti-node and node, with an associated cavity frequency shift of

$$g_{\mathrm{om}} = -\frac{g_0^2 \delta_0}{\delta_0^2 + \frac{\gamma^2}{4}} \tag{3.12}$$

and zero, respectively. As our perturbative treatment is valid for $\delta_0 \gtrsim g_0$ (see Appendix A.7), one sees that strong optomechanical coupling $g_{\mathrm{om}} \gtrsim \kappa$ can be achieved if the strong coupling regime of conventional cavity QED ($g_0 > \kappa$) is realized. The standard optomechanical Hamiltonian (linearized in displacement) describing interactions between single photons and single phonons is given by $H_{\mathrm{oms}} = g_m(b^\dagger + b)a^\dagger a$, where $g_m = \Delta_c'(x_0)x_{zp} \sim g_{om}\eta_{LD}$. Thus, in order to achieve strong optomechanical coupling on the single-photon, single-phonon level ($g_m \gtrsim \kappa$), additionally a sufficiently large Lamb-Dicke parameter η_{LD} is required. Given the above considerations, we next derive an effective master equation for the atomic motion alone that is valid for strong and nonlinear optomechanical coupling, which can be viewed as a generalization of the typical optically-induced cooling and heating rates obtained for linearized optomechanical coupling [93, 94, 106]. Our master equation also complements previous work investigating intra-cavity optical forces on atoms in the semi-classical limit [82, 83, 110–112].

3.3.2 *Effective Master Equation for Motion*

Starting with Eq. (3.7) we can use the Nakajima-Zwanzig technique to effectively eliminate the cavity degrees of freedom (Appendix A.5.2). Here, for simplicity we assume that spontaneous emission can be ignored. The resulting master equation for atomic motion in conventional Lindblad-form is then given by:

$$\dot{\rho} = -i[H_m, \rho] - \frac{1}{2}\left(J^\dagger J\rho + \rho J^\dagger J\right) + J\rho J^\dagger. \tag{3.13}$$

The Hermitian Hamiltonian and jump operators are given respectively by

$$H_m = \omega_m b^\dagger b + \frac{\kappa_r E_0^2 \Delta_c(x)}{\Delta_c^2(x) + \frac{\kappa^2}{4}} \tag{3.14}$$

and

$$J = \frac{i\sqrt{\kappa\kappa_r}E_0}{\Delta_c(x) + i\frac{\kappa}{2}}. \tag{3.15}$$

We will provide an intuitive picture of this master equation in Sec. 3.5. Now we focus on the effective mechanical potential which arises in the Hamiltonian. We can always rewrite a master equation in terms of an effective non-Hermitian Hamiltonian H_c which then contains a complex potential:

$$\dot{\rho} = -i(H_c\rho - \rho H_c^\dagger) + J\rho J^\dagger \tag{3.16}$$

$$H_c = \omega_m b^\dagger b + V(x) \tag{3.17}$$

with

$$V(x) = \frac{\kappa_r E_0^2 \Delta_c(x)}{\Delta_c^2(x) + \frac{\kappa^2}{4}} - \frac{i}{2}J^\dagger J. \tag{3.18}$$

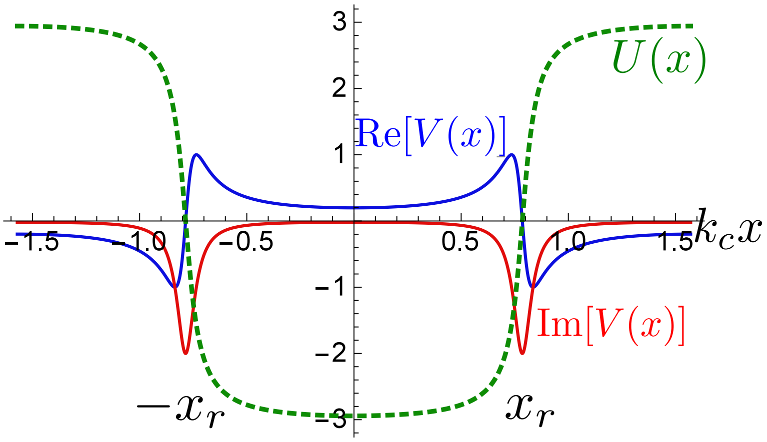

Figure 3.3: **Quantum and classical mechanical potential arising from a coherently driven cavity mode**
Real part $\mathrm{Re}[V(x)]$ (blue) and imaginary part $\mathrm{Im}[V(x)]$ (red) of the quantum potential Eq. (3.18) as a function of position. Also plotted is the classical potential $U(x)$ (dashed, green) derived by integrating the expectation value of the force acting on the atom. One can observe that the real part of the quantum potential is significantly different from the classical expectation value. Here, we choose a laser frequency ω_L such that the resonant position $k_c x_r = \pi/4$, and Jaynes-Cummings parameters of $g_0/\kappa \sim 20$ and $\delta_0 = -2g_0$ (yielding an effective optomechanical coupling strength of $g_{om} \sim 10\kappa$). The potentials are plotted in units of $\hbar(\kappa_r/\kappa)E_0^2$.

The real and imaginary parts of the complex potential $V(x)$ are illustrated in Fig. 3.3. As the resonance frequency of the cavity depends on the position of the atom, there can be atomic positions for which the cavity is resonant with the coherent drive. These positions x_r are called resonant positions and are defined by $\Delta_c(x_r) = 0$. Around these positions, the real part of the potential changes sign and the imaginary part has sinks indicating increased heating around those positions.

It is also interesting to compare the "coherent" potential, $\mathrm{Re}[V(x)]$, with the classical potential $U(x)$ as derived from the average force $F(x) = d\langle p\rangle/dt = \mathrm{Tr}(p\rho)$ on the atom, and defined via $dU/dx = -F(x)$. The result is given by

$$U(x) = -2\frac{\kappa_r}{\kappa}E_0^2 \arctan\left(\frac{2\Delta_c(x)}{\kappa}\right), \tag{3.19}$$

which agrees with our previous, completely classical analysis of a dielectric object trapped in a cavity in Chapter 2 (see Eq. (2.8)). The potential is illustrated in Fig. 3.3. For large g_{om}/κ, $U(x)$ is seen to approach a square well, with the walls of the well aligning with the resonant positions $\sim x_r$ where the large intracavity field results in a large classical restoring force. By comparing $V(x)$ and $U(x)$, it is clear that a significant contribution of the average force must arise from the stochastic process associated with the quantum jumps J. As one consequence, although it would be highly interesting to realize a square well for atoms (leading, e.g., to a highly anharmonic phonon spectrum), the direct quantization of $U(x)$ in this case is not meaningful.

3.4 SINGLE-PHOTON SCATTERING THEORY: OPTOMECHANICAL STRONG COUPLING WITH UNRESOLVED SIDEBANDS

A complementary physical picture of the optomechanical coupling between an atom and cavity can be gained by considering not a coherent external drive, but single incident photons. From Eq. (3.7), the effective non-Hermitian Hamiltonian associated with an undriven system is

$$H_{\text{eff}} = \omega_m b^\dagger b - (\Delta_c(x) + i\frac{\kappa}{2})a^\dagger a \tag{3.20}$$

where $\Delta_c(x) = \omega_L - \omega_c(x)$ is the position-dependent detuning between photon frequency ω_L and cavity frequency $\omega_c(x) = \omega_c - g_{om}u^2(x)$. To be specific, we will consider single photons incident through the left mirror (see Fig. 3.2), which has a decay rate back into the reflection channel of κ_r. The right mirror is coupled to the controlled transmission channel with κ_t. The total cavity linewidth is thus $\kappa = \kappa_r + \kappa_t$. For simplicity we ignore here an intrinsic loss rate, although it is straightforward to include later on.

A connection can be made between the eigenstates of H_{eff} and the properties of single-photon scattering via the S-matrix formalism. Formally, the S-matrix describes a coherent evolution mapping an input state ($t = -\infty$) to an output state ($t = +\infty$):

$$|\Psi_{\text{out}}(\omega_L)\rangle = S\,|\Psi_{\text{in}}(\omega_L)\rangle\,. \tag{3.21}$$

Here, we assume a single monochromatic photon with frequency ω_L incident on the left cavity mirror

$$|\Psi_{\text{in}}(\omega_L)\rangle = |(\omega_L)_{\text{left}}, 0\rangle\,, \tag{3.22}$$

whereas the optomechanical system initially is in its ground state represented by the second entry in the ket state. Generically the output state will consist of a superposition of n phonons in the mechanical state, which were excited by the incoming photon, and an outgoing photon of energy $\omega_L - n\omega_m$ in either the reflection port (r) or transmission port (t):

$$\begin{aligned} |\Psi_{\text{out}}(\omega_L)\rangle = &\sum_n S_{r,n}(\omega_L)\,|(\omega_L - n\omega_m)_r, n\rangle \\ &+ \sum_n S_{t,n}(\omega_L)\,|(\omega_L - n\omega_m)_t, n\rangle\,. \end{aligned} \tag{3.23}$$

Due to a connection between the scattering matrix and the Heisenberg input-output operators [113] one can express the S-matrix elements in terms of the eigenvalues λ_β and eigenstates $|\beta\rangle$ of the effective Hamiltonian H_{eff} [114]. We provide a detailed derivation of the S-matrix elements in Appendix A.6. In reflection, the output consists of a superposition between a non-interacting propagating photon ($\delta_{n,0}$) and photon emission from the excited optomechanical system:

$$S_{r,n}(\omega_L) = \delta_{n,0} + i\kappa_r \sum_\beta \langle 1_c, n|\beta\rangle \frac{1}{\lambda_\beta} \langle \beta|1_c, 0\rangle. \tag{3.24}$$

Here, $\langle 1_c, n|\beta\rangle$ is the projection of the eigenstates $|\beta\rangle$ onto the basis states $\langle 1_c, n|$ with 1_c referring to a single photon inside the cavity mode. Similarly, the matrix elements for photon transmission are given by

$$S_{t,n}(\omega_L) = i\sqrt{\kappa_t\kappa_r} \sum_\beta \langle 1_c, n|\beta\rangle \frac{1}{\lambda_\beta} \langle \beta|1_c, 0\rangle. \tag{3.25}$$

The matrix element for photon transmission lacks the contribution from the non-interacting propagating photon as the input channel on the transmitting side of the cavity is in the vacuum state. To proceed further, we assume in the following that a detector cannot effectively resolve the frequency of the outgoing photon. Then, we can effectively write the outgoing state as

$$|\Psi_{\text{out}}(\omega_L)\rangle = S_r(\omega_L, x)\Psi_0(x)\,|1_r\rangle + S_t(\omega_L, x)\Psi_0(x)\,|1_t\rangle\,, \tag{3.26}$$

where $|1_{r/t}\rangle$ indicates an outgoing reflected/transmitted photon, respectively, and $\Psi_0(x)$ is the initial motional wave function of the atom. The entanglement between the photon frequency and the motional state has been suppressed, as we have assumed that any projective measurement of a photon in either port is not frequency-resolving. Furthermore, we now assume that we operate in the sideband-unresolved limit $\kappa \gg \omega_m$. The Hamiltonian H_{eff} is approximately diagonal in the position basis, as the optomechanical interaction dominates over the free Hamilontian $\omega_m b^\dagger b$ in H_{eff} (Eq. 3.20). Thus, the eigenvalues of H_{eff} are approximately $\lambda \approx -\Delta_c(x) - i\frac{\kappa}{2}$ and the scattering matrix elements can be simply written as

$$S_r(\omega_L, x) = 1 - \frac{i\kappa_r}{\Delta_c(x) + i\frac{\kappa}{2}} \tag{3.27}$$

and

$$S_t(\omega_L, x) = -\frac{i\sqrt{\kappa_t\kappa_r}}{\Delta_c(x) + i\frac{\kappa}{2}}. \tag{3.28}$$

As the shape of the mechanical wave function after the decay of a single photon into one specific channel is the product between the corresponding S-matrix element and the initial wave function $\Psi_0(x)$, we observe that the shape of the mechanical wave function after one such scattering event is strongly entangled with whether the decaying photon is reflected or transmitted.

3.5 CONNECTION BETWEEN SCATTERING THEORY AND MASTER EQUATION

Motivated by the observation that the scattering matrices S_t and S_r of Eqs. (3.27) and (3.28) are very similar to the jump operators J (Eq. 3.15), we express the master equation (3.13) in a way that its jump operators correspond to the single photon scattering matrices:

$$\dot{\rho} = -i(H_s\rho - \rho H_s^\dagger) + E_0^2(S_r\rho S_r^\dagger + S_t\rho S_t^\dagger) \tag{3.29}$$

with the Hamiltonian

$$H_s = \omega_m b^\dagger b - \frac{i}{2}E_0^2. \tag{3.30}$$

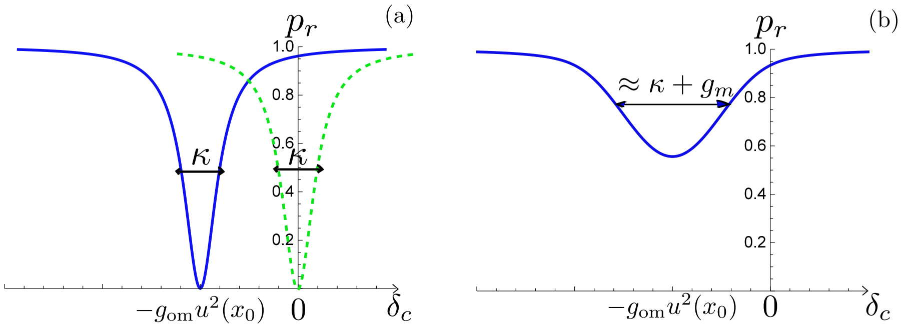

Figure 3.4: **Reflection spectrum p_r as a function of laser frequency ω_L.** Here, we take critical coupling ($\kappa_r = \kappa/2$) and a trap equilibrium position of $k_c x_0 = \pi/4$. We assume the initial atomic wave function is in the motional ground state.
a) If the zero-point motion is unresolved, the reflection spectrum (blue) just behaves like the reflection spectrum of an empty cavity (green, dashed) but is shifted to a new resonance $\omega_c(x_0)$. Here we choose $g_{om} = \kappa$ and $\eta_{LD} = 0.01$, implying $r_{zp} = 0.02$.
b) If the zero-point motion is resolved, the reflection spectrum is broadened by roughly g_m and becomes shallower. Here we choose $g_{om} = 5\kappa$ and $\eta_{LD} = 0.2$, implying $r_{zp} = 2$.

Written in this form the connection between scattering theory and jump formalism becomes clear. The non-Hermitian term in H_s describes the rate that quantum jumps are applied to the motional wave function, which corresponds to the rate E_0^2 of incident photons on the cavity. The jump operators themselves, $J_{r/t} = E_0 S_{r/t}$, with $(J_r^\dagger J_r + J_t^\dagger J_t = E_0^2)$, are proportional to the single-photon scattering matrix elements in reflection and transmission, encoding the two processes by which the original wave function can change by becoming entangled with a scattered photon. Interestingly, the coherent part of the potential, $\mathrm{Re}[V(x)]$ in Eq. (3.18), is seen to arise from the term $S_r \rho S_r^\dagger$ in Eq. (3.29), and specifically from the interference between the incident and scattered components (first and second terms on the right of Eq. (3.27), respectively).

3.6 QUANTUM EFFECTS DUE TO ZERO-POINT MOTION

We have already seen that the scattering of a single photon on a cavity containing an atom leads to an entangled output state (3.26). This output state describes the coexistence of the possibilities of photon reflection and photon transmission and how the wave function of the atom gets modified for each of those events. We now proceed to describe some of the relevant observational consequences.

We can expand the position-dependent cavity detuning around a resonant position x_r (defined by $\Delta_c(x_r) = 0$) until linear order:

$$\Delta_c(x) \approx \delta_c + g_{om} u^2(x_r) - g_{om} \sin(2k_c x_r) k_c (x - x_r). \quad (3.31)$$

This is a good approximation in the Lamb-Dicke regime $\eta_{LD} \ll 1$. In order to predict observables, linearizing displacement is also a good approximation for $g_{om} \gg \kappa$, even if $\eta_{LD} \sim 1$, since then the cavity frequency shifts out of resonance for displacements $k_c \delta x \ll 1$. The term $\sin(2k_c x_r)$ indicates that the cavity frequency is most sensitive to displacements if $k_c x_r = \pm\pi/4$, halfway between a cavity node and anti-node. Then it can be seen that if the atomic wave function is centered around $k_c x_0 = k_c x_r = \pi/4$, the cavity frequency shifts by a linewidth κ, if the atom moves a distance of $k_c R = \kappa/g_{om}$. As the transmission/reflection of a single, near-resonant photon changes significantly as its frequency varies over a cavity linewidth, R can be viewed as the spatial resolution over which the single photon "learns" about the atomic position via its scattering direction. We will now define the zero-point resolution

$$r_{zp} \equiv (2x_{zp})/R = (2g_m)/\kappa, \quad (3.32)$$

with $g_m = g_{om}\eta_{LD}$ being the single-photon, single phonon coupling strength as defined in Sec. 3.3.1. The zero-point resolution tells us how much finer the resolution of an incident photon is compared to the width of the atomic wave function. It distinguishes two regimes: unresolved zero-point motion $r_{zp} \ll 1$, which corresponds to the usual regime of weak optomechanical interactions, and the resolved zero-point motion regime $r_{zp} \gg 1$, where the resolution of the system becomes smaller then the zero-point motion, which is until now unexplored and which gives rise to novel effects as we will demonstrate in the following.

3.6.1 *Influence of the zero-point motion on the reflection spectrum*

Here, we assume the atom to be initially in its motional ground state $\Psi_0(x) \propto e^{-\frac{1}{4}(x-x_0)^2/x_{zp}^2}$ with a trap equilibrium $k_c x_0 = \pi/4$ and $\kappa_r = \kappa/2$ (critical coupling). The spectrum of reflection, as a function of the incident photon frequency ω_L, is then given by

$$p_r(\omega_L) = \int dx |S_r(\omega_L, x)|^2 |\Psi_0(x)|^2. \quad (3.33)$$

Fig. 3.4a) shows p_r as a function of cavity detuning $\delta_c = \omega_L - \omega_c$ for $r_{zp} \ll 1$ (unresolved zero-point motion). The green dashed

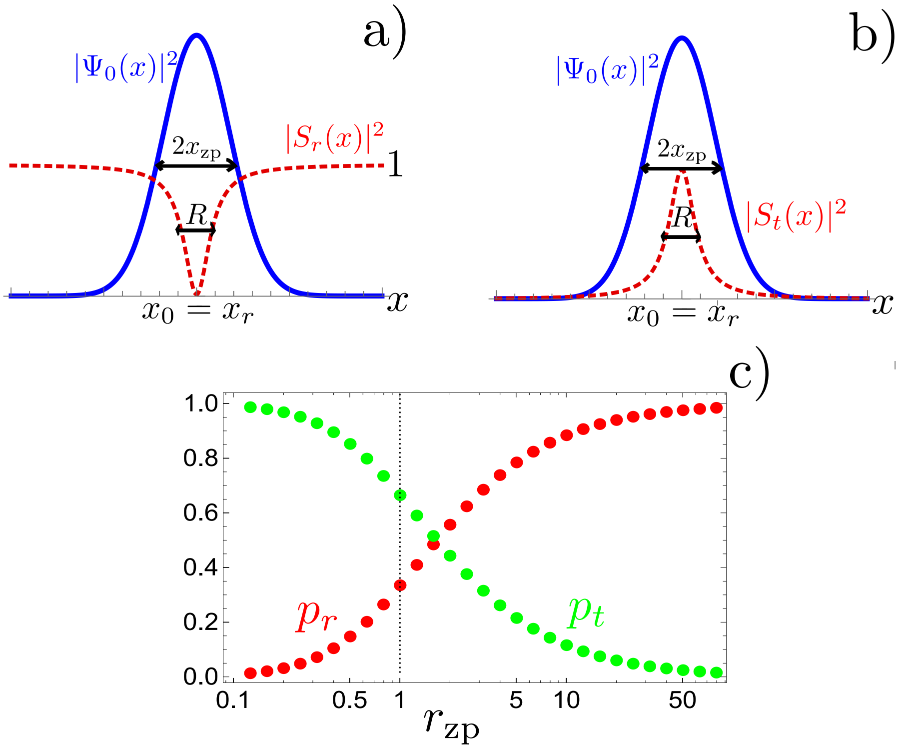

Figure 3.5: **Resolution beyond zero-point uncertainty**

a) For $r_{zp} = 2$, the spatial width $\sim 2x_{zp}$ of the atomic probability density $|\Psi_0(x)|^2$ (blue) exceeds the spatial resolution R, which corresponds to the width of the absolute value of the scattering matrix $|S_r(x)|^2$ (red dashed). As the cavity is only resonant with an incoming photon if the atom is located within R, there is a large probability that the cavity is off-resonant, even though $\omega_L = \omega_c(x_0)$. The probability of reflection is calculated by the overlap of both plotted functions.

b) Same as a), but with the absolute value of the S-matrix for transmission (red, dashed).

c) Probability of photon reflection p_r (red) and transmission p_t (green) as a function of zero-point resolution r_{zp}, for an incident photon that is resonant with the cavity in the limit that atomic motion fluctuations are ignored (i.e., $\delta_c = -g_{om}u^2(x_0)$). One sees that for large r_{zp}, the probability of transmission becomes negligible, because the probability of finding the atom within R (which would imply a resonant system and consequent transmission) approaches zero for $r_{zp} \gg 1$.

line is the reflection spectrum of an empty cavity with decay rate κ. The blue solid line is calculated with Eq. (3.33) for $r_{zp} = 0.02$, where $p_r \approx |S_r(\omega_L, x_0)|^2$. One can see that it exhibits the same Lorentzian response as an empty cavity, but with a resonance frequency shifted by $-g_{om}u^2(x_0)$. Fig. 3.4b) shows the reflection spectrum p_r for resolved zero-point motion $r_{zp} = 2$. We observe that the probability of reflection is strongly increased for $\delta_c = -g_{om}u^2(x_0)$, compared to the case of small r_{zp}. This behavior can be understood from Eq. (3.31). In particular, the resonance frequency of the coupled atom-cavity system depends on the position of the atom, and $\delta_c = -g_{om}u^2(x_0)$ corresponds to the resonance of the most likely atomic position. However, the large spread of the atomic wave function results in a large uncertainty of the resonance frequency, which increases the reflection probability. Conversely, an incident photon with frequency far from $\delta_c = -g_{om}u^2(x_0)$ sees a decreased reflection probability (thus the broadening of the spectrum), as there is some chance that the spread in atomic position allows the coupled system to be on resonance with the photon. This is illustrated in Fig. 3.5a), where we plot the atomic probability density $|\Psi_0(x)|^2$ (blue) and the absolute value of the reflection S-matrix $|S_r(x)|^2$ (red dashed) (Eq. 3.27) as a function of position x and for $r_{zp} = 2$. One can see, that the width of the atomic wave function $\sim 2x_{zp}$ exceeds the spatial resolution R, within which the cavity is resonant. For completeness, we also provide a plot of the absolute value of the transmission S-matrix $|S_t(x)|^2$ (red dashed) in Fig. 3.5b). Fig. 3.5c) shows the probability of reflection and transmission for $\delta_c = -g_{om}u^2(x_0)$ as a function of r_{zp}. For $r_{zp} \ll 1$ the probability of reflection vanishes and the transmission approaches unity as it would for an empty resonant cavity. However, with increasing r_{zp} it becomes less likely to find the atom within the spatial resolution R within which the cavity is resonant, leading to an increase of p_r. Finally, the reflection probability p_r approaches unity for $r_{zp} \gg 1$.

Most of this plot is already experimentally accessible with current technology. For example a neutral atom trapped in its ground state inside photonic crystal cavities can reach $r_{zp} \sim 10$ (Appendix A.8.1) whereas a current fiber cavity experiment reaches $r_{zp} \sim 1$ (Appendix A.8.2). While measuring p_r, the zero-point resolution r_{zp} can then be gradually decreased by increasing the atom-cavity detuning $\omega_0 - \omega_c$, increasing trap frequency ω_m or by moving the trap equilibrium x_0 away from the position of maximal optomechanical coupling $k_c x_0 = \pm\pi/4$. This procedure would experimentally reproduce parts of Fig. 3.5c).

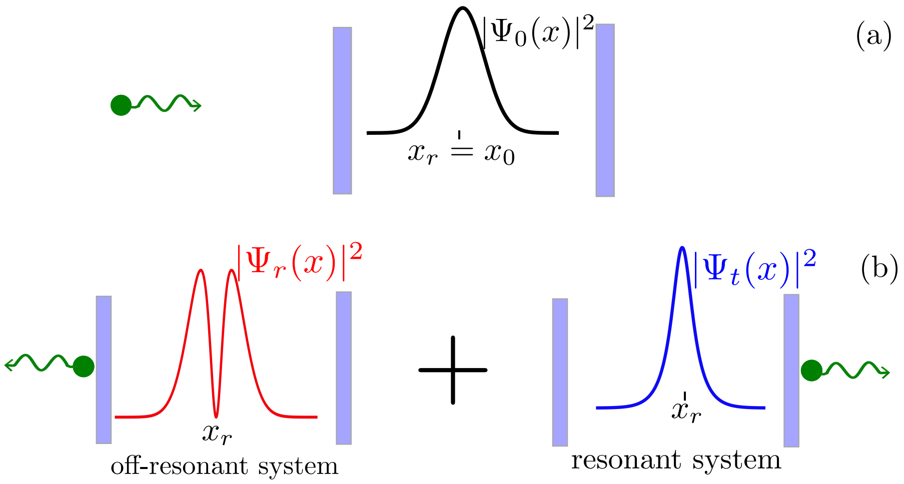

Figure 3.6: **Illustration of a single-photon scattering event for resolved zero-point motion**
a) Input state: An incident photon (green) with a frequency ensuring $x_0 = x_r$ is flying towards a cavity containing a trapped atom with probabilitiy density $|\Psi_0(x)|^2$ (black). Due to its zero-point uncertainty, the system is in an effective superposition of resonance frequencies. This input state is given by Eq. (3.22).
b) Output state: Illustration of the entangled output state given by Eq. (3.26), which is a superposition of the photon being reflected, which implies an off-resonant system and a photon being transmitted, which implies a resonant system. The plotted probability densities $|\Psi_{r/t}(x)|^2$ are the normalized product of $|\Psi_0(x)|^2$ and the respective scattering matrix $|S_{r/t}(x)|^2$ of Fig. 3.4a) and 3.4b), where $r_{zp} = 2$. For this value, the probability of reflection is $p_r \approx 0.56$.

3.6.2 *Entanglement and conditional projection of the atomic wave function*

Having previously investigated the unconditional reflection spectrum of an incident photon, we now study more carefully the correlations that build up between the atomic motion and photon reflection or transmission for the case when the trap equilibrium falls at the resonant position ($x_0 = x_r$). As the atom is in a coherent superposition of being within the spatial resolution R and not, and an incoming photon gets transmitted if the atom is within that spatial resolution and reflected if otherwise, the resulting state (Eq. 3.26) is entangled. Given that the photon has been transmitted, the normalized conditional wave function is given by

$$\Psi_t(x) = p_t^{-1/2} S_t(x) \Psi_0(x). \tag{3.34}$$

Its probability density is propotional to the product of $|\Psi_0(x)|^2$ and $|S_t(x)|^2$ as individually drawn in Fig. 3.5b). Thus, for $r_{zp} \gg$

1, the transmission of a photon projects the atom into a narrow spatial region $\Delta x \sim 1/R$ around the resonant position, which is consistent with the photon having seen a resonant cavity response.

In contrast, the reflection of a photon projects the atom away from that same spatial region, which results in a hole around x_r with width $\Delta x \sim 1/R$. This is consistent with the photon having seen an off-resonant cavity. The normalized conditional wave function after a photon reflection is then given by

$$\Psi_r(x) = p_r^{-1/2} S_r(x) \Psi_0(x). \tag{3.35}$$

As individually drawn in Fig. 3.5a), its probability density is propotional to the product of $|\Psi_0(x)|^2$ and $|S_r(x)|^2$. Fig. 3.6a) shows an illustration of the unentangled input state. The atom (black) is in its motional ground state, centered around $x_0 = x_r$, while a single photon (green) is incident and resonant with the atom-cavity system for this position. In Fig. 3.6b) we illustrate the entangled output state for $r_{zp} = 2$. We illustrate how the transmission or reflection of a photon are entangled with atomic wave functions $\Psi_t(x)$ or $\Psi_r(x)$ consistent with the respective scattering process, for the same parameters as in Figs. 3.4a) and b).

Interestingly, in the unresolved zero-point motion regime $r_{zp} \ll 1$ the scattering matrix for reflection is proportional to x: $S_r(x) \approx -2ix/R$. This leads to a final conditional wave function $\Psi_r(x) \propto x\Psi_0(x)$ which corresponds to a single-phonon Fock state. This represents the high-fidelity generation of a single-phonon Fock state, which is heralded on detection of a reflected photon (the probability of a single photon being reflected itself is quite low, $p_r \approx r_{zp}^2$). This approach is distinct from previous proposals for heralded generation, involving the detection of a Stokes-scattered photon in the sideband resolved regime [115].

The wave function after a transmission/reflection event adjusts in a way that it increases the probability of a subsequent transmission/reflection. To demonstrate this, we calculate the conditional probability of photon transmission given that a photon has just been transmitted:

$$p(t|t) = \frac{1}{p_t} \int dx |S_t(x, \omega_L)|^4 |\Psi_0(x)|^2. \tag{3.36}$$

Fig. 3.7a) shows $p(t|t)$ (green) as a function of cavity detuning δ_c for a fixed trapping position $k_c x_0 = \pi/4$. We plot the corresponding probability of transmission p_t (blue) as well, which is seen to be lower than the conditional probability. We use parameters of an existing fiber cavity QED experiment with trapped $^{40}Ca^{+}$-ions (Appendix A.8.2II). We chose $\omega_m = 2\pi \times$

50 kHz and $\omega_0 - \omega_c = 4g_0$. The asymmetry of $p(t|t))$ is due to the nonnegligible dependence of g_{om} (Eq. (3.12)) and $\kappa(x_0)$ (Eq. (3.11)) on the laser frequency ω_L (and thus δ_c) for those parameters. For $2\delta_c/\kappa = -(2g_{om}/\kappa)u^2(x_0) \approx -1.2$ (which implies $x_r = x_0$) a zero-point resolution of $r_{zp} \approx 0.89$ is obtained, which needs to be calculated with Eq. (A.65) as here spontaneous emission cannot be neglected. As one consequence of the higher likelihood of conditional transmission, the second-order correlation function $g^{(2)}_{tt}(0) = \frac{1}{p_t^2}\int dx|S_t(x,\omega_L)|^4|\Psi_0(x)|^2$ of the transmitted field, given a weak coherent input state, would exhibit bunching, as shown in Fig. 3.7b). Likewise, as reflection of a first photon suppresses the probability of transmitting a second photon (and vice versa), second-order correlations $g^{(2)}_{rt}(0) = \frac{1}{p_t p_r}\int dx|S_t(x,\omega_L)|^2|S_r(x,\omega_L)|^2|\Psi_0(x)|^2$ between the reflected and transmitted field would exhibit anti-bunching (Fig. 3.7c)).

3.6.3 *Motional heating induced by entanglement*

Each projection of the atomic wave function is associated with an increase in energy. We will now show that this energy can vastly exceed the energy added in free space or in a trap. In free space a recoil momentum $\hbar k_L$ results in a kinetic energy change of ω_{rec} (typically a few kHz). In a stiff trap ($\omega_{rec} \ll \omega_m$) it is unlikely that a phonon can be excited due to the insufficient energy associated with the recoil. In that case, it is well-known [116, 117] that the probability of exciting a phonon due to single-photon scattering is suppressed as $\omega_{rec}/\omega_m = \eta_{LD}^2$. However, here we show that for atoms trapped inside cavities, and in the regime of strong optomechanical coupling, it is possible for a single scattered photon to produce a much larger heating effect, even when the atom is trapped tightly within the Lamb-Dicke limit ($\eta_{LD} \ll 1$). The origin of this effect can already be inferred from Fig. 3.6b), where the post-scattering atomic wave function is seen to be far from the original ground-state wave function due to the narrow spatial features induced by scattering.

In Fig. 3.8a we plot the conditional expectation values $\bar{n}_{r/t} = \langle\Psi_{r/t}|\, b^\dagger b\, |\Psi_{r/t}\rangle$ of created phonons as a function of r_{zp} after measuring a reflected/transmitted photon, respectively. For these plots we assume the atom to be initially in its ground state and that the resonance position matches with the trap equilibrium ($x_r = x_0$). We find that $\bar{n}_r \approx 1$ for $r_{zp} \ll 1$, which reflects the fact that the resulting conditional wave function in this regime is a single-phonon Fock state, as explained in Sec. 3.6.2. For $r_{zp} \gg 1$ we observe a scaling of $\bar{n}_r \propto r_{zp}$, whereas $\bar{n}_t \propto r_{zp}^2$ for all val-

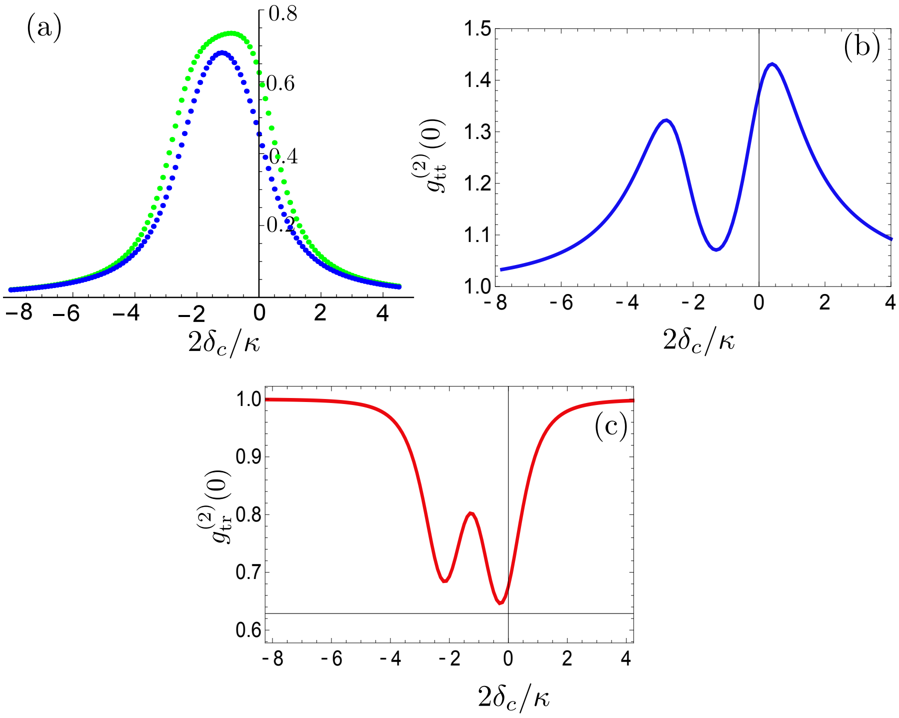

Figure 3.7: **Photon statistics due to wave function projection** for a fixed trapping position $k_c x_0 = \pi/4$.

a) Probability of photon transmission p_t (blue) as a function of cavity detuning δ_c and the conditional probability of transmission, given that a photon just has been transmitted $p(t|t)$ (green). We observe that a transmitted photon increases the probability of transmitting again.

b) The second-order correlation function $g^{(2)}_{tt}(0)$ of the transmitted field as a function of δ_c shows bunching due to the decay channel reinforcing nature of the wavefunction projection caused by the first photon.

c) The second-order correlations $g^{(2)}_{tr}(0)$ between the transmitted and the reflected field as a function of δ_c shows anti-bunching.

Here we use parameters of an existing fiber cavity QED experiment with trapped $^{40}\mathrm{Ca}^{+}$-ions with recoil frequency $\omega_{\mathrm{rec}} = 2\pi \times 6.8\,\mathrm{kHz}$ (see Appendix A.8.2I). The parameters are $g_0 = 2\pi \times 41\,\mathrm{MHz}$, $\gamma = 2\pi \times 11.2\,\mathrm{MHz}$, $\kappa = 2\pi \times 8\,\mathrm{MHz}$. We chose $\omega_m = 2\pi \times 50\,\mathrm{kHz}$ and $\omega_0 - \omega_c = 4g_0$. These values correspond to a zero-point resolution of $r_{zp} \approx 0.89$ for $2\delta_c/\kappa \approx -1.2$ (calulated with Eq. (A.65)).

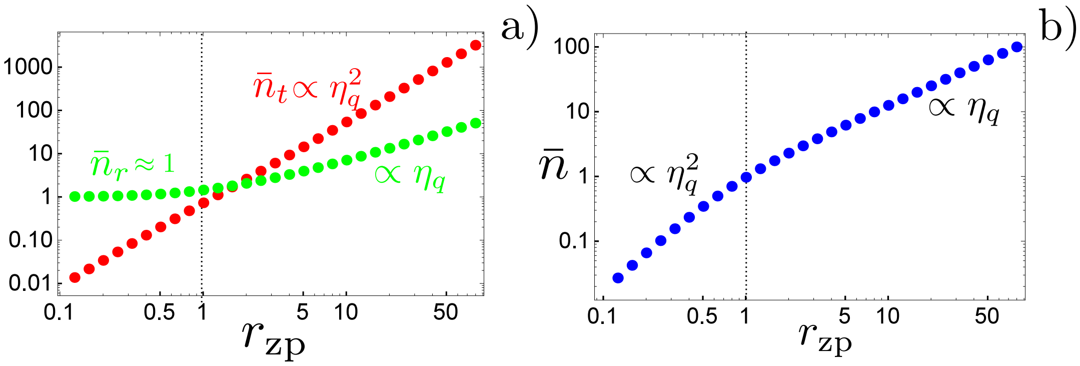

Figure 3.8: **Added phonons per photon**
We assume critical coupling, the atom to be initially trapped in its ground state and that the resonance position matches with the trap equilibrium ($x_r = x_0$). **a)** Conditional expectation values of created phonons after scattering a single photon $\bar{n}_{r/t}$. We find the scalings $\bar{n}_r \approx 1$ for $r_{zp} \ll 1$ and $\bar{n}_r \propto r_{zp}$ for $r_{zp} \gg 1$ and $\bar{n}_t \propto r_{zp}^2$ for all values of r_{zp}, leading to a very large number of added phonons for resolved zero-point motion in the case of a measured transmitted photon. **b)** Total expectation value $\bar{n}$ (unconditional) of added phonons per photon as a function of r_{zp}. The scalings $\bar{n} \propto r_{zp}^2$ for $r_{zp} \ll 1$ and $\bar{n} \propto r_{zp}$ for $r_{zp} \gg 1$ originate from the combination of a) and Fig. 3.5c), as $\bar{n} = p_t \bar{n}_t + p_r \bar{n}_r$.

ues of r_{zp}. We now want to give the intuition behind these scalings. Generally, the number of created phonons is the energy increase normalized with trap frequency: $\bar{n} = \frac{\Delta E}{\omega_m}$. The main contribution of added energy comes from the increase in momentum uncertainty, due to the narrow spatial features associated with the conditional wave functions after photon scattering (see Fig. 3.6b)). Thus, the added energy after one scattering event is approximately $\Delta E \approx \frac{\langle \Psi | p^2 | \Psi \rangle}{2m}$. Transmitting a photon localizes the atomic wave function around the resonant position x_r up to an uncertainty of $\Delta x \sim \hbar/\Delta p \sim 1/r_{zp}$, which yields a kinetic energy increase corresponding to $\bar{n}_t \propto r_{zp}^2$. The scaling $\bar{n}_r \propto r_{zp}$ for $r_{zp} \gg 1$ is best understood for the case $\kappa_t = 0$ (but the argument holds generally). There, the photon experiences a phase shift $\Phi(x) = \arg[S_r(x)] \approx \arctan[(2(x - x_r)R)/(R^2 - (x - x_r)^2)]$ which depends on the atomic position. $\Phi(x)$ only varies significantly for displacements smaller than $\delta x \lesssim R \propto 1/r_{zp}$ and its slope reaches a maximum value of $\Phi'(x_r) \propto r_{zp}$. The phase shift dominates the contribution to the added kinetic energy, $\bar{n}_r \propto \langle \Psi | p^2 | \Psi \rangle \propto \int dx |\Psi_0(x)|^2 (\Phi'(x))^2 \propto \int dx (\Phi'(x))^2 \propto r_{zp}^2 / r_{zp} = r_{zp}$ as for $r_{zp} \gg 1$, $(\Phi'(x))^2$ peaks over a region much smaller than the width of the wavefunction, and has a width of $\propto 1/r_{zp}$ and a maximum value of $\propto r_{zp}^2$.

In Fig. 3.8b) we plot the unconditional number of added phonons per photon $\bar{n}$ (the photon is not measured after the interaction). As it is given by $\bar{n} = p_t\bar{n}_t + p_r\bar{n}_r$, it can be understood as a combination of Figs. 3.8a) and 3.5c). Thus, the scaling of $\bar{n}_t$ dominates for $r_{zp} \ll 1$, whereas the scaling of $\bar{n}_r$ dominates for $r_{zp} \gg 1$.

3.6.4 *Conclusion*

We have presented the theory of strong optomechanical coupling in nano/micro-cavities, where naturally the mechanical sidebands are unresolved. Possible candidate platforms are trapped atoms or ions in photonic crystal cavities or fiber cavities. We show that these platforms already reach a regime where the atomic zero-point motion is resolved by incident photons, leading to strong entanglement between the photon and the atomic motion. Signatures of this entanglement can be measured in the reflection spectrum, the 2nd order photon correlation function or in the number of added phonons per photon. Furthermore, we showed that one can create non-Gaussian motional states from Gaussian states conditioned upon reflecting a single photon, even for unresolved zero-point motion. Generally we want to emphasize that the presented theory is relevant to any experiment where atoms are strongly coupled to cavities with small mode volumes.

4

REACHING THE OPTOMECHANICAL STRONG COUPLING REGIME WITH A SINGLE ATOM IN A CAVITY

4.1 INTRODUCTION

In the previous chapter, we showed how cavity QED experiments in the strong coupling regime are natural and attractive platforms to explore the single-photon, single-phonon strong coupling regime of optomechanics. While Chapter 3 focused on the strong coupling regime in the sideband unresolved limit, here we consider the sideband resolved limit. We note again (see Sec. 1.3.2) that attaining this limit represents a holy grail of optomechanics, as it effectively allows for the generation of non-classical states of light through strong motion-mediated photon-photon interactions. In particular, it has been theoretically shown that this regime enables optomechanically induced photon blockade [46], where only single photons can transmit through the cavity at a time.

In this Chapter, we show theoretically that one can observe optomechanically induced photon blockade [46] in realistic cavity QED setups, where a non-classical anti-bunched field is produced as the system is unable to transmit more than a single photon at a time. We also describe how this optomechanical behavior can be clearly distinguished from, and dominate over, the usual anti-bunching associated with the two-level nature of the atom. The explicit use of the strong coupling regime of cavity QED to attain novel regimes of optomechanics, and the examination of the resulting non-classical statistics of the outgoing field, distinguish the present work from previous experiments that explored optomechanical effects with atomic ensembles in cavities [61, 62, 85].

4.2 OPTOMECHANICAL PHOTON BLOCKADE

We begin by reviewing the phenomenon of photon blockade in a conventional optomechanical system. We focus on the system shown in Fig. 4.1a), where a mechanical element such as a trapped particle [19–21, 118, 119] or membrane [42] can be positioned arbitrarily, and couples to a single standing-wave optical mode of a Fabry-Perot cavity. For small displacements of the mechanical degree of freedom around the equilibrium position x_0, the cavity frequency is given by $\omega_c(x) \approx \omega_c(x_0) + \omega_c'(x_0)(x - x_0)$. The total Hamiltonian of the system, including a coherent external driving field, is given in a frame rotating with the laser frequency ω_L by

$$\begin{aligned} H_{op} = \quad & \omega_m b^\dagger b - (\omega_L - \omega_c(x_0) + i\frac{\kappa}{2})a^\dagger a \\ & + g_m(b + b^\dagger)a^\dagger a + \sqrt{\frac{\kappa}{2}} E_0(a^\dagger + a). \end{aligned} \tag{4.1}$$

Here, ω_m is the frequency of the vibrational mode, and a and b denote the photon and phonon annihilation operators, respectively. The quantity $\omega_L - \omega_c(x_0)$ is the detuning between laser frequency ω_L and the cavity frequency $\omega_c(x_0)$ when the mechanical system lies at its equilibrium position. Each cavity mirror has a decay rate of $\kappa/2$ into outgoing radiation, while the left side also serves as the source of injection of a coherent state into the cavity with photon number flux E_0^2. The position-dependent cavity shift described previously has been re-written in terms of phonon operators as $\omega_c'(x_0)(x - x_0) = g_m(b + b^\dagger)$ where $g_m = \omega_c'(x_0)x_{zp}$ is the single photon-phonon coupling strength and $x_{zp} = \sqrt{\hbar/(2m_{eff}\omega_m)}$ is the zero-point motional uncertainty (m_{eff} being the effective mass). The cubic interaction term $(b + b^\dagger)a^\dagger a$ gives rise to nonlinear equations of motion, but quantum signatures have not been observed, as the best ratio of coupling strength to linewidth so far is $g_m/\kappa \sim 10^{-2}$ [8, 9]. Thus, current experiments remain in the so-called optomechanical weak coupling regime, where many photons inside the optical mode are required to see an appreciable interaction, and allowing for linearization around the strong classical cavity field. However, here we will focus on the regime where this linearization breaks down and the nonlinear nature of the optomechanical coupling manifests itself via photon coincidence measurements [46].

To quantify the optomechanical nonlinearity we change into a displaced oscillator representation, which diagonalizes H_{op} in the limit of weak driving [46]. The eigenvalues as $E_0 \to 0$ can then be written as $E_{n,m} = m\omega_m + n\omega_c(x_0) - \frac{g_m^2}{\omega_m}n^2$and correspond to the (displaced) eigenstates $|n, m\rangle$. The spectrum is shown in Fig. 4.1b). If the laser frequency is resonant with the transition $|0_c, 0\rangle \to |1_c, 0\rangle$ (zero phonon line $\equiv$ ZPL) then the transition for the second photon is off resonant from the transition $|1_c, 0\rangle \to |2_c, 0\rangle$ by an amount $E_{2,0} - 2E_{1,0} = -2g_m^2/\omega_m$. In order to have a substantial effect, this anharmonicity should be resolvable, $g_m^2/\omega_m \gtrsim \kappa$, and furthermore, one should operate in the sideband resolved regime $\omega_m \gtrsim \kappa$ so that transitions to other motional states, e.g., the first phonon sideband $|0_c, 0\rangle \to |1_c, 1\rangle$ are suppressed. These requirements for antibunching can also be observed in Fig. 4.1c), where we have plotted the second-order correlation function $g^{(2)}(0)$ of the transmitted field given a weak coherent state input for different values of κ and g_m, taking the laser frequency ω_L as being resonant with the ZPL.

Formally, the quantum properties of the transmitted field are encoded in the input-output relation $a_{out}(t) = a_{in}(t) + \sqrt{\kappa/2}a(t)$. As the external driving field is injected through the other mirror, the input field in the transmitted port is the vacuum state, and thus the second-order correlation function $g^{(2)}(0) = \langle (a^\dagger_{out})^2 a^2_{out}\rangle / \langle a^\dagger_{out} a_{out}\rangle^2 = \langle (a^\dagger)^2 a^2\rangle / \langle a^\dagger a\rangle^2$ depends only on the intra-cavity field. We numerically calculate the necessary expectation values from the system wavefunction $|\Psi(t)\rangle = \sum_{n,m} c_{n,m}(t)\,|n,m\rangle$ (where n denotes the photon number and m the phonon number), which we truncate for $n_{max} > 2$ (given that a sufficiently weak input state is unlikely to generate more than two cavity photons), and m_{max} depending on convergence. In the case of the pure optomechanical Hamiltonian H_{op}, we solve for the steady-state amplitudes $c_{n,m}$ from the effective Schroedinger equation $i\,|\dot{\Psi}(t)\rangle = H_{op}\,|\Psi(t)\rangle$. Then, $\langle a^\dagger a\rangle = \sum_m |c_{1,m}|^2 + 2|c_{2,m}|^2$ and $\langle (a^\dagger)^2 a^2\rangle = \sum_m 2|c_{2,m}|^2$. Note that we neglect mechanical damping as our true subspace of interest consists of trapped atoms. Formally, the inclusion of cavity dissipation in the effective wavefunction evolution must be supplemented with stochastic quantum jumps [26]. However, in the weak driving limit $E_0 \to 0$ that we consider here, the effect of jumps on observables becomes vanishingly small and thus we do not need to explicitly account for them. While we have explicitly discussed the optomechanical Hamiltonian H_{op} here, the cases of the Jaynes-Cummings model without motion or Jaynes-Cummings model including motion are solved in an immediately similar fashion in the following.

A value of $g^{(2)}(0) < 1$ indicates non-classical antibunching, and a minimum value occurs around around $g_m \approx 0.5\omega_m$, which for well-resolved sidebands decreases as $g^{(2)}(0) \approx 20(\kappa/\omega_m)^2$. One also sees that increasing the ratio g_m/ω_m further does not improve the amount of antibunching, due to the possibility of resonantly coupling to other excited states. For example, at $g_m/\omega_m \approx 1/\sqrt{2}$, the reduced antibunching arises as a second photon can resonantly excite the state $|2_c, 1\rangle$, since $E_{2,0} - 2E_{1,0} = -\omega_m$.

While mathematically the degree of antibunching is determined by the parameters g_m, ω_m, κ, it will also be helpful to “visualize” how the antibunching changes as the equilibrium position x_0 is scanned from a cavity anti-node to node, to provide a useful comparison with atoms later. For a weak dielectric

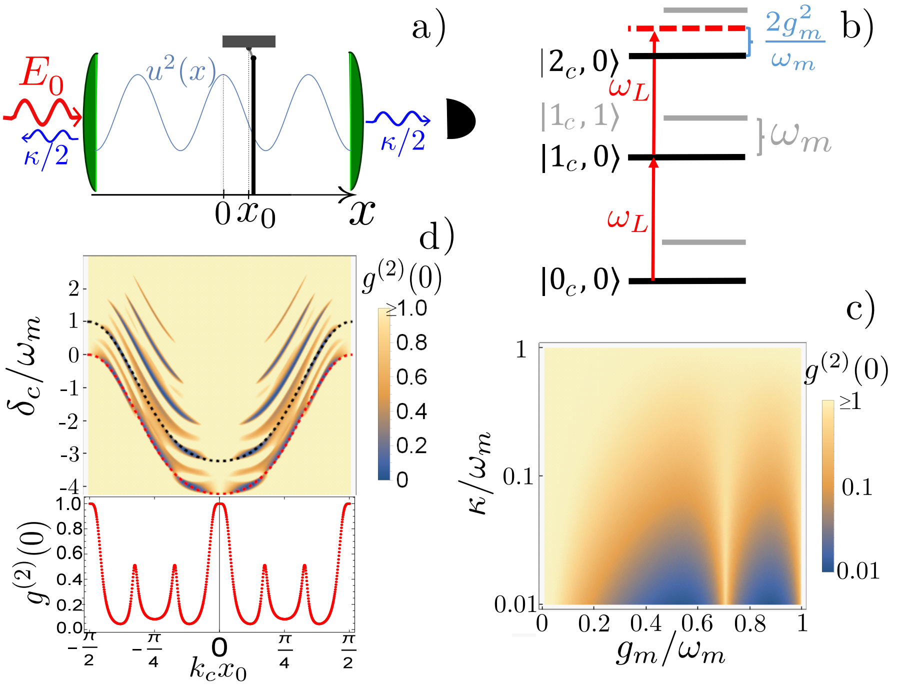

Figure 4.1: Optomechanical photon blockade. **a)** A membrane with equilibrium position x_0 inside a cavity with intensity mode profile $u^2(x)$, which is driven with number flux E_0^2 from the left. Each mirror has a decay rate of $\kappa/2$. The photons are measured on the transmitting side of the cavity (right). **b)** Spectrum of the optomechanical Hamiltonian H_{op} for $E_0 \rightarrow 0$. Here, $|n, m\rangle$ denotes the state with n photons and m phonons. In this diagram, we focus on transitions involving states with $m = 0$ phonons (black lines), while other states ($m = 1$ shown here) are denoted by gray lines. A laser with frequency ω_L, which is resonant with the transition $|0_c, 0\rangle \rightarrow |1_c, 0\rangle$ (the zero-phonon line), cannot resonantly excite a second photon $|2_c, 0\rangle$ as optomechanical interactions shift the relative energy of this state by an amount $2g_m^2/\omega_m$. **c)** Normalized second-order correlation function of the transmitted field, $g^{(2)}(0)$, as a function of g_m/ω_m and κ/ω_m. **d)** Top: $g^{(2)}(0)$ as a function of equilibrium position x_0 and detuning from the empty cavity $\delta_c = \omega_L - \omega_c$, normalized by the trap frequency ω_m. The mechanical system is coupled to an intensity mode profile $u^2(x) = \cos^2(k_c x)$, where k_c is the wavevector of the cavity mode. The dashed red/black lines denote a detuning where the cavity is resonantly driven on the zero phonon line (ZPL)/first phonon sideband, respectively. Bottom: $g^{(2)}(0)$ along the ZPL. The parameters chosen for Fig. 4.1d) are $g_{mo} = 2\pi \times 0.16\,\text{MHz}$, $\kappa = 2\pi \times 0.02\,\text{MHz}$, $\omega_m = 2\pi \times 0.2\,\text{MHz}$.

perturbation such as a thin membrane, intuitively one expects that the variation in the cavity frequency follows the intensity profile of the standing wave itself, $\delta\omega_c(x) \propto -\cos^2(k_c x)$ [22, 120]. It follows then that $g_m(x_0) = g_{mo}\sin(2k_c x_0)$. In particular, $g_m(x_0)$ vanishes at a node or anti-node, and reaches the maximum possible value of g_{mo} halfway between. In Fig. 4.1d) we plot $g^{(2)}(0)$ as a function of trapping position x_0 and detuning from the empty cavity $\delta_c = \omega_L - \omega_c$ for a mechanical system initially in its ground state. The dashed red line corresponds to a driving laser resonant with the ZPL, which requires the laser frequency to be tuned following the energy eigenvalue $E_{1,0}$. In addition to the features along the ZPL, antibunching can also be observed when a motional sideband $|1_c, m\rangle$ is resonantly driven, following the equation $|\omega_L = E_{1,m}\rangle$ (see black dashed curve for m=1). Below, we plot $g^{(2)}(0)$ following the ZPL (red, dashed). The oscillations in $g^{(2)}(0)$ along the ZPL versus x_0 occur as $g_m(x_0)$ sweeps into and away from the optimal values for antibunching (compare with Fig. 4.1c)). Here, we have chosen parameters of $g_{m0} = 2\pi \times 0.16\,\text{MHz}$, $\kappa = 2\pi \times 0.02\,\text{MHz}$ and $\omega_m = 2\pi \times 0.2\,\text{MHz}$. These do not necessarily correspond to a physically realizable optomechanical system, but allow the interesting features to be observed.

4.3 CAVITY QED WITHOUT MOTION

We now consider an atom coupled to a cavity mode with amplitude $u(x) = \cos(k_c x)$ (see Fig. 4.2a)), which is described by the Jaynes-Cummings (J-C) Hamiltonian [105]. Due to the two-level nature of the atom, the spectrum of the J-C Hamiltonian is nonlinear. We thus study the effect of this nonlinearity on $g^{(2)}(0)$ first without motion (i.e., the atom is infinitely tightly trapped), so that we can later clearly distinguish motional effects. The J-C Hamiltonian, in an interaction picture rotating at ω_L, is given by

$$\begin{aligned} H_{JC} = &-(\delta_0 + i\frac{\gamma}{2})\sigma_{ee} - (\delta_c + i\frac{\kappa}{2})a^\dagger a \\ &+ \sqrt{\frac{\kappa}{2}}E_0(a + a^\dagger) + g_0 u(x_0)(a^\dagger\sigma_{ge} + \text{h.c.}). \end{aligned} \tag{4.2}$$

The laser-atom detuning is $\delta_0 = \omega_L - \omega_0$ with ω_0 being the resonance frequency of the atom, while $\sigma_{\alpha\beta} = |\alpha\rangle\langle\beta|$, where $\alpha, \beta = g, e$ correspond to combinations of the atomic ground and excited states. As before, $\delta_c = \omega_L - \omega_c$ is the detuning relative to the bare cavity resonance. The atom-cavity coupling strength $g_0 u(x_0)$ depends on the trapping position x_0, where g_0 is the magnitude of the vacuum Rabi splitting at the anti-node at the cavity waist. The emission rate of an excited atom into

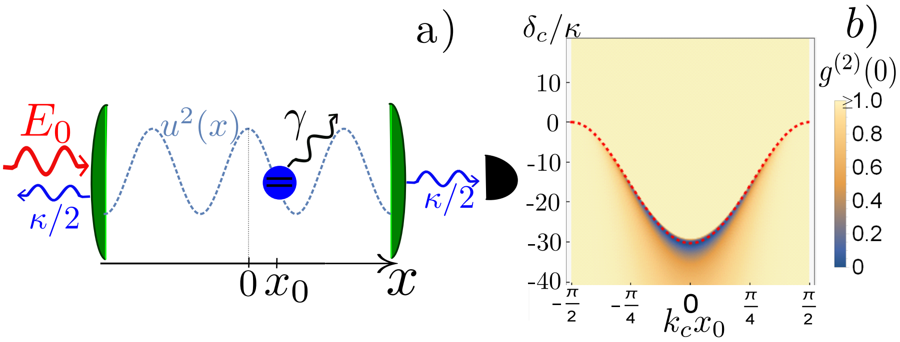

Figure 4.2: Cavity QED without motion. **a)** Schematic of an atom infinitely tightly trapped inside a cavity mode at position x_0. The cavity and atomic excited state decay rates are κ and γ, respectively. **b)** Second-order correlation function $g^{(2)}(0)$ of the transmitted field, as a function of trapping position x_0 and detuning from the empty cavity $\delta_c = \omega_L - \omega_c$, normalized by the cavity linewidth κ. Here, we restrict ourselves to driving frequencies near the resonance of the photon-like dressed state of the Jaynes-Cummings model. To generate this plot, we take idealized parameters such that antibunching arising from strong atom-cavity coupling can be easily seen: $\Delta = 3g_0$, $g_0 = 2\pi \times 2\,\mathrm{MHz}$, $\kappa = \gamma = 2\pi \times 0.02\,\mathrm{MHz}$.

free space is given by γ.

Ignoring dissipative processes for the moment, the system is block diagonal for n total excitations in the system, with possible states $|g, n\rangle, |e, n-1\rangle$. The energy eigenvalues in each block are given by $E_n^{\pm} = n\omega_c + (\pm\sqrt{4g_0^2 u^2(x_0)n + \Delta^2} + \Delta)/2$, where $\Delta = \omega_0 - \omega_c$. In the following we consider the dispersive regime $\Delta \gg g_0, \kappa, \gamma$, where the single-excitation eigenstates of the J-C Hamiltonian are either mostly atomic ($|\psi_+\rangle \approx |e, 0\rangle$) or photonic ($|\psi_-\rangle \approx |g, 1\rangle$). These eigenstates have corresponding eigenenergies $E_1^+ \approx \omega_0 + \frac{g_0^2}{\Delta}u^2(x_0)$ and $E_1^- \approx \omega_c - \frac{g_0^2}{\Delta}u^2(x_0)$, respectively. Here, we focus on the case when the system is driven near resonantly with the photonic eigenstate. In that limit, the atom can approximately be viewed as a classical dielectric that provides a position-dependent cavity shift $\propto \frac{g_0^2}{\Delta}$. However, the two-level nature of the atom provides a residual nonlinearity to excite a second photon, of magnitude $E_2^- - 2E_1^- \approx 2(g_0^4/\Delta^3)u^4(x_0)$. Such a nonlinearity results in an anti-bunched transmitted field if it is comparable to the cavity linewidth κ. In Fig. 4.2b) we plot $g^{(2)}(0)$ for $\Delta = 3g_0$, as a function of atom position x_0 and detuning δ_c, for frequencies around the photonic eigenenergy E_1^- (dotted line). Here, we have chosen idealized parameters $g_0 = 2\pi \times 2\,\mathrm{MHz}$, $\kappa = \gamma = 2\pi \times 0.02\,\mathrm{MHz}$, which enable the antibunching features to be clearly seen. Without motion, the largest degree of antibunching naturally occurs around the anti-node ($x_0 = 0$) and monotonically decreases as one approaches the nodes.

4.4 FULL MODEL: CAVITY QED WITH MOTION

We now include atomic motion into the Jaynes-Cummings Hamiltonian $H = \omega_m b^\dagger b + H_{JC}$ by treating $x_0 \to x$ as a dynamical variable. We assume that the atom sees an internal-state independent and harmonic trapping potential, which occurs naturally for trapped ions or using magic wavelength traps for neutral atoms [121]. In Fig. 4.3a), we plot $g^{(2)}(0)$ as a function of laser-cavity detuning δ_c and the central position x_0 of the trap, for parameters $g_0 = 2\pi \times 10\,\text{MHz}$, $\kappa = \gamma = 2\pi \times 0.02\,\text{MHz}$, $\Delta = 5g_0$, $\omega_m = 2\pi \times 0.5\,\text{MHz}$, and an atomic recoil frequency $\omega_{rec} = 2\pi \times 6.8\,\text{kHz}$ corresponding to a ${}^{40}\text{Ca}^+$ ion. It can be seen that this figure captures a combination of the pure J-C plot (Fig. 4.2b) and pure optomechanical plot (Fig. 4.1d), where the largest degree of antibunching occurs around the anti-node ($x_0 = 0$) or in between the node and anti-node, respectively. In particular, the presence of sideband features, and the extended antibunching away from the anti-node are qualitative signatures of motional effects. Below we plot $g^{(2)}(0)$ following the ZPL (red, dashed). The region of negligible antibunching, $g^{(2)}(0) \approx 1$, at $k_c x_0 \approx \pm\pi/8$ originates from an exact cancellation of the nonlinearities induced by motion and the two-level nature.

To better understand the contribution from motion, under certain conditions one can effectively map the J-C model to the optomechanical Hamiltonian. In particular, for large laser-atom detunings $\delta_0 \gg g_0$, the atomic ground-state population is approximately one which allows for an effective elimination of the atomic excited state [107, 122] using the Nakajima-Zwanzig projection operator formalism [108, 109]. In the Lamb-Dicke regime $\eta_{LD} = \sqrt{\omega_{rec}/\omega_m} = k_c x_{zp} \ll 1$ the effective optomechanical Hamiltonian (4.1) is reproduced by replacing $g_m \to g_{eff}$ with the effective optomechanical coupling strength $g_{eff} = g_0^2\delta_0/(\delta_0^2 + \gamma^2/4)\eta_{LD}\sin(2k_c x_0)$ and $\kappa \to \kappa_{eff}$ with the effective cavity linewidth $\kappa_{eff} = \kappa + \gamma g_0^2/(\delta_0^2 + \gamma^2/4)u^2(x_0)$, broadened by atomic spontaneous emission (see Sec. 3.3.1 and Appendix A.5.1 for the derivation of the effective optomechanical model: $g_{eff} = \Delta_c'(x_0)x_{zp}$ with Eq. (3.9) and κ_{eff} originates from averaging $\kappa(x)$ with the atomic wavefunction in Eq. (3.11)). Note that $\delta_0 \approx -\Delta$ for $\Delta \gg g_0$ and when the system is driven resonantly on the ZPL. For small η_{LD}, the nonlinearity arising from mo-

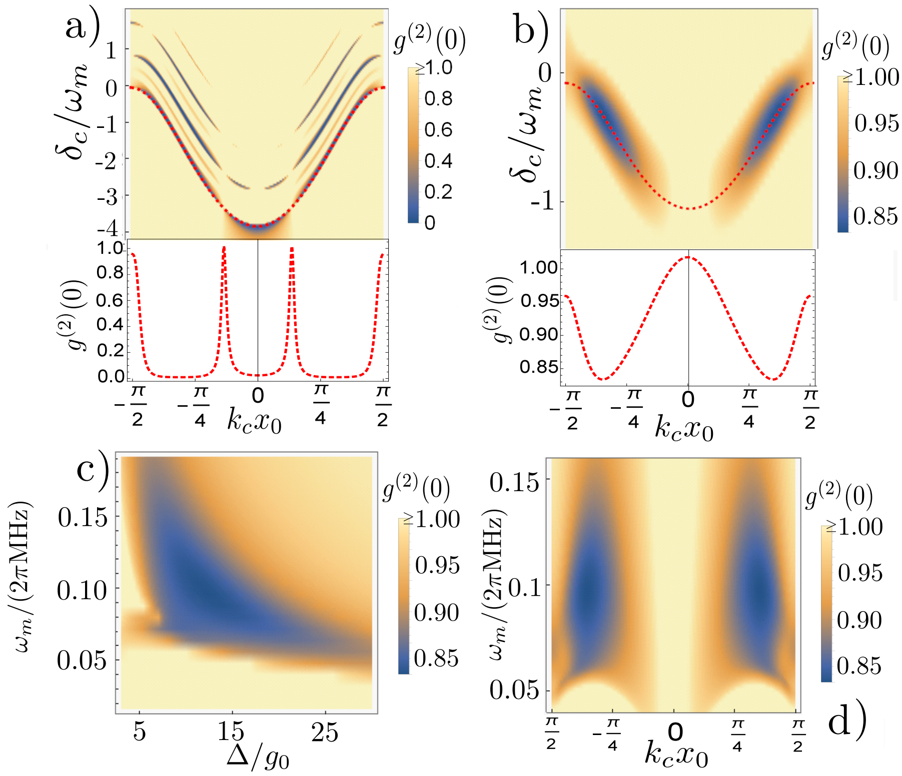

Figure 4.3: J-C model including motion. **a)** Top: $g^{(2)}(0)$ of the transmitted field versus trapping position x_0 and detuning from the empty cavity $\delta_c = \omega_L - \omega_c$, for detunings near the photonic eigenstate and for atom-cavity detuning $\Delta = 5g_0$. Here, we use idealized parameters $g_0 = 2\pi \times 10\,\text{MHz}$, $\kappa = \gamma = 2\pi \times 0.02\,\text{MHz}$, and $\omega_m = 2\pi \times 0.5\,\text{MHz}$ so that all of the key features can be clearly observed. Below: $g^{(2)}(0)$ following the ZPL (red, dashed). **b)** We plot the same as in Fig. 4.3a), but using the parameters for a realistic cavity QED experiment given below. In this figure, we choose $\Delta = 12g_0$ and $\omega_m = 2\pi \times 0.1\,\text{MHz}$. **c)** $g^{(2)}(0)$ as a function of atom-cavity detuning Δ and trapping frequency ω_m. **d)** $g^{(2)}(0)$ as a function of trapping position x_0 and trapping frequency ω_m for $\Delta = 12g_0$. For Fig. 4.3b), 4.3c) and 4.3d) we choose parameters $g_0 = 2\pi \times 1.4\,\text{MHz}$, $\kappa = 2\pi \times 0.05\,\text{MHz}$, $\gamma = 2\pi \times 11\,\text{MHz}$ and recoil frequency $\omega_{rec} = 2\pi \times 6.8\,\text{kHz}$.

tion simply adds to that arising from the two-level nature of the atom, and the energy spectrum reads

$$E_{n,m} \approx m\omega_m + \left(\omega_c - \frac{g_0^2}{\Delta}u^2(x_0)\right)n + \left(\frac{g_0^4}{\Delta^3}u^4(x_0) - \frac{g_{\text{eff}}^2}{\omega_m}\right)n^2. \tag{4.3}$$

Here, n denotes the number of excitations in the photon-like eigenstate of the J-C model. Thus, the essential ingredients needed to observe a quantum nonlinearity associated with the motion are $g_{\text{eff}}^2/\omega_m \gtrsim \kappa_{\text{eff}}$ and $\omega_m \gtrsim \kappa_{\text{eff}}$ (along with $\eta_{LD} < 1$, such that the atomic motion can be linearized, see Appendix A.9 for second order corrections). As the two-level and motional anharmonicities scale with Δ^{-3} and Δ^{-2}, respectively, increasing Δ serves as a way to make two-level antibunching vanish while nonlinear motional effects persist. Furthermore, as the maximum allowed value of g_{eff} to retain validity of the effective model is $g_{\text{eff}} \sim g_0$, one can see that the cavity QED strong coupling condition $g_0 \gtrsim \kappa$ naturally enables optomechanical strong coupling. Actually, the more conventional criterion for cavity QED strong coupling, $g_0 > \kappa, \gamma$, is not required, as we illustrate next.

4.5 MOTIONAL PHOTON BLOCKADE IN AN EXISTING EXPERIMENT

To present the realistic possibilities of observing optomechanical blockade, we consider an existing cavity QED setup with trapped $^{40}\mathrm{Ca}^+$-ions [123] with $g_0 = 2\pi \times 1.4\,\text{MHz}$, $\kappa = 2\pi \times 0.05\,\text{MHz}$ and $\gamma = 2\pi \times 11\,\text{MHz}$. Note that without motion, the large spontaneous emission rate $\gamma \gg g_0$ in this particular setup prevents one from observing blockade arising from the Jaynes-Cummings ladder when the atom and cavity are on resonance. Blockade cannot be observed by working off resonance either, as the nonlinearity in the spectrum decreases faster ($\propto \Delta^{-3}$) than the atomic contribution to the decay rate of the cavity ($\propto \Delta^{-2}$). However, optomechanical blockade can be observed as its nonlinearity decreases also as Δ^{-2}. In Fig. 4.3b) we plot $g^{(2)}(0)$ as a function of atom position x_0 and detuning δ_c, for $\Delta = 12g_0$ and $\omega_m = 2\pi \times 0.1\,\text{MHz}$, and also for a detuning δ_c following the ZPL (red, dashed). As the maximal two-level anharmonicity $2(g_0^4/\Delta^3)u^4(0) \approx 2\pi \times 1.6\,\text{kHz} \ll \kappa_{\text{eff}}$ is far from being resolved, no photon blockade occurs due to the two-level nature and thus no antibunching can be seen at the anti-nodes. However, the motional nonlinearity $2g_{\text{eff}}^2/\omega_m \approx 2\pi \times 15\,\text{kHz}$ is almost an order of magnitude larger and allows a minimum value of $g^{(2)}(0) \approx 0.83$ driving the ZPL (red dotted line) around $k_c x_0 \approx \pi/3$.

This value actually represents the optimum that can be observed at this position, scanning over the parameters ω_m and Δ/g_0 as we illustrate in Fig. 4.3c). For lower values of Δ, the sideband resolution is lost owing to the large value of the atomic spontaneous emission rate γ and its contribution to the effective cavity linewidth κ_{eff} ($\kappa_{\text{eff}} \approx 2\pi \times 84\,\text{kHz}$ at the optimized point). On the other hand, for increasing ω_m, the magnitude of the motional nonlinearity $2g_{\text{eff}}^2/\omega_m$ becomes reduced, while for decreasing ω_m again sideband resolution is lost. Note as well that the anti-bunching is negligible for any detuning, when the motion is frozen out ($\omega_m \to \infty$). This dependence of $g^{(2)}(0)$ on ω_m reveals the pure motional origin of antibunching. Fig. 4.3d) shows $g^{(2)}(0)$ as a function of atom position x_0 and trap frequency ω_m, for $\Delta = 12g_0$ and resonantly driving the ZPL. Here one again sees that the antibunching occurs only between the nodes and anti-nodes, and the tradeoff in ω_m.

4.6 CONCLUSION

In conclusion, we have shown that cavity QED experiments approaching the strong coupling regime are natural platforms to explore the single-photon, single-phonon strong coupling regime of optomechanics, in the limit that the motional sidebands can be resolved. Since many of those experiments, which allow for the realization of motional nonlinear effects, already exist, we anticipate that such platforms will stimulate much theoretical and experimental work to further explore the generation of non-classical light from motion and its consequences.

Part III

APPENDIX

APPENDIX

A

A.1 FREQUENCY SHIFT

Here, in relation with Chapter 2, we derive the frequency shift of a cavity due to the presence of a dielectric particle. For small frequency shifts $\delta\omega_c(x_p) = \omega_c(x_p) - \omega_c$ compared to the unaltered resonance frequency ω_c of the cavity, we can obtain $\delta\omega_c(x_p)$ from electromagnetic perturbation theory [124]:

$$\delta\omega_c(x_p) = -\frac{\omega_c}{2}\frac{\int d^3r\vec{P}(r)\cdot\vec{E}(r)}{\int d^3r\frac{d}{d\omega}\left(\epsilon(\omega,r)\omega\right)|E(r)|^2} \tag{A.1}$$

where $\vec{E}(r)$ is the electric field of the empty resonator, $\epsilon(\omega, r)$ is the dielectric function of the empty resonator, and $\vec{P}(r)$ is the additional polarization due to the presence of the particle. If we take the particle to be small compared to the wavelength of the laser, the electric field across the particle is approximately constant and its response is equivalent to a point dipole with polarizability $\alpha(\omega)$. As an example, for a dielectric sphere of volume V and refractive index n in vacuum, the polarizability can be exactly calculated, $\alpha(\omega) = 3\epsilon_0 V\frac{n^2-1}{n^2+2}$. For a given polarizability, one finds

$$\delta\omega_c(x_p) = -\frac{\omega_c\alpha(\omega)}{2\epsilon_0 V_m}f(x_p) \tag{A.2}$$

with $f(x) = \frac{\frac{d}{d\omega}(\epsilon(\omega,x)\omega)|E(x)|^2}{\max_x \frac{d}{d\omega}(\epsilon(\omega,x)\omega)|E(x)|^2}$ describing the dimensionless spatial intensity profile of the empty cavity, normalized to be 1 at the intensity maximum. V_m is the mode volume of the empty resonator and is defined as follows:

$$V_m = \frac{\int d^3x\frac{d}{d\omega}\left(\epsilon(\omega,x)\omega\right)|E(x)|^2}{\max_x \frac{d}{d\omega}\left(\epsilon(\omega,x)\omega\right)|E(x)|^2} \tag{A.3}$$

A.2 SCATTERING RATE OF THE TRAPPED PARTICLE

Here we consider the scattering of light by the trapped object itself, which decreases the cavity quality factor by contributing to its loss rate $\kappa = \kappa_{ex} + \kappa_{int} + \kappa_{scat}(x_p)$. The scattering rate for sub-wavelength particles reads:

$$\kappa_{scat}(x_p) = \sigma_{scat}c\frac{f(x_p)}{V_m}, \tag{A.4}$$

with V_m being the mode volume, c the photon velocity, and $\sigma_{scat} = \frac{k^4}{6\pi\epsilon_0^2}|\alpha(\omega)|^2$ the Rayleigh scattering cross-section (where $k = \frac{2\pi}{\lambda}$ is the wavevector of the incident light). We begin by comparing the relative effects of the position dependent scattering rate and cavity frequency shift on the intra-cavity photon number.

Fig. 2.2b) in the main text shows how the particle motion shifts the resonance peak of the intra-cavity photon number spectrum. In contrast, a position dependent scattering rate does not shift the peak, but instead alters its width and height. With this picture in mind we can neglect the effect of the position dependent scattering rate, if the change in scattering rate $\delta\kappa(x_p) = \kappa_{scat}(x_p)$ is much smaller than the frequency shift $\delta\omega_c(x_p)$ induced by the same particle movement. Using Eq. (A.4) and Eq. (2.6) and comparing these two quantities yields:

$$\frac{|\delta\kappa_{scat}(x_p)|}{|\delta\omega_c(x_p)|} \sim (kr)^3 \ll 1, \tag{A.5}$$

which allows us to neglect the position dependence of the scattering rate for sub-wavelength particles.

Nonetheless we have to consider the reduced quality factor of the resonator-particle system due to scattering of light. The total cavity decay rate is $\kappa = \frac{\omega_c}{Q} + \kappa_{scat}(x_0)$ where $Q = \frac{\omega_c}{\kappa_{ex}+\kappa_{int}}$ is the quality factor of the empty cavity. Thus, the back-action parameter reduces to

$$\eta = Q\frac{\alpha(\omega)}{\epsilon_0 V_m}\frac{1}{1+\frac{\kappa_{scat}(x_0)}{\kappa_{ex}+\kappa_{int}}}. \tag{A.6}$$

From Eq. (A.4), assuming that $\alpha(\omega) \approx \epsilon_0 V$ and writing $V_m = \nu\left(\frac{\lambda}{2}\right)^3$, where ν tells us how close the light is focused to the diffraction limit, the scattering rate reads

$$\kappa_{scat}(x_p) \approx \kappa_{scat}(x_0) \lessapprox \frac{8\epsilon^2}{27\pi^2\nu}(kr)^6\omega_L. \tag{A.7}$$

Inserting this into Eq. (A.6) finally yields

$$\eta = \frac{4}{3\pi^2}\frac{Q}{\nu}\frac{(kr)^3}{1+\frac{Q}{\nu}\frac{8}{27\pi^2}(kr)^6}, \tag{A.8}$$

and is plotted in Fig. A.1 for $\nu = 1$. In the limit that $\frac{Q}{\nu}\frac{8}{27\pi^2}(kr)^6 \ll 1$, we recover our results from the main text where scattering is negligible, and decreasing the mode volume or increasing the

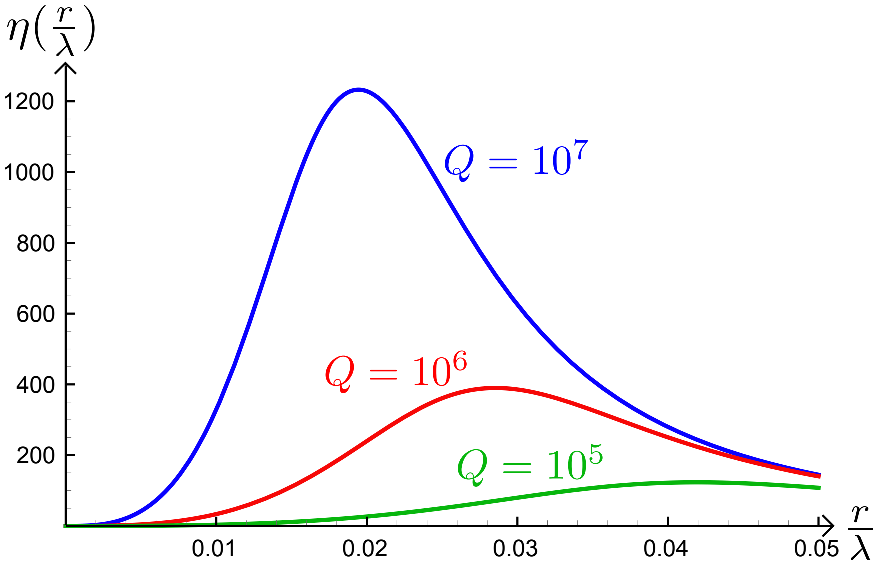

Figure A.1: Plot of the back-action parameter as a function of particle size after considering particle induced scattering losses as described by Eq. (A.8). Here we take $\nu = 1$ and empty-resonator quality factors of $Q = 10^5, 10^6, 10^7$.

quality factor has the same effect on the back-action parameter. In general, however, for a given value of $\frac{Q}{\nu}$ for an empty resonator, there is a maximum achievable η,

$$\eta_{\max} = \sqrt{\frac{3Q}{2\pi^2\nu}}, \tag{A.9}$$

which occurs at an optimized particle size of

$$kr = \sqrt[6]{\frac{27\pi^2\nu}{8Q}}. \tag{A.10}$$

A.3 TIME AVERAGED EXPERIENCED INTENSITY

Here we want to derive Eq. (2.10) of the main text. In order to do so, we multiply Eq. (2.4) with $\frac{f(x)}{f'(x)} \cdot dt$ and integrate both sides over a quarter of an oscillation period:

$$\int_0^{p_{\max}} dp \frac{f(x)}{|f'(x)|} = \frac{\omega_c \alpha(\omega)}{2V_m} \int_0^{\frac{T}{4}} dt \cdot n(x(t)) \cdot f(x(t)) \tag{A.11}$$

We integrate from the classical turning point (where the momentum is zero) to the trap minimum (where the momentum is maximal) which relates to a quarter of the oscillation period T. Using Eq. (2.9) of the main text, the right side of the previous equation is proportional to the time averaged experienced intensity and we can formally rewrite Eq. (A.11) as follows:

$$\langle I_{\exp} \rangle_t = \frac{4c}{T\alpha(\omega)} \int_0^{p_{\max}} dp \frac{f(x)}{|f'(x)|} \tag{A.12}$$

To proceed we make two approximations: First we approximate the oscillation period T in the high back-action regime as $T \approx 4\frac{x_t}{v_{max}}$. In particular, the particle moves in a square well with length $\delta x = 2x_r = 2x_t$, where x_t is the classical turning point, and v_{max} is the maximum velocity in the middle (minimum) of the potential. Additionally, in the high back-action regime the particle significantly changes its momentum only around the classical turning point x_t when it hits one of the edges of the square well. Since the momentum change occurs in a narrow region, we can approximate in the integral $f(x) \approx f(x_t)$ and $|f'(x)| \approx |f'(x_t)|$. These approximations lead to the following equation:

$$\langle I_{exp} \rangle_t \approx \frac{c\epsilon_0}{\alpha(\omega)} \frac{2}{x_t} \frac{f(x_t)}{|f'(x_t)|} E_{kin} \tag{A.13}$$

where $v_{max} \cdot p_{max} = 2E_{kin}$, with E_{kin} being the maximal kinetic energy in the trap. Now we can normalize this time averaged experienced intensity with the time averaged experienced intensity of the optical tweezer regime. We begin with expanding the potential Eq. (2.8) for small η:

$$U_T(x) = -2\hbar \frac{\kappa_{ex}}{\kappa} E_0^2 \frac{\eta}{1+\tilde{\Delta}^2} f(x). \tag{A.14}$$

Since $f(x)$ only varies between 0 and 1, it follows that the trap depth δU_T is given by

$$\delta U_T = 2\hbar \frac{\kappa_{ex}}{\kappa} E_0^2 \frac{\eta}{1+\tilde{\Delta}^2}. \tag{A.15}$$

Next we insert Eq. (2.7) of the main text, and assume that the particle is tightly trapped ($k\delta x \ll 1$) around the point of maximum intensity. As the change in intra-cavity photon number is negligible, we can approximate $n(x_p) \approx n(x_0)$. Eq. (2.9) from the main text then predicts that

$$\langle I_{exp,T} \rangle_t = \frac{c\hbar\omega_L}{2V_m} n(x_0) f(x_0) \tag{A.16}$$

in the optical tweezer regime. For the case where the particle is trapped around the antinode of the fundamental mode of a Fabry-Perot cavity:

$$\langle I_{exp,T} \rangle_t = \frac{c\epsilon_0}{\alpha(\omega)} \delta U_T. \tag{A.17}$$

Normalizing Eq. (2.10) with Eq. (A.17) and ensuring that $\delta U = \delta U_T$ for all η yields:

$$\frac{\langle I_{exp} \rangle_t}{\langle I_{exp,T} \rangle_t} \approx \frac{2}{x_t} \frac{f(x_t)}{|f'(x_t)|} \frac{E_{kin}}{\delta U}. \tag{A.18}$$

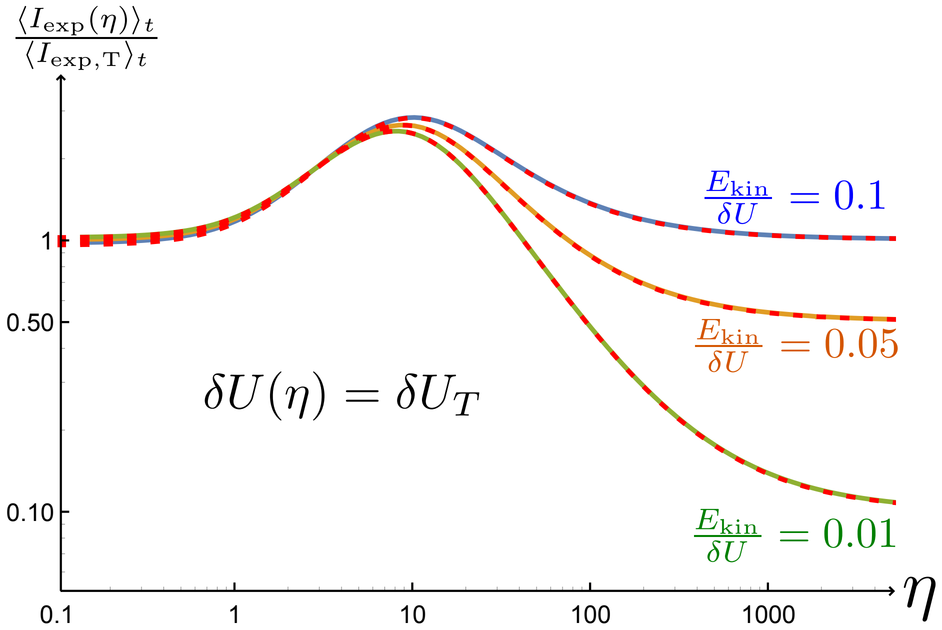

Figure A.2: Plot of the time-averaged experienced intensity of the particle as a function of back-action parameter $\langle I_{\mathrm{exp}}(\eta)\rangle_t$, normalized by the value in the optical tweezer regime $\eta \ll 1$. The two cases are set to have equal trap depth. The plot is numerically calculated for the case of trapping in the fundamental mode of a Fabry-Perot cavity $f(x) = \cos^2(kx)$ with resonant positions $kx_r = \frac{\pi}{10}$. The red line shows the excellent agreement between Eq. (A.17) and the numerical simulation of Eq. (2.9) in the main text.

Surprisingly this equation is valid for all η as long as the particle is confined sufficiently close to the antinode. Fig. A.2 shows the excellent agreement between the numerical simulation and the analytic solution obtained by Eq. (A.18). Taking the limit $\eta \to \infty$ of Eq. (A.18) implies $x_t \to x_r$ which reproduces Eq. (2.10) of the main text:

$$\lim_{\eta\to\infty} \langle I_{\exp}(\eta)\rangle_t = \frac{2c\epsilon_0}{\alpha(\omega)} \frac{f(x_r)}{|f'(x_r)|} \frac{E_{\mathrm{kin}}}{x_r} \tag{A.19}$$

A.4 OPTIMIZATION OF THE HARMONIC BACK-ACTION REGIME

Here we want to maximize the spring constant $k_{\mathrm{opt}} = k_{\mathrm{hb}} + k_T$ given by Eq. (2.11) in the main text. $k_{\mathrm{hb}} = \sum_i n_i'(x_0)\omega_{c,i}'(x_0)$ describes the first term in Eq. (2.11) and originates from changes of photon number with particle position, whereas k_T is the familiar term known from optical tweezers. The optimization is done for a fixed experienced intensity $\langle I_{\exp}\rangle_t$ if we consider two trapping modes of a cavity. As a result we will derive Eq. (2.12) and Eq. (2.13) in the main text and conclude how to optimally choose the laser detunings for the trapping modes.

We focus on the regime where the trap minimum x_0 is located roughly at a distance $\sim \frac{1}{k\eta}$ away from both resonant positions, where the photon number $n(x_p)$ can be linearized around the trap minimum x_0 for each trapping mode i: $n_i(x) \approx n_i(x_0) + n_i'(x_0)(x - x_0)$. A linear change in photon number with displacement implies a harmonic trap, because the force is proportional to the photon number (see Eq. (2.4) and Eq. (2.6) in the main text and note that $f_i'(x) \approx f_i'(x_0) \approx f_i'(x_{ri})$ for $k\delta x \ll 1$). Using Eq. (2.9) in the main text, the term proportional to $n_i'(x_0)$ does not contribute to the time-averaged intensity due to the harmonic motion. Under these circumstances Eq. (A.16) is valid in the harmonic back-action regime as well and the particle experiences the following time averaged intensity from each trapping mode i:

$$\langle I_{\exp,i}\rangle_t \approx \frac{2E_0^2\kappa_{\mathrm{ex}} c\hbar\omega_L}{\kappa^2 V_m} \frac{f_i(x_0)}{1 + (\eta f_i'(x_{ri}))^2 (x_0 - x_{ri})^2}, \tag{A.20}$$

where we linearized the mode profiles around their resonant positions in Eq. (2.9) in the main text. This is a good approximation if the the width of the intensity peaks is smaller than the spatial variations of the mode profiles, which is the case for $\eta \gg 1$. Now can write the contributions to the first term k_{hb} of Eq. (2.11) in the main text as:

$$k_{\mathrm{hb},i} \approx 4E_0^2 \frac{\kappa_{\mathrm{ex}}}{\kappa} \left(\eta f_i'(x_{ri})\right)^2 \frac{\eta |f_i'(x_{ri})(x_0 - x_{ri})|}{\left(1 + (\eta f_i'(x_{ri}))^2 (x_0 - x_{ri})^2\right)^2}. \tag{A.21}$$

Expressing the optical tweezer term k_T in the same way, we can write $k_{opt,i}$ in terms of $\langle I_{exp,i}\rangle_t$:

$$k_{opt,i} = \frac{\alpha(\omega)}{c\epsilon_0}\langle I_{exp,i}\rangle_t \frac{1}{f_i(x_0)}\left[\frac{2r_i}{1+r_i^2}\eta_i f_i'(x_{ri})^2 - f_i''(x_0)\right]. \quad (A.22)$$

$r_i = |\eta_i f_i'(x_{ri})(x_{ri} - x_0)|$ physically describes the ratio between half of the width of an intensity peak $\frac{1}{\eta_i f_i'(x_{ri})}$ and the distance of the respective resonant position of mode i from the trap minimum $|x_{ri} - x_0|$. The spring constant is maximized for $r_i = 1$ for which Eq. (A.22) reduces back to Eq. (2.12) in the main text. For $\eta_i \gg 1$ and $r_i = 1$ the contribution to the spring constant proportional to $f_i''(x_0)$ can be neglected and the spring constant purely arises from changes of photon numbers with particle position. In contrast, for $\eta \ll 1$ we can neglect the contribution proportional to $f_i'(x_0)^2$ reaching again the optical tweezer regime.

Eq. (2.13) in the main text is derived by forming the ratio of these two contributions to the spring constant $\frac{k_{hb}}{k_T}$ and comparing the two experienced intensities necessary to create the same spring constant in each regime. To derive this, we also assume that the trapping modes consist of the first and second modes of a Fabry-Perot cavity, which have equal back-action parameters η_i. We also use that $\langle I_{exp,1}\rangle_t f_2(x_0) \approx \langle I_{exp,2}\rangle_t f_1(x_0)$ using Eq. (2.4) in the main text with Eq. (A.16) and $|f_1'(x_0)| \approx |f_2'(x_0)|$ close to the trap minimum.

A.5 FROM THE JAYNES-CUMMINGS MODEL INCLUDING MOTION TO AN EFFECTIVE MODEL OF MOTION ONLY

Eq. (3.2) of the main text describes the full master equation of a moving two-level atom interacting with a cavity, in the presence of cavity losses and atomic spontaneous emission. In the limit where the cavity is driven near resonantly and the atom is far-detuned, the atomic excited state can be eliminated to yield an effective optomechanical system involving just the atomic motion and the cavity mode. One can go a step further and eliminate the cavity mode, to yield the reduced dynamics of just the atomic motion. The procedure by which a certain degree of freedom can be eliminated from an open system is known as the Nakajima-Zwanzig projection operator formalism [106, 108, 109], which we now describe here.

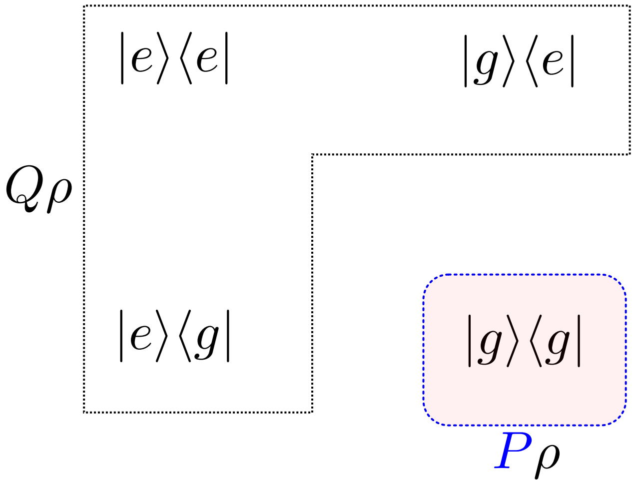

Figure A.3: The complete Hilbert space of the internal degrees of freedom of the atom. $P\rho$ is the part we are interested in and the remainder is characterized by the projection operator Q.

A.5.1 *Projecting out the atomic excited state*

First, we want to eliminate the atomic excited state from the full dynamics of Eq. 3.2. It is convenient to define a set of operators P, Q, which project the entire system density matrix

$$\rho = |g\rangle\langle g|\rho_{gg} + |g\rangle\langle e|\rho_{ge} + |e\rangle\langle g|\rho_{eg} + |e\rangle\langle e|\rho_{ee}, \tag{A.23}$$

into the subspace spanned by $|g\rangle\langle g|$ (which we want to project the dynamics into), and its orthogonal $1 - |g\rangle\langle g|$. Here $\rho_{ij} = \langle i|\rho|j\rangle$ are the reduced density matrices for the reduced Hilbert space, which still contain all other existing degrees of freedom. Thus, we define a projection operator P:

$$P\rho = |g\rangle\langle g|\rho_{gg} \tag{A.24}$$

and its complementary

$$Q\rho = |g\rangle\langle e|\rho_{ge} + |e\rangle\langle g|\rho_{eg} + |e\rangle\langle e|\rho_{ee}. \tag{A.25}$$

It is straightforward to show $P^2 = P, Q^2 = Q, QP = 0, P + Q = 1$. In Fig. A.3 we draw a simple picture of the full Hilbert space of the internal degrees of freedom of the atom in order to visualize the part of the Hilbert space we are interested in (described by $P\rho$) and the part we are not (described by $Q\rho$). We will now divide the super-operator L up in parts according to the way they act on the Hilbert space describing the internal degrees of freedom of the atom:

$$L = L_0 + L_a + L_I + J. \tag{A.26}$$

Here, $L_o = L_m + L_c$ is composed of terms that do not act on the internal degrees of freedom, with L_m and L_c describing respectively the trapped atomic motion and the bare dynamics of the driven cavity mode:

$$L_m \rho = -i[\omega_m b^\dagger b, \rho] \tag{A.27}$$

$$L_c \rho = i\delta_c[a^\dagger a, \rho] - i\sqrt{\kappa_r} E_0[(a + a^\dagger), \rho] - \frac{\kappa}{2}\left(a^\dagger a \rho + \rho a^\dagger a - 2a\rho a^\dagger\right). \tag{A.28}$$

The super-operator

$$L_a \rho = i\delta[\sigma_{ee}, \rho] - \frac{\gamma}{2}\{\sigma_{ee}, \rho\} \tag{A.29}$$

acts on $|e\rangle\langle g|, |g\rangle\langle e|, |e\rangle\langle e|$ (the subspace spanned by Q) and just multiplies those terms by a c-number. It describes evolution and damping of the excited internal state of the atom.

$$L_I \rho = -i[g(x)(\sigma_{eg} a + \sigma_{ge} a^\dagger), \rho] \tag{A.30}$$

acts on all the states and all Hilbert spaces, describing the interaction of the atom with the cavity field and

$$J\rho = \gamma \sigma_{ge} e^{-ik_c x} \rho e^{ik_c x} \sigma_{eg} \tag{A.31}$$

describes the spontaneous jump of the excited state of the atom into its ground state accompanied by a momentum recoil. In Fig. A.4 we draw arrows showing how these super-operators act on different parts of the Hilbert space of atomic internal degrees of freedom. We are interested in the dynamics of the subspace $P\rho$, while accounting for fluctuations into $Q\rho$. Thus, only closed loops which start and end in $P\rho$ contribute to the evolution of the reduced density matrix $P\rho$. To see how this works, we define $v = P\rho$ and $w = Q\rho$ and insert $P + Q = 1$ into Eq. (3.2):

$$\dot{v} = P\dot{\rho} = PL\rho = PLP\rho + PLQ\rho. \tag{A.32}$$

Let us first look at PLP:

$$PLP\rho = P(L_o + L_a + L_I + J)P\rho. \tag{A.33}$$

To quickly identify vanishing terms we take advantage of Fig. A.4 by following the path the super-operators take us through the Hilbert space applying them from the right to the left. Here are some examples:

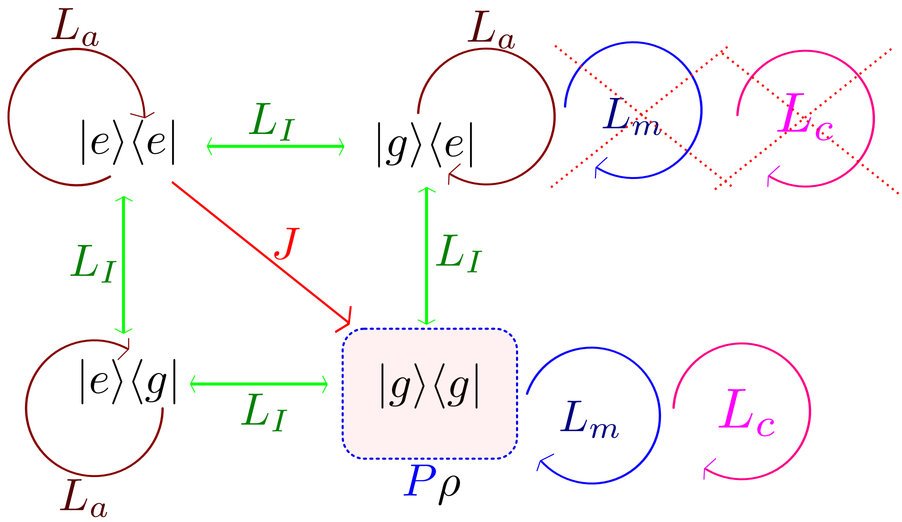

Figure A.4: The Hilbert space of the internal degrees of freedom of the atom. The notation is as follows: The label of an arrow corresponds to a Liouvillian, while the direction of the arrow indicates the possible beginning and ending subspaces of the Liouvillian. For example, the red arrow indicates that the Liouvillian J acting on the subspace $|e\rangle\langle e|$ takes this subspace to $|g\rangle\langle g|$. Since we assume δ_0 or γ to be much larger than κ and ω_m, we can neglect the action of $L_o = L_m + L_c$ during a fluctuation out of $P\rho$, which we indicate by crossing them out in the right-top corner and neglecting them in Eq. (A.35).

1. The term PL_IP: P projects into the subspace $|g\rangle\langle g|$, while L_I maps a state from P to Q. Thus, acting again with P causes this term to vanish.
2. PL_aP: P projects into $|g\rangle\langle g|$ and we immediately see that L_a does not act on it, so this term vanishes.
3. $PJP = 0$ because J does not act on $|g\rangle\langle g|$.

After identifying all vanishing terms, we obtain:

$$\dot{v} = L_o v + P(J + L_I)w \tag{A.34}$$

and

$$\dot{w} = QL_I v + Q(L_o + L_a + L_I)w. \tag{A.35}$$

Note that w describes the evolution of the fluctuations out of the subspace of interest. As the timescale of these fluctuations is set by δ_0 and γ and we assume that either δ_0 or γ is much larger than both ω_m and κ, we can neglect the free evolution of the cavity or motion during one of these fluctuations and approximate $L_o w \approx 0$ in Eq. (A.35), as also indicated in Fig. A.4. Then the general solution to this equation reads:

$$w(t) = \int_0^t d\tau e^{Q(L_o+L_a)(t-\tau)} QL_I w(\tau) + \int_0^t d\tau e^{Q(L_o+L_a)(t-\tau)} QL_I v(\tau) \tag{A.36}$$

where we set $w(0) = 0$ as the initial condition. Now we plug this equation twice into Eq. (A.34) (iteratively) in order to catch a term of the order JL_I^2:

$$\begin{aligned}\dot{v}(t) = {} & L_o v + P(J + L_I) \int_0^t d\tau e^{Q(L_o+L_a)(t-\tau)} QL_I v(\tau) \\ & + P(J + L_I) \int_0^t d\tau e^{Q(L_o+L_a)(t-\tau)} QL_I \int_0^\tau d\tau' e^{Q(L_o+L_a)(t-\tau')} QL_I v(\tau').\end{aligned} \tag{A.37}$$

Here we neglected the term proportional to $w(\tau')$ since it produces only terms $\propto L_I^3$ or higher. Again by following the path of how these super-operators act with Fig. A.4, we can quickly identify which terms vanish since all contributing terms need to have closed loops starting and ending in $|g\rangle\langle g|$. So we are left with:

$$\begin{aligned}\dot{v}(t) = {} & L_o v + PL_I \int_0^t d\tau e^{(L_o+L_a)(t-\tau)} L_I v(\tau) \\ & + PJ \int_0^t d\tau e^{(L_o+L_a)(t-\tau)} L_I \int_0^\tau d\tau' e^{(L_o+L_a)(t-\tau')} L_I v(\tau').\end{aligned} \tag{A.38}$$

After extending the lower integral borders to $-\infty$ (Markov approximation), we obtain Eq. (3.7) of the main text.

A.5.2 *Projecting out the cavity field*

The next step is to find a master equation only containing motional degrees of freedom (p and x) of the atom as operators. In order to find this equation we need to use the Nakajima-Zwanzig technique to project out the cavity mode from Eq. (3.7). For the sake of simplicity we assume $\delta_0 \gg \gamma$ (and thus $\frac{g_0^2}{\delta_0^2+\frac{\gamma^2}{4}} \approx \frac{g_0^2}{\delta_0^2}$) and $\kappa \gg \gamma$ in the following, so we can ignore the atomic decay channel for this derivation by approximating $L_{om} \approx L_\kappa$. For weak driving, we can restrict ourselves to the photon subspace defined by $|0\rangle$, $|1\rangle$. Subsequently, we can adopt our projection operator formalism from above and write the density operator as follows:

$$\rho = |0\rangle\langle 0|\rho_{00} + |0\rangle\langle 1|\rho_{01} + |1\rangle\langle 0|\rho_{10} + |1\rangle\langle 1|\rho_{11} \tag{A.39}$$

with $\rho_{ij} = \langle i|\rho|j\rangle$ being the reduced density matrix describing atomic motion. As we are interested in the subspace spanned by $|0\rangle\langle 0|$ we define an projection operator P:

$$P\rho = |0\rangle\langle 0|\rho_{00} \tag{A.40}$$

and

$$Q\rho = |0\rangle\langle 1|\rho_{01} + |1\rangle\langle 0|\rho_{10} + |1\rangle\langle 1|\rho_{11}. \tag{A.41}$$

We again decompose the total Liouvillian in parts according to the way they act:

$$L = L_m + L_{ca} + L_D + J \tag{A.42}$$

with L_m defined in Eq. (A.27),

$$L_{ca} \approx -i[-\Delta(x)a^\dagger a, \rho] - \frac{\kappa}{2}\{a^\dagger a, \rho\} \tag{A.43}$$

and $L_D\rho = -i\sqrt{\kappa_r}E_0[a + a^\dagger, \rho]$, which describes the interaction of the cavity mode with an external coherent laser drive. $J\rho = \kappa a \rho a^\dagger$ describes the spontaneous decay of the cavity mode. Now we draw in Fig. A.5 a picture of the Hilbert space of the degrees of freedom of the cavity, including the arrows which illustrate how these defined super-operators act. A similar prodecure as in Appendix A.5.1 leads to the quantum master equation (3.13) of the main text describing atomic motion.

A.6 SINGLE PHOTON SCATTERING THEORY

Here we provide details of the derivation of Eqs. (3.24) and (3.25) in the main text. Inserting Eqs. (3.22) and (3.23) into

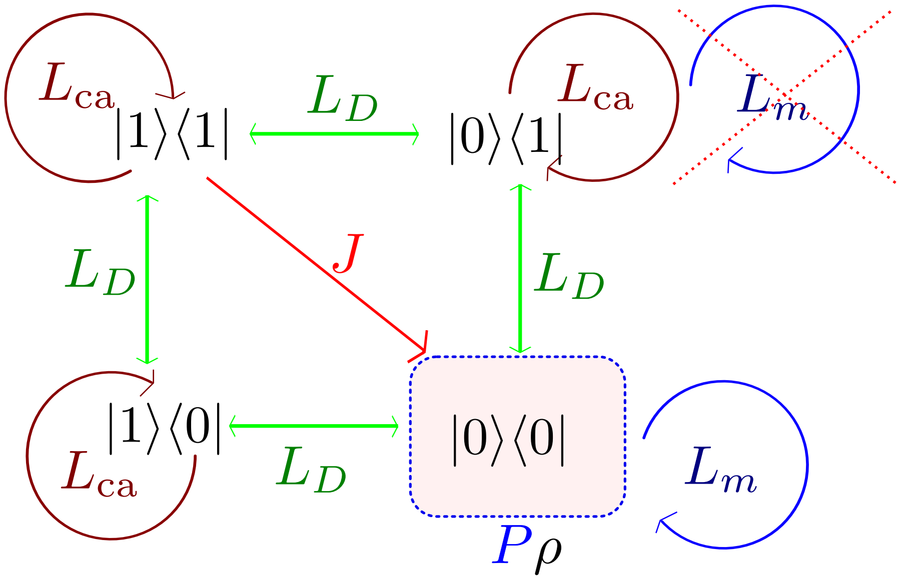

Figure A.5: The Hilbert space of the single excitation subspace of the cavity. The label of an arrow corresponds to a Liouvillian, while the direction of the arrow indicates the possible beginning and ending subspaces of the Liouvillian. For example, the red arrow indicates that the Liouvillian J acting on the subspace $|1\rangle\langle 1|$ takes this subspace to $|0\rangle\langle 0|$. As we assume $\kappa \gg \omega_m$, we can neglect the time evolution due to the super-operator L_m during a fluctuation out of $P\rho$.

Eq. (3.21) and multiplying with $\langle(\omega')_{r/t}, m|$ from the left gives us an equation for the S-matrix elements:

$$S_{r/t,n}(\omega_L)\delta(\omega_L - \omega' - n\omega_m) = \langle(\omega')_{r/t}, n|\, S\, |(\omega_L)_{\text{left}}, 0\rangle \quad \text{(A.44)}$$

where ω' refers to the frequency of the reflected or transmitted photon. In the following, we will establish a connection between the S-matrix elements, and the standard input-output formalism of cavity QED [114]. Conveniently, this connection enables one to calculate S-matrix elements based upon knowledge of the eigenvalues and eigenstates of the system Hamiltonian H_{eff}. The input-output equation states that the output field in each decay channel (reflection/transmission) is the sum of the input field and the field emitted by the scattering center. For example the input-output equation for photon reflection is given by

$$a_{\text{out}}(t) = a_{\text{in}}(t) - i\sqrt{\kappa_r}\, a(t) \quad \text{(A.45)}$$

where for notational convenience we leave out the subscript "r" in the input and output ports. The scattering operators

$a_{\text{in/out}}(\omega)$ are connected to the input-output Heisenberg-Langevin operators $a_{\text{in/out}}(t)$ by a simple Fourier transform [113]

$$a_{\text{in/out}}(\omega) = \frac{1}{\sqrt{2\pi}} \int dt e^{i\omega t} a_{\text{in/out}}(t). \tag{A.46}$$

Now we focus on the S-matrix for the process of photon reflection

$$S_{r,n}(\omega_L)\delta(\omega_L - \omega' - n\omega_m) = \langle 0_c, n| \, a_{\text{out}}(\omega') a_{\text{in}}^{\dagger}(\omega_L) \, |0_c, 0\rangle \tag{A.47}$$

where we expressed the S-matrix in terms of scattering operators $a_{\text{in}}^{\dagger}(\omega_L)$ and $a_{\text{out}}(\omega')$ which create in- and out-going monochromatic scattering states [125]. Using the input-output equation, one can re-write a_{out} in terms of the cavity field and input field, yielding

$$\begin{aligned} S_{r,n}(\omega_L)\delta(\omega_L - \omega' - n\omega_m) = \delta(\omega_L - \omega')\delta_{n,0} \\ - i\sqrt{\kappa_r} \, \langle 0_c, n| \, a(\omega') a_{\text{in}}^{\dagger}(\omega_L) \, |0_c, 0\rangle \, . \end{aligned} \tag{A.48}$$

Now we replace the scattering operators with the Fourier transform of the corresponding input-output operators. The matrix element $\langle 0_c, n| \, a(t') a_{\text{in}}^{\dagger}(t_L) \, |0_c, 0\rangle$ vanishes for $t_L > t'$ since $[a(t'), a_{\text{in}}^{\dagger}(t_L)] = 0$ for $t_L > t'$ and $\langle 0_c| \, a_{\text{in}}^{\dagger}(t_L) = 0$. Thus, we introduce the time ordering operator T making sure that $t' > t_L$. Then we have

$$\langle 0_c, n| \, T[a(t') a_{\text{in}}^{\dagger}(t_L)] \, |0_c, 0\rangle = -i\sqrt{\kappa_r} \, \langle 0_c, n| \, T[a(t') a^{\dagger}(t_L)] \, |0_c, 0\rangle \, , \tag{A.49}$$

where we replaced $a_{\text{in}}(t_L)$ with $a(t_L)$ using the input-output equation. The term containing the output operator vanishes as $[a(t'), a_{\text{out}}^{\dagger}(t_L)] = 0$ for $t' > t_L$ (which is already ensured by T) and $\langle 0_c| \, a_{\text{out}}^{\dagger}(t_L) = 0$. Finally, we arrive at

$$S_{r,n}(\omega_L)\delta(\omega_L - \omega' - n\omega_m) = \delta(\omega_L - \omega')\delta_{n,0} - \kappa_r \tau_n(\omega_L) \tag{A.50}$$

with

$$\tau_n(\omega_L) = \frac{1}{2\pi} \int dt_L dt' e^{i(\omega' t' - \omega_L t_L)} \, \langle 0_c, n| \, T a(t') a^{\dagger}(t_L) \, |0_c, 0\rangle \, . \tag{A.51}$$

For the S-matrix describing the process of photon transmission we obtain

$$S_{t,n}(\omega_L)\delta(\omega_L - \omega' - n\omega_m) = -\sqrt{\kappa_r \kappa_t} \tau_n(\omega_L). \tag{A.52}$$

Note that the S-matrix of reflection S_r includes the term $\delta(\omega_L - \omega')\delta_{n,0}$ describing interaction-free reflection of photons. In contrast, in the S-matrix of transmission S_t there is no such term, since the input field on the transmitting side of the cavity is in the vacuum state and thus the transmitted field is built exclusively from the emission of photons by the scattering center. We can write

$$\langle a(t')a^\dagger(t_L)\rangle = \mathrm{Tr}\left[a e^{L_s(t'-t_L)} a\rho(0)\right], \tag{A.53}$$

where $\rho(0) = |0_c, 0\rangle\langle 0_c, 0|$ and $L_s\rho = -i[H_{\mathrm{eff}}, \rho] + \kappa a\rho a^\dagger$ with H_{eff} described by Eq. (1.3) from the main text. Since the term $\kappa a\rho a^\dagger$ reduces the number of photons, its contribution vanishes as the correlator conserves the number of photons. Thus, the evolution of $a(t)$ is governed by H_{eff} alone and for evaluating the S-matrix we can effectively use

$$a(t) = e^{iH_{\mathrm{eff}}t} a^\dagger e^{-iH_{\mathrm{eff}}t}. \tag{A.54}$$

We further express

$$\langle 0_c, n|\, T a(t')a^\dagger(t_L)\, |0_c, 0\rangle = \Theta(t_L - t')e^{i\omega_n n t_L} \langle 1_c, n|\, e^{-iH_{\mathrm{eff}}(t_L - t')}\, |1_c, 0\rangle \tag{A.55}$$

where $e^{i\omega_n n t_L}$ counts the energy of the created phonons during the scattering process and the step function $\Theta(t_L - t')$ which vanishes for $t_L < t'$ ensures time ordering. In order to express the S-matrix fully in terms of eigenvalues λ_β and eigenstates $|\beta\rangle$ of H_{eff} with $H_{\mathrm{eff}}|\beta\rangle = \lambda_\beta|\beta\rangle$ we insert a unity operator $1 = \sum_\beta |\beta\rangle\langle\beta|$ right before $|1_c, 0\rangle$. Therefore we write

$$\langle 1_c, n|\, e^{-iH_{\mathrm{eff}}(t_L - t')}\, |1_c, 0\rangle = \sum_\beta \langle 1_c, n|\beta\rangle e^{-i\lambda_\beta(t_L - t')}\langle\beta|1_c, 0\rangle \tag{A.56}$$

where $\langle 1_c, n|\beta\rangle$ is the projection of the eigenstates $|\beta\rangle$ into the basis states $\langle 1_c, n|$. After evaluating the Fourier transform in Eq. (A.51) we are left with

$$\tau_n(\omega_L) = -i\delta(\omega_L - \omega' - n\omega_m)\sum_\beta \langle 1_c, n|\beta\rangle \frac{1}{\lambda_\beta}\langle\beta|1_c, 0\rangle. \tag{A.57}$$

which together with Eq. (A.50) and (A.52) reproduces Eq. (3.24) and (3.25) in the main text.

A.7 THE FULL EFFECTIVE THEORY AND ITS VALIDITY

Here we begin by generalizing our effective theory presented in the main text (sections 3.3 and 3.4) by including spontaneous emission into the master equation (3.13) and the single photon scattering output state (3.26). Then we define the parameter space for which our theory is valid. We do this by comparing results of our effective theory with a numerical simulation of the full Jaynes-Cummings model including motion (3.2) where the only assumption is the Lamb-Dicke regime $\eta_{LD} \ll 1$ which allows for the linearization of the mode profile $u(x)$. This approximation is only done for numerical purposes and we note that our effective theory does not depend on the Lamb-Dicke parameter.

For systems where $\kappa \gg \gamma$ is not true, we need to include the atomic decay channel. Doing so, the single photon scattering output state now generalizes to:

$$|\Psi_{out}\rangle = S_r(\omega_L, x)\Psi_o(x)\,|(\omega_L)_r\rangle + S_t(\omega_L, x)\Psi_0(x)\,|(\omega_L)_t\rangle \\ + S_{at}(\omega_L, x)\Psi_0(x)\,|(\omega_L)_{at}\rangle \tag{A.58}$$

where the scattering matrices for reflection, transmission and the scattering matrix for spontaneous emission are respectively given by:

$$S_r(\omega_L, x) = 1 - \frac{i\kappa_r}{\Delta_c(x) + i\frac{\kappa(x)}{2}} \tag{A.59}$$

$$S_t(\omega_L, x) = -\frac{i\sqrt{\kappa_t\kappa_r}}{\Delta_c(x) + i\frac{\kappa(x)}{2}}, \tag{A.60}$$

$$S_{at}(\omega_L, x) = \sqrt{\frac{g_0^2}{\delta_0^2 + \frac{\gamma^2}{4}}}\frac{i\sqrt{\gamma\kappa_r}}{\Delta_c(x) + i\frac{\kappa(x)}{2}}u(x)e^{ik_c x}. \tag{A.61}$$

The scattering matrices conserve probability and obey $|S_r(\omega_L, x)|^2 + |S_t(\omega_L, x)|^2 + |S_{at}(\omega_L, x)|^2 = 1$ for all values of ω_L and x. Note that we treat here for simplicity only one direction of spontaneous emission which has a one dimensional decay channel described by $|(\omega_L)_{at}\rangle$. The resulting momentum kick qualitatively reproduces the main effect that would occur in a full three-dimensional treatment of spontaneous emission. We also did not exclusively account for intrinsic cavity losses at a possible rate κ_{in}, however including this process would simply result in an additional term in the output state Eq. (A.58) with a corresponding S-matrix that looks like S_t, but with κ_t replaced by κ_{in}. The total effective linewidth of the cavity is increased by the effective rate of spontaneous emission

$$\kappa(x) = \kappa_r + \kappa_t + \gamma\frac{g_0^2}{\delta_0^2 + \frac{\gamma^2}{4}}u^2(x), \tag{A.62}$$

which depends on the position of the atom. As explained in the main text, we can express the jump operators in terms of the scattering matrices such that they describe intuitive physical decay processes. The corresponding master equation describing a coherent drive is then given by:

$$\dot{\rho} = -i(H_e\rho - \rho H_e^\dagger) + E_0^2(S_r\rho S_r^\dagger + S_t\rho S_t^\dagger + S_{at}\rho S_{at}^\dagger) \qquad \text{(A.63)}$$

with the Hamiltonian

$$H_e = \omega_m b^\dagger b - \frac{i}{2}E_0^2. \qquad \text{(A.64)}$$

Note that by including spontaneous emission into the model the zero-point resolution reads in good approximation

$$r_{zp} \approx \eta_{LD}\frac{2g_0^2|\delta_0|}{\kappa(x_0)(\delta_0^2 + \frac{\gamma^2}{4})}. \qquad \text{(A.65)}$$

Here we have averaged the position dependent effective decay rate $\kappa(x_0) \approx \langle\Psi_0|\,\kappa(x)\,|\Psi_0\rangle$ with the atomic wavefunction $\Psi_0(x)$.

In order to derive the single photon output state (A.58) and the master equation (A.63) we made two assumptions:

1. Large atom/laser detuning $\delta_0 \gg g_0$, which allowed us to effectively eliminate the excited state of the atom leading to an effective optomechanical master equation (3.7). Note that a large spontaneous emission rate $\gamma \gg g_0$ would allow this elimination as well. However, here we are interested in strongly coupled systems, where $g_0 \gtrsim \gamma$.

2. Unresolved vibrational sidebands $\kappa \gg \omega_m$ which allowed us to derive the output state (A.58) and effectively eliminate the cavity mode in order to derive the master equation (A.63).

Now we will check the limits of these assumptions by numerically simulating a single photon scattering event with the full model (Eq. (3.2)). The numerical simulation is done by diagonalizing the Hamiltonian

$$\begin{aligned} H_D = \omega_m b^\dagger b - (\delta_0 + i\frac{\gamma}{2})\sigma_{ee} - (\delta_c + i\frac{\kappa}{2})a^\dagger a \\ + g_0(u(x_0) + g_0\eta_{LD}(b^\dagger + b))(a^\dagger\sigma_{ge} + h.c.), \end{aligned} \qquad \text{(A.66)}$$

in the single-photon subspace and using the eigenvalues and eigenstates in the exact scattering matrices for reflection, transmition and atomic decay constructed according to Eq. (3.24) and Eq. (3.25). One has to take care that the unity operator as inserted in Eq. (A.56), is here $1 = \sum_\beta |\beta\rangle\langle\beta^*|$, with the eigenvectors normalized as $\langle\beta^*\rangle\,\beta = 1$, since the Hamiltonian H_D is complex symmetric due to losses rather than Hermitian.

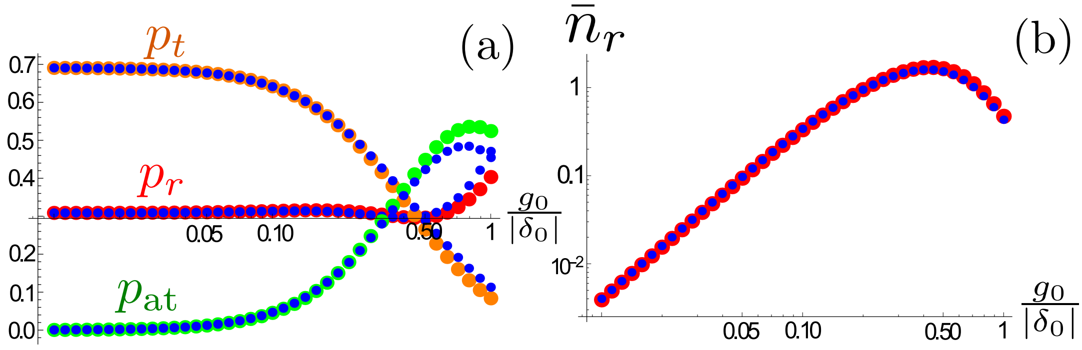

Figure A.6: **Effective theory vs numerical simulation.** We assume the atom to be initially in its motional ground state and the incident photon in resonance with the atom-cavity system. **a)** Probability of photon reflection p_r (red), photon transmission p_t (orange) and spontaneous emission p_{at} (green) as a function of $\frac{g_0}{|\delta_0|}$ and calculated with the effective theory. Blue smaller dots: numerical simulation. Parameters from a recente fiber cavity experiment with trapped $^{40}\mathrm{Ca}^+$-ions (see Appendix A.8.2, parameter set II). Here we choose $\kappa_t = 2\pi \cdot 0.8$Mhz, $\kappa_r = 2\pi \cdot 2.8$Mhz, $\eta_{LD} = \sqrt{\omega_{rec}/\omega_m} = 0.2$, $\omega_m = 2\pi \cdot 0.2$Mhz. **b)** Conditional phonon expectation value $\bar{n}_r$ given that a photon is reflected from the cavity for the same parameters as a). The effective theory (red) matches very well with the numerical simulation (blue).

A.7.1 *Limits of the assumption* $|\delta_0| \gg g_0$

We begin with the question of how large $\frac{g_0}{|\delta_0|}$ can be, such that all approximations previously made are still valid. This is important to know, as the previously studied regime of resolved zero point motion $r_{zp} \gg 1$ requires a large effective optomechanical coupling $r_{zp} \propto g_{om} \overset{\propto}{\sim} \frac{g_0}{|\delta_0|}$. Thus, to reach this regime, it is beneficial to choose $\frac{g_0}{|\delta_0|}$ as large as possible. However, increasing this fraction, we will eventually leave the parameter space in which our effective theory correctly predicts results. To understand when this happens we will now compare our effective theory with a numerical simulation of the full master equation (A.66) as a function of $g_0/|\delta_0|$ (and later as a function of ω_m/κ for similar reasons). We will assume in the following that the atom is trapped in its motional ground state at a location with maximum intra cavity intensity slope $k_c x_0 = \pi/4$ and, if not stated otherwise, that the single incident photon is on resonance with the atom-cavity system $\Delta_c(x_0) = 0$, which implies $x_r = x_0$. Fig. A.6a) shows the probability of photon reflection p_r (red), photon transmission (orange) and spontaneous emission

p_{at} (green) as a function of $g_0/|\delta_0|$ calculated with the effective theory:

$$p_{r/t/at}(\omega_L) = \int dx |S_{r/t/at}(\omega_L, x)|^2 |\Psi_0(x)|^2. \tag{A.67}$$

We use for $|S_{r/t/at}(\omega_L, x)|^2$, Eq. (A.59), Eq. (A.60) and Eq. (A.61), respectively. We also use parameters from a recent fiber cavity experiment (Appendix A.8.2), where $\gamma > \kappa$ and thus, one needs to account for spontaneous emission. The blue dots correspond to the full numerical simulation of the Jaynes-Cummings model including motion (Eq. (A.66)). We observe a great match for $g_0/|\delta_0| < 1/2$. Fig. A.6b) shows the conditional phonon expectation value $\bar{n}_r = \langle\Psi_r| b^\dagger b |\Psi_r\rangle$ given a reflected photon as a function of $g_0/|\delta_0|$ for the same parameters as a). $\Psi_r(x)$ is given by Eq. (3.35) in the main text. We observe a great match for $g_0/|\delta_0| < 1$.

A.7.2 *Limits of the assumption $\kappa \gg \omega_m$*

Here we want to check the validity of the effective theory once sideband resolution is approached. We plot the created phonon expectation value $\bar{n}_r$ after reflecting a single photon in Fig. A.7 as a function of $\frac{\omega_m}{\kappa}$. Here, we take the vacuum Rabi splitting $g_0 = 2\pi \times 10\,\text{GHz}$ corresponding to a possible photonic crystal cavity (A.8.1.1), an atom-cavity detuning of $\omega_0 - \omega_c = 100 g_0$, and again we consider a resonant photon for an atom trapped at $k_c x_0 = \pi/4$. For illustrative purposes, we take an artificially low value of $\kappa = 2\pi \times 20\,\text{MHz}$, which is distributed only between reflection and transmission ports (with $\kappa_r = 4\kappa_t$), and allow ω_m to vary. We observe a reasonable match between the exact numerical simulation and our effective model for $\omega/\kappa < 1/4$.

A.8 EXPERIMENTAL CANDITATE SYSTEMS FOR RESOLVING ZERO-POINT MOTION

A.8.1 *Photonic Crystal Cavities*

The coupling of atoms to the mode of a photonic crystal cavity can be as large as $g_0 \sim 2\pi \times 10\,\text{GHz}$ [126] for Rubidium atoms. Rubidium atoms have a natural linewidth of $\gamma \sim 2\pi \times 6\,\text{MHz}$ and a recoil frequency of $\omega_{rec} \approx 2\pi \times 3.8\,\text{kHz}$ for a resonant photon wavelength around $\lambda_c \approx 780\text{nm}$. At the same time quality factors of more than $Q \sim 10^6$ are feasible inside photonic crystal nano-cavities [76], associated with a decay rate of rougly $\kappa \sim 2\pi \times 0.25\,\text{GHz}$. Since $\gamma \ll \kappa$, spontaneous emission can be

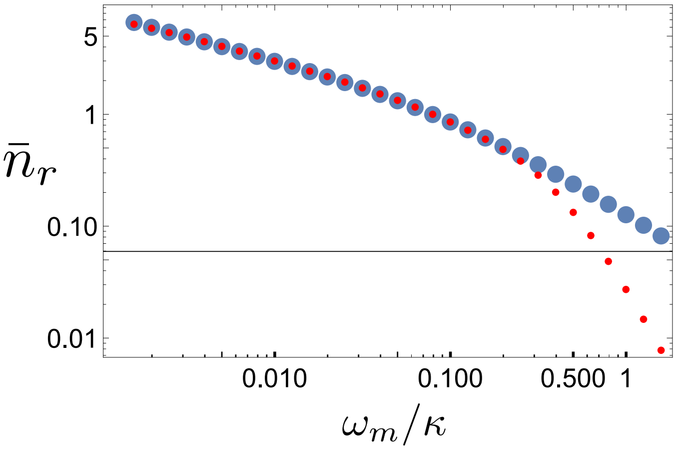

Figure A.7: **Effective theory (blue) vs numerical simulation (red dots) approaching sideband resolution**
We assume the atom to be initially in its motional ground state and that the incident photon is on resonance with the atom-cavity system. We plot the phonon expectation value $\bar{n}_r$ after reflecting a photon as a function of ω_m/κ. Parameters are chosen for an atom trapped inside a photonic crystal cavity as presented in Appendix A.8.1. We choose an atom-cavity detuning of $\omega_0 - \omega_c = 100 g_0$ and an artificial value of $\kappa = 2\pi \times 20\,\text{MHz}$ (with $\kappa_r = 4\kappa_t$) as we only want to check the validity of the effective theory once sideband resolution is approached.

ignored and experiments are very well described by the effective master equation (Eq. (3.13)) and the effective output state (Eq. (3.26)). The achievable zero-point resolution in photonic crystal cavities is $r_{zp} \sim 10$ by taking $\eta_{LD} = 0.25$ (calculated with Eq. (A.65)).

A.8.2 *Fiber Cavities*

Here we discuss a fiber cavity QED experiment with trapped $^{40}\text{Ca}^+$-ions ($\omega_{rec} \approx 2\pi \times 6.8\,\text{kHz}$, $\gamma = 2\pi \times 11.2\,\text{MHz}$) by Tracy Northup in Innbruck [127]. They are able to realize different sets of g_0 and κ by changing the cavity length. Here we give two examples:

1. Parameter set I is given by: $g_0 = 2\pi \times 41\,\text{MHz}$, $\kappa = 2\pi \times 8\,\text{MHz}$.
2. Parameter set II is given by: $g_0 = 2\pi \times 21\,\text{MHz}$ and $\kappa = 2\pi \times 3.6\,\text{MHz}$.

Fig. A.8(a) shows the zero-point resolution r_{zp} as a function of cavity-atom detuning $\omega_0 - \omega_c$ for parameter set I (red) and set II (blue, dashed) calculated with Eq. (A.65). We choose $\omega_m =$

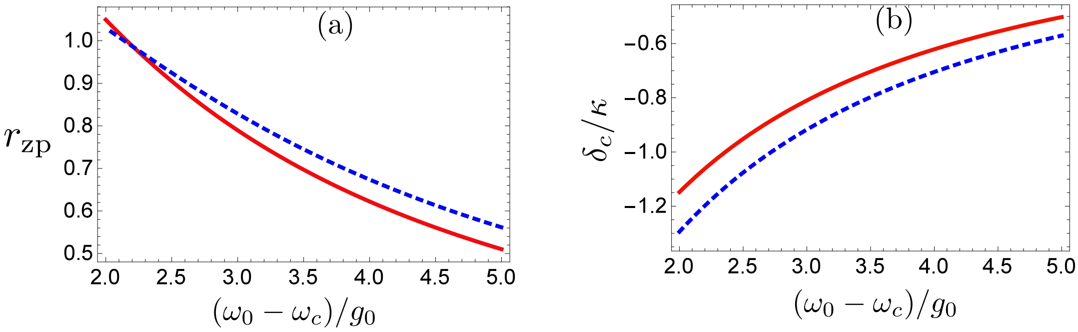

Figure A.8: **a)** Zero-point resolution r_{zp} as a function of cavity-atom detuning $\omega_0-\omega_c$ for parameter set I (red) and set II (blue, dashed) of a tunable fiber cavity experiment with trapped ions. For parameters see A.8.2. Here, we choose $\omega_m = 2\pi \times 0.1$ MHz, $k_c x_0 = \pi/4$ and δ_c such that $x_r = x_0$ (see b)).
b) Here we show how to choose δ_c in order to ensure $k_c x_r = k_c x_0 = \pi/4$. Plotted is the cavity-laser detuning δ_c as a function of $\omega_0-\omega_c$ for parameter set I (red) and set II (blue, dashed) satisfying the condition $\Delta_c(x_r) = 0$.

$2\pi \times 0.1$ MHz, $k_c x_0 = \pi/4$. δ_c is chosen in a way that the condition $\Delta_c(x_r) = 0$ is satisfied, which implies $x_r = x_0$. We observe that by choosing $\omega_0-\omega_c = 2g_0$ one achieves $r_{zp} \approx 1.05$ with parameters set I and $r_{zp} \approx 1.03$ with parameter set II. We also demonstrate how to choose δ_c in order to obtain $k_c x_r = k_c x_0 = \pi/4$ in Fig. A.8(b), which shows δ_c as a function of $\omega_0-\omega_c$ for parameter set I (red) and set II (blue, dashed).

Note that because the spontaneous emission rate γ is comparable to κ, the process of spontaneous emission cannot be neglected and the master equation (A.63) and single photon scattering output state (A.58) need to be applied in order to predict outcomes of this experiment.

A.9 BEYOND THE LAMB-DICKE REGIME: INCLUDING QUADRATIC-ORDER TERMS IN DISPLACEMENT

In order to show that the strong coupling regime of optomechanics can already be observed by an existing experiment, we plotted $g^{(2)}(0)$ as a function of x_0 in Fig. 4.3b) in the main text. In this calculation, we linearized the cavity mode profile $u(x)$ in Hamiltonian Eq. (4.2) of the main text around the trapping position x_0: $u(x) \approx u(x_0) + u'(x_0)k_c(x-x_0)$, which is strictly only valid in the Lamb-Dicke regime $\eta_{LD} = k_c x_{zp} = \sqrt{\omega_{rec}/\omega_m} \ll 1$. However, in order to produce Fig. 4.3 of the main text, we used a trapping frequency of $\omega_m = 2\pi \times 0.1$ MHz. With the recoil frequency of ^{40}Ca$^+$-ions this corresponds to $\eta_{LD} \approx 0.26$.

To ensure that the results are not significantly affected by this relatively large Lamb-Dicke parameter, we will now include the next order term $u(x) \approx u(x_0) + u'(x_0)k_c(x - x_0) + (1/2)u''(x_0)(x - x_0)^2$. In Fig. A.9a), we plot the adjusted $g^{(2)}(0)$ as a function of atom position x_0 and detuning δ_c. Here we choose $\Delta = 10g_0$ and $\omega_m = 2\pi \times 0.09\,\mathrm{MHz}$ in order to minimize $g^{(2)}(0)$ including quadratic order corrections. Fig. A.9b) shows $g^{(2)}(0)$ as a function of atom position x_0 following the ZPL of a) (blue). In red we plot $g^{(2)}(0)$, where $u(x)$ has only been expanded until linear order for the same parameters. We observe a reasonable match and conclude that linearizing motion on the Hamiltonian level at least qualitatively fully captures the relevant physics even for relatively large η_{LD}. For completeness, we plot $g^{(2)}(0)$ as a function of ω_m and Δ in Fig. A.9c) for a fixed atomic position $k_c x_0 = 1.15$, and in Fig. A.9d) we plot $g^{(2)}(0)$ as a function of trapping position x_0 and trap frequency ω_m for $\Delta = 10g_0$.

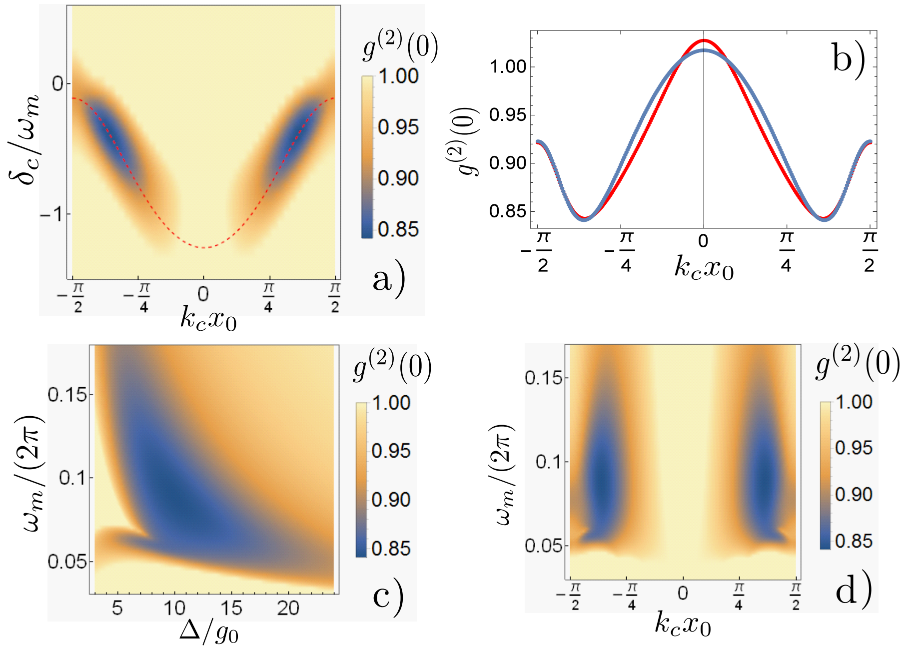

Figure A.9: J-C model with motion expanding $u(x)$ until quadratic order. **a)** $g^{(2)}(0)$ of the transmitted field versus trapping position x_0 and detuning from the empty cavity $\delta_c = \omega_L - \omega_c$, for detunings near the photonic eigenstate and by using the parameters for a realistic cavity QED experiment given below. In this figure, we choose an atom-cavity detuning $\Delta = 10g_0$ and atomic trap frequency $\omega_m = 2\pi \times 0.09\,\text{MHz}$, which produces the minimum possible $g^{(2)}(0)$ including quadratic order corrections. **b)** Following the ZPL of a) (red, dashed). W compare $g^{(2)}(0)$ calculated with only linear displacements (red) in Hamiltonian Eq. (4.2) of the main text with $g^{(2)}(0)$ calculated by also including terms of quadratic order (blue). **c)** $g^{(2)}(0)$ as a function of atom-cavity detuning Δ and trapping frequency ω_m including terms of quadratic order. order. Here, the atomic position is fixed at $k_c x_0 = 1.15$. **d)** $g^{(2)}(0)$ as a function of trapping position x_0 and trapping frequency ω_m for $\Delta = 10g_0$ including terms of quadratic order. As in the main text, we choose parameters of an existing cavity QED experiment with trapped $^{40}\text{Ca}^+$-ions: $g_0 = 2\pi \times 1.4\,\text{MHz}$, $\kappa = 2\pi \times 0.05\,\text{MHz}$, $\gamma = 2\pi \times 11\,\text{MHz}$ and recoil frequency $\omega_{\text{rec}} = 2\pi \times 6.8\,\text{kHz}$.

BIBLIOGRAPHY

1. Ashkin, A. Acceleration and trapping of particles by radiation pressure. *Physical review letters* **24,** 156 (1970).
2. Tsuda, Y *et al.* Flight status of IKAROS deep space solar sail demonstrator. *Acta Astronautica* **69,** 833–840 (2011).
3. Hänsch, T. W. & Schawlow, A. L. Cooling of gases by laser radiation. *Optics Communications* **13,** 68–69 (1975).
4. Ashkin, A. Optical trapping and manipulation of neutral particles using lasers. *Proceedings of the National Academy of Sciences* **94,** 4853–4860 (1997).
5. Chan, J. J. Chan, TPM Alegre, AH Safavi-Naeini, JT Hill, A. Krause, S. Gröblacher, M. Aspelmeyer, and O. Painter, Nature (London) 478, 89 (2011). *Nature (London)* **478,** 89 (2011).
6. Teufel, J., Harlow, J., Regal, C. & Lehnert, K. Dynamical backaction of microwave fields on a nanomechanical oscillator. *Physical review letters* **101,** 197203 (2008).
7. Law, C. Interaction between a moving mirror and radiation pressure: A Hamiltonian formulation. *Physical Review A* **51,** 2537 (1995).
8. Meenehan, S. M. *et al.* Silicon optomechanical crystal resonator at millikelvin temperatures. *Physical Review A* **90,** 011803 (2014).
9. Pirkkalainen, J.-M. *et al.* Cavity optomechanics mediated by a quantum two-level system. *Nature communications* **6,** 6981 (2015).
10. Corbitt, T. *et al.* An all-optical trap for a gram-scale mirror. *Physical review letters* **98,** 150802 (2007).
11. Kleckner, D. & Bouwmeester, D. Sub-kelvin optical cooling of a micromechanical resonator. *Nature* **444,** 75 (2006).
12. Arcizet, O., Cohadon, P.-F., Briant, T., Pinard, M. & Heidmann, A. Radiation-pressure cooling and optomechanical instability of a micromirror. *Nature* **444,** 71 (2006).
13. Gigan, S. *et al.* Self-cooling of a micromirror by radiation pressure. *Nature* **444,** 67 (2006).
14. Thompson, J., Zwickl, B., Jayich, A., Marquardt, F., Girvin, S. & Harris, J. Strong dispersive coupling of a high-finesse cavity to a micromechanical membrane. *Nature* **452,** 72 (2008).

15. Kippenberg, T., Rokhsari, H, Carmon, T, Scherer, A & Vahala, K. Analysis of radiation-pressure induced mechanical oscillation of an optical microcavity. *Physical Review Letters* **95,** 033901 (2005).
16. Schliesser, A., Del'Haye, P., Nooshi, N., Vahala, K. & Kippenberg, T. Radiation pressure cooling of a micromechanical oscillator using dynamical backaction. *Physical Review Letters* **97,** 243905 (2006).
17. Regal, C., Teufel, J. & Lehnert, K. Measuring nanomechanical motion with a microwave cavity interferometer. *Nature Physics* **4,** 555 (2008).
18. Gavartin, E. *et al.* Optomechanical coupling in a two-dimensional photonic crystal defect cavity. *Physical review letters* **106,** 203902 (2011).
19. Kiesel, N., Blaser, F., Delić, U., Grass, D., Kaltenbaek, R. & Aspelmeyer, M. Cavity cooling of an optically levitated submicron particle. *Proceedings of the National Academy of Sciences* **110,** 14180–14185 (2013).
20. Kuhn, S. *et al.* Cavity-assisted manipulation of freely rotating silicon nanorods in high vacuum. *Nano letters* **15,** 5604–5608 (2015).
21. Genoni, M. G., Zhang, J., Millen, J., Barker, P. F. & Serafini, A. Quantum cooling and squeezing of a levitating nanosphere via time-continuous measurements. *New Journal of Physics* **17,** 073019 (2015).
22. Chang, D. E. *et al.* Cavity opto-mechanics using an optically levitated nanosphere. *Proceedings of the National Academy of Sciences* **107,** 1005–1010 (2010).
23. Gieseler, J., Deutsch, B., Quidant, R. & Novotny, L. Subkelvin parametric feedback cooling of a laser-trapped nanoparticle. *Physical review letters* **109,** 103603 (2012).
24. Mestres, P., Berthelot, J., Spasenović, M., Gieseler, J., Novotny, L. & Quidant, R. Cooling and manipulation of a levitated nanoparticle with an optical fiber trap. *Applied Physics Letters* **107,** 151102 (2015).
25. Kippenberg, T. J. & Vahala, K. J. Cavity optomechanics: back-action at the mesoscale. *science* **321,** 1172–1176 (2008).
26. Meystre, P. & Sargent, M. *Elements of quantum optics* (Springer Science & Business Media, 2007).
27. Marquardt, F., Chen, J. P., Clerk, A. & Girvin, S. Quantum theory of cavity-assisted sideband cooling of mechanical motion. *Physical Review Letters* **99,** 093902 (2007).

28. Teufel, J. *et al.* Sideband cooling of micromechanical motion to the quantum ground state. *Nature* **475,** 359 (2011).
29. Sheard, B. S., Gray, M. B., Mow-Lowry, C. M., McClelland, D. E. & Whitcomb, S. E. Observation and characterization of an optical spring. *Physical Review A* **69,** 051801 (2004).
30. Vogel, M, Mooser, C, Karrai, K & Warburton, R. Optically tunable mechanics of microlevers. *Applied Physics Letters* **83,** 1337–1339 (2003).
31. Schumaker, B. L. Quantum mechanical pure states with Gaussian wave functions. *Physics Reports* **135,** 317–408 (1986).
32. Parkins, A. & Kimble, H. Quantum state transfer between motion and light. *Journal of Optics B: Quantum and Semiclassical Optics* **1,** 496 (1999).
33. Zhang, J., Peng, K. & Braunstein, S. L. Quantum-state transfer from light to macroscopic oscillators. *Physical Review A* **68,** 013808 (2003).
34. Vitali, D. *et al.* Optomechanical entanglement between a movable mirror and a cavity field. *Physical review letters* **98,** 030405 (2007).
35. Genes, C, Mari, A, Tombesi, P & Vitali, D. Robust entanglement of a micromechanical resonator with output optical fields. *Physical Review A* **78,** 032316 (2008).
36. Paternostro, M. *et al.* Creating and probing multipartite macroscopic entanglement with light. *Physical Review Letters* **99,** 250401 (2007).
37. Chang, D., Safavi-Naeini, A. H., Hafezi, M. & Painter, O. Slowing and stopping light using an optomechanical crystal array. *New Journal of Physics* **13,** 023003 (2011).
38. Andrews, R. W. *et al.* Bidirectional and efficient conversion between microwave and optical light. *Nature Physics* **10,** 321 (2014).
39. Galland, C., Sangouard, N., Piro, N., Gisin, N. & Kippenberg, T. J. Heralded single-phonon preparation, storage, and readout in cavity optomechanics. *Physical review letters* **112,** 143602 (2014).
40. Nunnenkamp, A, Børkje, K, Harris, J. & Girvin, S. Cooling and squeezing via quadratic optomechanical coupling. *Physical Review A* **82,** 021806 (2010).
41. Gangat, A. A., Stace, T. M. & Milburn, G. J. Phonon number quantum jumps in an optomechanical system. *New Journal of Physics* **13,** 043024 (2011).

42. Sankey, J. C., Yang, C., Zwickl, B. M., Jayich, A. M. & Harris, J. G. Strong and tunable nonlinear optomechanical coupling in a low-loss system. *Nature Physics* **6,** 707 (2010).
43. Thompson, J., Zwickl, B., Jayich, A., Marquardt, F., Girvin, S. & Harris, J. Strong dispersive coupling of a high-finesse cavity to a micromechanical membrane. *Nature* **452,** 72 (2008).
44. Miao, H., Danilishin, S., Corbitt, T. & Chen, Y. Standard quantum limit for probing mechanical energy quantization. *Physical review letters* **103,** 100402 (2009).
45. Huttner, B. & Barnett, S. M. Quantization of the electromagnetic field in dielectrics. *Physical Review A* **46,** 4306 (1992).
46. Rabl, P. Photon blockade effect in optomechanical systems. *Physical review letters* **107,** 063601 (2011).
47. Juan, M. L., Gordon, R., Pang, Y., Eftekhari, F. & Quidant, R. Self-induced back-action optical trapping of dielectric nanoparticles. *Nature Physics* **5,** 915 (2009).
48. Descharmes, N., Dharanipathy, U. P., Diao, Z., Tonin, M. & Houdré, R. Observation of backaction and self-induced trapping in a planar hollow photonic crystal cavity. *Physical review letters* **110,** 123601 (2013).
49. Mestres, P., Berthelot, J., Aćimović, S. S. & Quidant, R. Unraveling the optomechanical nature of plasmonic trapping. *Light: Science & Applications* **5,** e16092 (2016).
50. Birnbaum, K. KM Birnbaum, A. Boca, R. Miller, AD Boozer, TE Northup, and HJ Kimble, Nature (London) 436, 87 (2005). *Nature (London)* **436,** 87 (2005).
51. Reiserer, A. & Rempe, G. Cavity-based quantum networks with single atoms and optical photons. *Reviews of Modern Physics* **87,** 1379 (2015).
52. Volz, J., Scheucher, M., Junge, C. & Rauschenbeutel, A. Nonlinear π phase shift for single fibre-guided photons interacting with a single resonator-enhanced atom. *Nature Photonics* **8,** 965 (2014).
53. Shomroni, I., Rosenblum, S., Lovsky, Y., Bechler, O., Guendelman, G. & Dayan, B. All-optical routing of single photons by a one-atom switch controlled by a single photon. *Science* **345,** 903–906 (2014).
54. Guthöhrlein, G., Keller, M, Hayasaka, K, Lange, W & Walther, H. A single ion as a nanoscopic probe of an optical field. *Nature* **414,** 49 (2001).

55. Mundt, A. *et al.* Coupling a single atomic quantum bit to a high finesse optical cavity. *Physical review letters* **89,** 103001 (2002).

56. Russo, C *et al.* Raman spectroscopy of a single ion coupled to a high-finesse cavity. *Applied Physics B* **95,** 205–212 (2009).

57. Leibrandt, D. R., Labaziewicz, J., Vuletić, V. & Chuang, I. L. Cavity sideband cooling of a single trapped ion. *Physical review letters* **103,** 103001 (2009).

58. Sterk, J., Luo, L, Manning, T., Maunz, P & Monroe, C. Photon collection from a trapped ion-cavity system. *Physical Review A* **85,** 062308 (2012).

59. Steiner, M., Meyer, H. M., Deutsch, C., Reichel, J. & Köhl, M. Single ion coupled to an optical fiber cavity. *Physical review letters* **110,** 043003 (2013).

60. Takahashi, H., Kassa, E., Christoforou, C. & Keller, M. Cavity-induced anticorrelated photon-emission rates of a single ion. *Physical Review A* **96,** 023824 (2017).

61. Black, A. T., Chan, H. W. & Vuletić, V. Observation of collective friction forces due to spatial self-organization of atoms: from Rayleigh to Bragg scattering. *Physical review letters* **91,** 203001 (2003).

62. Purdy, T. P., Brooks, D., Botter, T., Brahms, N., Ma, Z.-Y. & Stamper-Kurn, D. M. Tunable cavity optomechanics with ultracold atoms. *Physical review letters* **105,** 133602 (2010).

63. Li, T. in *Fundamental Tests of Physics with Optically Trapped Microspheres* 81–110 (Springer, 2013).

64. Kiesel, N., Blaser, F., Delić, U., Grass, D., Kaltenbaek, R. & Aspelmeyer, M. Cavity cooling of an optically levitated submicron particle. *Proceedings of the National Academy of Sciences* **110,** 14180–14185 (2013).

65. Millen, J, Fonseca, P, Mavrogordatos, T, Monteiro, T & Barker, P. Optomechanical cooling of a levitated nanosphere in a hybrid electro-optical trap. *Preprint at http://arxiv. org/abs/1407.3595* (2014).

66. Ranjit, G., Atherton, D. P., Stutz, J. H., Cunningham, M. & Geraci, A. A. Attonewton force detection using microspheres in a dual-beam optical trap in high vacuum. *Physical Review A* **91,** 051805 (2015).

67. Ashkin, A. & Dziedzic, J. M. Optical trapping and manipulation of viruses and bacteria. *Science* **235,** 1517–1520 (1987).

68. Liu, Y, Sonek, G., Berns, M. & Tromberg, B. Physiological monitoring of optically trapped cells: assessing the effects of confinement by 1064-nm laser tweezers using microfluorometry. *Biophysical Journal* **71,** 2158–2167 (1996).
69. MacDonald, M., Spalding, G. & Dholakia, K. Microfluidic sorting in an optical lattice. *Nature* **426,** 421 (2003).
70. Wang, M. D., Yin, H., Landick, R., Gelles, J. & Block, S. M. Stretching DNA with optical tweezers. *Biophysical journal* **72,** 1335–1346 (1997).
71. Pang, Y., Song, H., Kim, J. H., Hou, X. & Cheng, W. Optical trapping of individual human immunodeficiency viruses in culture fluid reveals heterogeneity with single-molecule resolution. *Nature nanotechnology* **9,** 624 (2014).
72. Volpe, G., Quidant, R., Badenes, G. & Petrov, D. Surface plasmon radiation forces. *Physical review letters* **96,** 238101 (2006).
73. Nieto-Vesperinas, M, Chaumet, P., Rahmani, A., *et al.* Near-field photonic forces. *Philosophical Transactions-Royal Society of London Series A Mathematical Physical and Engineering Sciences,* 719–738 (2004).
74. Grigorenko, A., Roberts, N., Dickinson, M. & Zhang, Y. Nanometric optical tweezers based on nanostructured substrates. *Nature Photonics* **2,** 365 (2008).
75. Righini, M., Zelenina, A. S., Girard, C. & Quidant, R. Parallel and selective trapping in a patterned plasmonic landscape. *Nature Physics* **3,** 477 (2007).
76. Asano, T., Song, B.-S. & Noda, S. Analysis of the experimental Q factors (˜ 1 million) of photonic crystal nanocavities. *Optics express* **14,** 1996–2002 (2006).
77. Bohren, C. F. & Huffman, D. R. *Absorption and scattering of light by small particles* (John Wiley & Sons, 2008).
78. Corbitt, T. *et al.* An all-optical trap for a gram-scale mirror. *Physical review letters* **98,** 150802 (2007).
79. Hammerer, K. *et al.* Strong coupling of a mechanical oscillator and a single atom. *Physical review letters* **103,** 063005 (2009).
80. Juan, M. L., Righini, M. & Quidant, R. Plasmon nano-optical tweezers. *Nature Photonics* **5,** 349 (2011).
81. Hung, C., Meenehan, S., Chang, D., Painter, O & Kimble, H. Trapped atoms in one-dimensional photonic crystals. *New Journal of Physics* **15,** 083026 (2013).

82. Niedenzu, W., Schütz, S., Habibian, H., Morigi, G. & Ritsch, H. Seeding patterns for self-organization of photons and atoms. *Physical Review A* **88,** 033830 (2013).

83. Domokos, P. & Ritsch, H. Collective cooling and self-organization of atoms in a cavity. *Physical review letters* **89,** 253003 (2002).

84. Black, A. T., Chan, H. W. & Vuletić, V. Observation of collective friction forces due to spatial self-organization of atoms: from Rayleigh to Bragg scattering. *Physical review letters* **91,** 203001 (2003).

85. Baumann, K., Guerlin, C., Brennecke, F. & Esslinger, T. Dicke quantum phase transition with a superfluid gas in an optical cavity. *Nature* **464,** 1301 (2010).

86. Murch, K. W., Moore, K. L., Gupta, S. & Stamper-Kurn, D. M. Observation of quantum-measurement backaction with an ultracold atomic gas. *Nature Physics* **4,** 561 (2008).

87. Thompson, J. D. *et al.* Coupling a single trapped atom to a nanoscale optical cavity. *Science* **340,** 1202–1205 (2013).

88. Goban, A *et al.* Atom–light interactions in photonic crystals. *Nature communications* **5,** 3808 (2014).

89. Aspelmeyer, M., Kippenberg, T. J. & Marquardt, F. Cavity optomechanics. *Reviews of Modern Physics* **86,** 1391 (2014).

90. Safavi-Naeini, A. H. *et al.* Electromagnetically induced transparency and slow light with optomechanics. *Nature* **472,** 69 (2011).

91. Palomaki, T., Teufel, J., Simmonds, R. & Lehnert, K. Entangling mechanical motion with microwave fields. *Science,* 1244563 (2013).

92. Riedinger, R. *et al.* Remote quantum entanglement between two micromechanical oscillators. *arXiv preprint arXiv:1710.11147* (2017).

93. Genes, C., Vitali, D., Tombesi, P., Gigan, S. & Aspelmeyer, M. Ground-state cooling of a micromechanical oscillator: Comparing cold damping and cavity-assisted cooling schemes. *Physical Review A* **77,** 033804 (2008).

94. Marquardt, F., Chen, J. P., Clerk, A. & Girvin, S. Quantum theory of cavity-assisted sideband cooling of mechanical motion. *Physical Review Letters* **99,** 093902 (2007).

95. Bennett, J. S., Khosla, K., Madsen, L. S., Vanner, M. R., Rubinsztein-Dunlop, H. & Bowen, W. P. A quantum optomechanical interface beyond the resolved sideband limit. *New Journal of Physics* **18,** 053030 (2016).

96. Ojanen, T. & Børkje, K. Ground-state cooling of mechanical motion in the unresolved sideband regime by use of optomechanically induced transparency. *Physical Review A* **90,** 013824 (2014).

97. Reiserer, A., Kalb, N., Rempe, G. & Ritter, S. A quantum gate between a flying optical photon and a single trapped atom. *Nature* **508,** 237 (2014).

98. Hacker, B., Welte, S., Rempe, G. & Ritter, S. A photon–photon quantum gate based on a single atom in an optical resonator. *Nature* **536,** 193 (2016).

99. Kimble, H. J. Strong interactions of single atoms and photons in cavity QED. *Physica Scripta* **1998,** 127 (1998).

100. Maunz, P., Puppe, T., Schuster, I., Syassen, N., Pinkse, P. W. & Rempe, G. Cavity cooling of a single atom. *Nature* **428,** 50 (2004).

101. Thompson, J. D. *et al.* Coupling a single trapped atom to a nanoscale optical cavity. *Science* **340,** 1202–1205 (2013).

102. Aoki, T. *et al.* Observation of strong coupling between one atom and a monolithic microresonator. *Nature* **443,** 671 (2006).

103. Darquié, B. *et al.* Controlled single-photon emission from a single trapped two-level atom. *Science* **309,** 454–456 (2005).

104. Tey, M. K. *et al.* Strong interaction between light and a single trapped atom without the need for a cavity. *Nature Physics* **4,** 924 (2008).

105. Jaynes, E. T. & Cummings, F. W. Comparison of quantum and semiclassical radiation theories with application to the beam maser. *Proceedings of the IEEE* **51,** 89–109 (1963).

106. Wilson-Rae, I, Nooshi, N, Dobrindt, J., Kippenberg, T. J. & Zwerger, W. Cavity-assisted backaction cooling of mechanical resonators. *New Journal of Physics* **10,** 095007 (2008).

107. Schütz, S., Habibian, H. & Morigi, G. Cooling of atomic ensembles in optical cavities: Semiclassical limit. *Physical Review A* **88,** 033427 (2013).

108. Nakajima, S. On quantum theory of transport phenomena: steady diffusion. *Progress of Theoretical Physics* **20,** 948–959 (1958).

109. Zwanzig, R. Ensemble method in the theory of irreversibility. *The Journal of Chemical Physics* **33,** 1338–1341 (1960).

110. Horak, P., Hechenblaikner, G., Gheri, K. M., Stecher, H. & Ritsch, H. Cavity-induced atom cooling in the strong coupling regime. *Physical review letters* **79,** 4974 (1997).

111. Domokos, P. & Ritsch, H. Mechanical effects of light in optical resonators. *JOSA B* **20,** 1098–1130 (2003).

112. Fernández-Vidal, S., De Chiara, G., Larson, J. & Morigi, G. Quantum ground state of self-organized atomic crystals in optical resonators. *Physical Review A* **81,** 043407 (2010).

113. Fan, S., Kocabaş, Ş. E. & Shen, J.-T. Input-output formalism for few-photon transport in one-dimensional nanophotonic waveguides coupled to a qubit. *Physical Review A* **82,** 063821 (2010).

114. Caneva, T., Manzoni, M. T., Shi, T., Douglas, J. S., Cirac, J. I. & Chang, D. E. Quantum dynamics of propagating photons with strong interactions: a generalized input–output formalism. *New Journal of Physics* **17,** 113001 (2015).

115. Galland, C., Sangouard, N., Piro, N., Gisin, N. & Kippenberg, T. J. Heralded single-phonon preparation, storage, and readout in cavity optomechanics. *Physical review letters* **112,** 143602 (2014).

116. Wineland, D. J. & Itano, W. M. Laser cooling of atoms. *Physical Review A* **20,** 1521 (1979).

117. Wolf, S., Oliver, S. J. & Weiss, D. S. Suppression of recoil heating by an optical lattice. *Physical review letters* **85,** 4249 (2000).

118. Lechner, W, Habraken, S., Kiesel, N, Aspelmeyer, M & Zoller, P. Cavity optomechanics of levitated nanodumbbells: Nonequilibrium phases and self-assembly. *Physical review letters* **110,** 143604 (2013).

119. Gieseler, J., Deutsch, B., Quidant, R. & Novotny, L. Subkelvin parametric feedback cooling of a laser-trapped nanoparticle. *Physical review letters* **109,** 103603 (2012).

120. Jayich, A. *et al.* Dispersive optomechanics: a membrane inside a cavity. *New Journal of Physics* **10,** 095008 (2008).

121. Ye, J., Kimble, H. & Katori, H. Quantum state engineering and precision metrology using state-insensitive light traps. *science* **320,** 1734–1738 (2008).

122. Domokos, P., Horak, P. & Ritsch, H. Semiclassical theory of cavity-assisted atom cooling. *Journal of Physics B: Atomic, Molecular and Optical Physics* **34,** 187 (2001).

123. Stute, A *et al.* Toward an ion–photon quantum interface in an optical cavity. *Applied Physics B* **107,** 1145–1157 (2012).

124. Joannopoulos, J. D., Johnson, S. G., Winn, J. N. & Meade, R. D. *Photonic crystals: molding the flow of light* (Princeton university press, 2011).

125. Taylor, J. R. *Scattering theory: the quantum theory of nonrelativistic collisions* (Courier Corporation, 2006).
126. Thompson, J. D. *et al.* Coupling a single trapped atom to a nanoscale optical cavity. *Science* **340,** 1202–1205 (2013).
127. Brandstätter, B. *et al.* Integrated fiber-mirror ion trap for strong ion-cavity coupling. *Review of Scientific Instruments* **84,** 123104 (2013).